

TESIS DEFENDIDA POR

Miguel José Costa de Almeida Tenreiro

Y APROBADA POR EL SIGUIENTE COMITÉ

Dr. Luis Zavala Sansón

Director del Comité

Dr. G. J. F. van Heijst

Miembro del Comité

Dr. Julio Sheinbaum Pardo

Miembro del Comité

Dr. Juan Manuel López Mariscal

Miembro del Comité

Dr. Francisco Alejandro Parés Sierra

Miembro del Comité

Dr. Jesús Manuel Figueroa Rodríguez

*Coordinador del programa de
posgrado en Oceanografía Física*

Dr. David Hilario Covarrubias Rosales

Director de Estudios de Posgrado

31 de mayo de 2011

**CENTRO DE INVESTIGACIÓN CIENTÍFICA Y DE
EDUCACIÓN SUPERIOR DE ENSENADA**



**PROGRAMA DE POSGRADO EN CIENCIAS
EN OCEANOGRAFÍA FÍSICA**

**TOPOGRAPHIC EFFECTS ON THE FORMATION, EVOLUTION AND
ORGANIZATION OF COHERENT STRUCTURES IN TURBULENT
FLOWS. THE GULF OF CALIFORNIA CASE**

TESIS

que para cubrir parcialmente los requisitos necesarios para obtener el grado de

DOCTOR EN CIENCIAS

Presenta:

MIGUEL JOSÉ COSTA DE ALMEIDA TENREIRO

Ensenada, Baja California, México, mayo de 2011

RESUMEN de la tesis de **MIGUEL JOSÉ COSTA DE ALMEIDA TENREIRO**, presentada como requisito parcial para la obtención del grado de **DOCTOR EN CIENCIAS** en **OCEANOGRAFÍA FÍSICA**. Ensenada, Baja California, mayo de 2011.

EFFECTOS TOPOGRÁFICOS EN LA FORMACIÓN, EVOLUCIÓN Y ORGANIZACIÓN DE ESTRUCTURAS COHERENTES EN FLUJOS TURBULENTOS. EL CASO DEL GOLFO DE CALIFORNIA

Resumen aprobado por:

Dr. Luis Zavala Sansón

Director de Tesis

El Golfo de California ha sido estudiado ampliamente en las últimas décadas. En particular, en estudios recientes se ha reportado la formación estacional de un tren de remolinos de mesoescala en la parte sur del golfo. Sin embargo, se conoce poco sobre el papel de la topografía del fondo en la formación, evolución y organización de estas estructuras. En esta tesis, se investigan los efectos de topografías abruptas en la circulación del Golfo de California por medio de experimentos de laboratorio y simulaciones numéricas.

Como primera aproximación, se ha investigado el decaimiento de flujos turbulentos cuasi-bidimensionales en un sistema en rotación sobre una topografía tipo escalón. El escalón divide el dominio en dos regiones del mismo tamaño, siendo una profunda y la otra somera. Se ha encontrado una clara concordancia entre los experimentos y las simulaciones basadas en un modelo de aguas someras. Inicialmente, la interacción entre los vórtices origina la auto-organización del flujo, tal como sucede durante la cascada inversa de energía en la turbulencia bidimensional. Además, la interacción de los vórtices con el escalón genera un flujo persistente a lo largo de la topografía con la región somera a la derecha (cuando el parámetro de Coriolis es positivo). Como resultado, el flujo evoluciona casi de manera independiente en las regiones somera y profunda, afectando la eficiencia de la organización. La existencia de una distribución preferencial de vorticidad debida al escalón para tiempos largos (varios periodos de rotación) es ampliamente discutida para dominios cuadrados y rectangulares.

El modelo numérico ROMS (Regional Ocean Modeling System) se ha utilizado para simular de manera más realista la circulación en la parte sur del Golfo de California. Para diferentes topografías se observó la formación de remolinos de mesoescala ciclónicos y anticiclónicos distribuidos de manera alternada durante el período de verano. El proceso de formación de los remolinos depende de la intensa corriente costera, del lado continental, que entra en el golfo en el inicio de esta temporada. Se encontró que la evolución y la posición final de los remolinos durante un período de relajamiento del viento (al final del verano) depende de la forma de la topografía. Además de las simulaciones con el ROMS, se ha usado el modelo de aguas someras para simular la evolución

del flujo en un dominio rectangular similar a la parte sur del golfo. Se han considerado diferentes topografías idealizadas con la intención de representar algunos rasgos batimétricos de la región. Se encontró una fuerte dependencia entre la distribución final de los remolinos y la topografía, de manera análoga a las simulaciones con el ROMS. Una conclusión general es que la evolución del flujo en un dominio rectangular favorece la organización del tren de remolinos de manera similar a como sucede en la parte sur del Golfo de California. Además, la topografía influye en el posicionamiento de los vórtices.

Palabras Clave: Golfo de California, turbulencia, cascada inversa de energía, estructuras coherentes, topografía del fondo.

ABSTRACT of the thesis presented by **MIGUEL JOSÉ COSTA DE ALMEIDA TENREIRO**, in partial fulfillment of the requirements for the degree of DOCTOR IN SCIENCES in PHYSICAL OCEANOGRAPHY. Ensenada, Baja California, May 2011.

TOPOGRAPHIC EFFECTS ON THE FORMATION, EVOLUTION AND ORGANIZATION OF COHERENT STRUCTURES IN TURBULENT FLOWS. THE GULF OF CALIFORNIA CASE

The Gulf of California has been widely studied during the last decades. In particular, the seasonal formation of a train of mesoscale eddies at the southern part of the gulf has been reported in recent studies. However, the role of the bottom topography on the formation, evolution and organization of these structures remains uncertain. In this thesis, the effects of abrupt topography on the circulation of the Gulf of California are investigated by means of idealized laboratory experiments and numerical simulations.

As a first approximation, decaying, quasi-two-dimensional turbulent flows in a rotating system with a step-like topography are investigated. The step divides the domain in two equal-size regions, one being deep and the other shallow. A clear agreement - between experiments and simulations based on a shallow-water model is found. Initially, vortex interactions lead to the self-organization of the flow, as in the classical inverse energy cascade in two-dimensional turbulence. Afterwards, the interaction of vortices with the step generates a persistent flow along the topography with the shallow region at its right (when the Coriolis parameter is positive). As a result, the flow evolves almost independently at the shallow and deep regions, affecting the efficiency of the organization. The existence of a preferential distribution of vorticity due to the step for long times (several rotation periods) is thoroughly discussed for square and rectangular domains.

The Regional Ocean Modeling System (ROMS) is used to simulate the circulation in the southern part of the Gulf of California in a more realistic way. By using different topographies, the formation of counter-rotating mesoscale eddies during the summer period is observed. The eddy formation process strongly depends on the intense eastern boundary current that enters the gulf at the beginning of this season. The evolution and final position of the vortices during a wind relaxation period (late summer) are found to depend on the shape of the topography. In addition to the ROMS simulations, the shallow-water model is used to simulate the flow evolution in a rectangular domain similar to the southern part of the gulf. Different idealized topographies resembling the topographic features that characterize the region were considered. A strong dependence between the final distribution of the vortices and the topography is found, analogous to the ROMS simulations. A general conclusion is that the flow evolution in a rectangular domain favours the eddy-train organization in a similar fashion as in the southern part of the Gulf of California. In addition, the topography plays a role on the positioning of the vortices.

Keywords: Gulf of California, turbulence, inverse energy cascade, coherent structures, bottom topography.

Com eterna saudade

ao meu pai.

Acknowledgements

Este trabajo fue posible gracias a la colaboración de varias personas, por lo que en estas líneas les quiero agradecer,

al Dr. Luis Zavala Sansón por su amistad y total compromiso en la dirección de este trabajo;

a los Drs. GertJan van Heijst, Julio Sheinbaum, Manuel López y Alejandro Parés por su dedicación plena en la realización de este trabajo. Un agradecimiento especial al Dr. Ruben Trieling por sus excelentes comentarios y ayuda en el trabajo experimental;

a todo el Departamento de Oceanografía Física, investigadores, personal administrativo y estudiantes, por su enseñanza, amistad y apoyo incondicional durante esta estancia académica;

a todo el personal del laboratorio de mecánica de fluidos de la Universidad Tecnológica de Eindhoven por su ayuda en la realización de los experimentos. Un agradecimiento especial a Frank Jehoel;

a Paula por su belleza y cariño, reflejo de nuestros hijos Emiliano y Ernesto;

a mi madre, mi hermano y mis dos sobrinas, Pipa y Leonor, porque los amo profundamente. También a toda mi familia, que de una manera u otra, siempre me ha apoyado;

a todos mis amigos que nunca olvidaré;

al CONACyT por su apoyo económico;

al posgrado en Oceanografía Física por el apoyo económico brindado en el final de este trabajo de investigación;

Contents

	Page
Abstract in Spanish	i
Abstract	iii
Dedicatory	v
Acknowledgements	vi
Contents	vii
List of Figures	ix
List of Tables	xv
I. Introduction	1
I.1 Turbulent geophysical systems	1
I.2 Gulf of California	4
I.3 Motivation	9
I.4 Thesis outline	9
II. Theory and methods	12
II.1 Equations of motion	12
II.1.1 Two-dimensional motion	13
II.1.2 Shallow-water model	15
II.1.3 Quasi-2D models	17
II.1.4 Ekman damping effects	19
II.2 Experimental methods	21
II.3 Numerical methods	23
II.3.1 Shallow Water Evolution (SWEVOL)	23
II.3.2 Regional Ocean Modeling System (ROMS)	24
III. Self-organization and decaying process in a rectangular domain with a step topography	27
III.1 Introduction	27
III.2 Laboratory experiments	28
III.2.1 Experimental set-up	28
III.2.2 Results	30
III.3 Numerical simulations	33
III.3.1 General features	35

Contents (continuation)

	Page
III.3.2 Flow at the step region	38
III.3.3 Final configurations	41
III.3.4 Generalization based on ensemble averages	44
III.3.5 Step-limit and step-signal	46
III.3.6 Statistical analysis of the final configuration	48
III.4 Discussion and conclusions	53
IV. Self-organization and decaying process in a square domain with a step topography	57
IV.1 Introduction	57
IV.2 Laboratory experiments	58
IV.2.1 Experimental setup and procedures	58
IV.2.2 General features	61
IV.2.3 Flow at the step	63
IV.2.4 Results based on ensemble averages	65
IV.3 Numerical simulations	69
IV.3.1 Comparison with the laboratory experiments	71
IV.3.2 Results without bottom friction	73
IV.3.3 Different initial conditions	77
IV.4 Discussion and conclusions	79
V. The Gulf of California	83
V.1 Introduction	83
V.2 An idealized Gulf of California	84
V.2.1 Flat-bottom topography	86
V.2.2 Step-array topography	88
V.2.3 Short-platform topography	90
V.3 Gulf of California: a regional approximation	93
V.3.1 Real topography	98
V.3.2 Flat-bottom topography	102
V.3.3 Step-like topography	103
V.3.4 Comparison between simulations	105
V.4 Discussion and conclusions	108
VI. Conclusions and final remarks	111
Bibliography	118

List of Figures

Figure		Page
1	<i>SeaWiFS image of the Gulf of California from October 6, 2001 (SeaWiFS Project, NASA/Goddard Space Flight Center and ORBIMAGE).</i>	5
2	<i>Schematic monthly mean circulation in the Southern part of the Gulf of California (SGC) from hydrographic historical data (taken from Figueroa et al., 2003).</i>	6
3	<i>Schematic picture of the experimental set-up. The initial flow is generated by moving the set of vertical bars from right to left.</i>	29
4	<i>Sequence of top view photographs showing the evolution of an experimental 2D decaying turbulent flow with rotation and discontinuous topography. The black line divides the domain into a deep (lower) and shallow (upper) regions. This experiment is visualized with dye distributed randomly inside the domain before passing the grid.</i>	31
5	<i>Top view data from PIV showing the step region of an experimental flow field at two different times. The small arrows represent the velocity field $\mathbf{u} = (u, v)$. Dark regions represent strong positive (negative) vorticity center at the deep (shallow) side of the step. The black line indicates the position of the step. The big black arrows schematize the flow behavior. The area is a rectangle with dimensions $\sim [75 \text{ cm}, 80 \text{ cm}]$.</i>	32
6	<i>Vorticity contours from a simulation with a low step and no-slip boundary conditions. Dashed contours represent negative values of vorticity, and solid contours represent positive values. The contour level increment is: (a)-(b) 0.02, (c) 0.01 and (d) 0.002.</i>	36
7	<i>As Figure 6, but now for a high step.</i>	38
8	<i>Normalized mean velocity components along six grid-lines adjacent and parallel to the step in the deep region for the simulations shown in Figures 6 and 7. The velocity is normalized with the maximum value for each transect. The time step is $\Delta t = 1$. Dashed contours represent negative values and solid contours represent positive values. Dashed-point contours represents the zero. The contour level interval is 0.2.</i>	39

List of Figures (continuation)

Figure		Page
9	<i>Zoom of Figure 8 panels (a) and (c). The line indicates the separation time between regions and the circle the initial position of the jet for a low (a) and high (b) steps.</i>	40
10	<i>Scatter plots at two different times of simulations shown in Figures 6 and 7. Panels (a)-(b): low step; panels (c)-(d): high step. The values are normalized with maximum absolute values. Dark (grey) points are located in the deep (shallow) region.</i>	41
11	<i>Vorticity contours and scatter plots of three different simulations with a low step-like topography. Dashed contours represent negative values of vorticity, and solid contours represent positive values. The contour level increment is 0.001. Black (grey) dots in scatter plots are located in the deep (shallow) region.</i>	42
12	<i>Time evolution of global quantities with low (solid) and high (dashed) steps: (a) Normalized kinetic energy ($E/E_{(t=0)}$) and normalized enstrophy ($Z/Z_{(t=0)}$); (b) Ratio of Z/E; (c) Mean scale structures; (d) Number of vortices. The data are computed from ensemble averages of twelve runs with slightly different initial conditions.</i>	45
13	<i>Time evolution of integrated relative vorticity in different regions due to different step heights. (a) Schematic representation of the integration regions. Vorticity adjustment in (b) deep, (c) R1, (d) R4, (e) R2 and (f) R3 regions.</i>	47
14	<i>Mean spatial vorticity distribution at $t=400$ for (a) very-low step, (b) low step and (c) high step. Dashed contours represent negative values of vorticity, dashed-dotted contours represent zero values, and solid contours represent positive values. The contour level increment is: (a) 0.001 and (b)-(c) 0.0008.</i>	48
15	<i>Mean spatial vorticity distribution and respective principal components at $t=400$ for the very-low step EOF analysis: (a-b) first, (c-d) second and (e-f) third modes.</i>	50
16	<i>As Figure 15, but now for the low step case.</i>	51
17	<i>As Figure 15, but now for the high step case.</i>	52
18	<i>Summary of the EOF analysis results for different step heights.</i>	53

List of Figures (continuation)

Figure		Page
19	<i>Schematic top and side views of the experimental setup.</i>	59
20	<i>Vorticity surfaces, streamlines contours, and velocity arrows from an experiment with a low step ($\Delta h/H_0 = 0.15$). The black line at $x = 0.5$ indicates the step position which divides the domain in a deep (left) and a shallow (right) region. Grey surfaces represent negative values of vorticity, and dark surfaces represent positive values. The streamlines contour level increment is 0.1. The velocity arrows are scaled for a qualitative view.</i>	61
21	<i>As Fig. 20, but now for a high step ($\Delta h/H_0 = 0.25$).</i>	63
22	<i>Normalized velocity component along the step for the experiments shown in Figs. 20 and 21. The velocity is normalized with the corresponding maximum value along the transect. The time step is $\Delta t = 1$. Grey (black) surfaces represent negative (positive) values.</i>	64
23	<i>Mean spatial distribution of vorticity, streamlines contours, and velocity arrows at $t/T = 35$ from an ensemble of (a) 14 experiments for the low step and (b) 18 experiments for the high step. Grey (black) surfaces represent negative (positive) values of vorticity. The contour level increment for the streamlines is 0.1. The velocity arrows are scaled for a qualitative view.</i>	65
24	<i>Time evolution of the normalized velocity component along the step (V_s, equation 69) for (a) low and (b) high steps, calculated in 14 experiments for the low step and 18 experiments for the high step. The thick, black line indicates the ensemble average.</i>	67
25	<i>Time evolution of (a) normalized kinetic energy (E) and enstrophy (Z) and (b) ratio Z/E, from an ensemble of 14 experiments for the low step (solid lines) and 18 experiments for the high step (dashed lines).</i>	68
26	<i>Time evolution of the ratio Z/E in the shallow (dashed) and deep (solid) regions for the (a) low step and (b) high step. The ensemble is based on 14 experiments using the low step and on 18 experiments using the high step.</i>	69

List of Figures (continuation)

Figure	Page	
27	<i>Vorticity surfaces from a simulation with a high step and no-slip boundary conditions. Grey (dark) surfaces represent negative (positive) values of vorticity. The black line at $x = 0.5$ indicates the step position which divides the domain in a deep (left) and a shallow (right) region.</i>	71
28	<i>Mean spatial vorticity distribution at $t/T = 20$ for (a) low step and (b) high step. Color surfaces as in Fig. 27. The ensemble is based on 27 simulations with slightly different initial conditions for each step height.</i>	72
29	<i>Time evolution of (a) normalized kinetic energy (E) and enstrophy (Z) and (b) ratio Z/E from an ensemble of 27 simulations for each step height.</i>	73
30	<i>Time evolution of the normalized ratio (Z/E) for (a) low step and (b) high step from an ensemble of 27 simulations for each step height. . .</i>	74
31	<i>Mean spatial vorticity distribution at $t/T = 200$ for (a) low step and (b) high step simulations without bottom friction. Grey (dark) surfaces represent negative (positive) values of vorticity. The black line at $x = 0.5$ indicates the step position. The data are computed from an ensemble of 10 simulations for each step height.</i>	74
32	<i>Mean spatial vorticity distribution and respective principal components at $t/T = 200$ for the low step case POD analysis: (a)-(b) first, (c)-(d) second, and (e)-(f) third modes.</i>	76
33	<i>Time evolution of explained changes relative to the mean spatial distribution of vorticity by the (a) first, (b) second, and (c) third modes. Continuous line for the low step and dashed lines for the high step. . . .</i>	77
34	<i>Vorticity surfaces at $t/T = 0$ and $t/T = 200$ from five simulations without bottom friction using different initial conditions.</i>	78
35	<i>Schematic representation of the five topographies used: (a) flat-bottom topography; (b) and (c) step-array topographies; (d) and (e) platform topographies. The depth values $H_{0,1,2,3,4}$ are summarized in table IV. . .</i>	85
36	<i>Vorticity contours from a simulation with a flat-bottom topography (a) with $H_0 = 10^3$ m. Solid (dashed) contours represent positive (negative) values of vorticity. The contour level increment is $10^{-5} s^{-1}$. The horizontal dimensions of the rectangular domain are nondimensionalized by using the width of the box $L_x = 200$ km.</i>	87

List of Figures (continuation)

Figure	Page
37	89
<i>Vorticity contours as in Fig. 36, but now using a step-array topography (b) consisting of five square regions with horizontal dimensions 200×200 km² and depths $H_0 > H_1 > H_2 > H_3 > H_4$ (see Table IV). The step heights at $y = 1, 2, 3, 4$ are 1, 0.5, 0.5, 0.25×10^3 m, respectively.</i>	
38	91
<i>As in the Fig. 37 but now using topography (c) consisting of five square regions with depths $H_0 > H_1 < H_2 > H_3 > H_4$ (see Table IV). The step heights at $y = 1, 2, 3, 4$ are 1, -0.5, 1.0, 0.5×10^3 m, respectively.</i>	
39	93
<i>As Fig. 36, but now using the large-platform topography (d) consisting of a rectangular shallow region with horizontal dimensions $L_x/2 \times L_y/5$ and depth $H_1 = 0.5 \times 10^3$ m. The depth outside the platform is $H_0 = 10^3$ m (see Table IV).</i>	
40	94
<i>As Fig. 39, but now using the short-platform topography (e).</i>	
41	95
<i>Schematic representation of the final distribution of the vortices found for the different topographies: (a) flat-bottom topography; (b) and (c) step-array topographies; (d) and (e) platform topographies. Dark and white surfaces represent cyclonic and anticyclonic structures, respectively [in panel (a) the sense of rotation of the structures is indicated by the white arrows]. Gray arrows represent the flow direction above the steps.</i>	
42	96
<i>Monthly average of the horizontal wind field: streamline contours and vorticity surfaces.</i>	
43	97
<i>Monthly average of the zonal and meridional components of the horizontal wind velocity.</i>	
44	98
<i>Monthly sea surface temperature [$^{\circ}$].</i>	
45	99
<i>Plan view and topographic contours of the GC. The coast-line is defined by the 50 meter isobath. The contour interval is 100 m. The Gulf is divided in northern, central, southern and entrance regions and are referred to as NGC, SGC, and EGC, respectively. The principal basins in the SGC are also indicated.</i>	
46	100
<i>Two-month averaged sea surface height in a simulation using a real topography. The continuous (dashed) contours represent positive (negative) altimetry values. The contour level increment is 10^{-3} m.</i>	

List of Figures (continuation)

Figure		Page
47	<i>Monthly averaged sea surface height for 2005 using a real topography for the SGC region. The continuous contours represent positive altimetry values and dashed contours negative values. The contour levels as in Figure 46.</i>	101
48	<i>Monthly averaged sea surface height for 2005 using a flat-bottom topography for the SGC region. The continuous contours represent positive altimetry values and dashed contours negative values. The contour levels as in Figure 46.</i>	102
49	<i>Monthly averaged sea surface height for 2005 using a step-like topography for the SGC region. The continuous contours represent positive altimetry values and dashed contours negative values. The contour levels as in Figure 46.</i>	104
50	<i>Upper panels: mean relative vorticity along the main axis of the Gulf (shown at the central panel) during July and August in the three regional simulations. Lower panels: the three topographies used in the simulations. The transect is 800 km long and the space between data is 32 km.</i>	105
51	<i>Streamline contours representing the annual mean surface circulation of the GC for the three topographies used in the numerical simulations. The arrows indicate the sense of motion. The contour interval is 5×10^{-3}.</i>	106
52	<i>Annual mean bottom circulation in part of the SGC region. Relative vorticity distributions are represented by colors. The contours represent streamlines, with the sense of motion indicated by the arrows. The longitudinal black line represents the position of the vertical section shown in the insets.</i>	107

List of Tables

Table	Page
I	33
<i>Summary of the laboratory results in terms of number, sign of vorticity and region of the vortices for $t = 25$. $+D$ ($+S$) denotes cyclones in the deep (shallow) region, while $D-$ ($S-$) indicates anticyclones in the deep (shallow) region.</i>	
II	35
<i>Characteristic parameters of the numerical simulations.</i>	
III	43
<i>Summary of the numerical results for low and high steps in terms of number, sign of vorticity and region of the vortices at time $t = 400$. $+D$ ($+S$) cyclone at the deep (shallow) region; $D-$ ($S-$) anticyclone at the deep (shallow) region. The symbol 0 denotes cases in which no structures were found.</i>	
IV	86
<i>Characteristic parameters and topographies of the numerical simulations.</i>	

Chapter I

Introduction

I.1 Turbulent geophysical systems

A geophysical flow system can be characterized by the existence of a great number of scales of motion that may vary from planetary to micro scales. Such a wide range of scales of motion defines the turbulent character of most of the oceanic and atmospheric phenomena. For example, the kinetic energy transfer from smaller to bigger spatial scales characterizes the two-dimensional (2D) turbulence decay, which results in the self-organization of the flow (Kraichnan, 1967; Batchelor, 1967). This effect is known as the inverse energy cascade, which is not observed in three-dimensional flows (3D). In contrast, both cases (2D and 3D) present an enstrophy transfer to small scales, being one of the main characteristics of decaying turbulent flows. Large scale systems (small wave numbers) tend to be conservative, *i.e.* the kinetic energy dissipation is weak, resulting in the persistence of structures like eddies and currents. This kind of phenomena has been studied with increasing interest during the last decades by means of laboratory experiments, numerical simulations and theoretical considerations.

The evolution of 2D turbulent flow in the presence of lateral walls has been a research topic in a number of recent investigations. Clercx *et al.* (1999) described the inverse energy cascade on decaying 2D turbulence in a bounded domain, and compared the results using no-slip and stress-free boundary conditions. They found that the self-organization of the flow in a square box shows a relaxation towards the so-called Stokes

fundamental eigenmode, which consists of a single vortex with size comparable to the domain. Maassen *et al.* (2003) studied the self-organization of decaying, quasi-two-dimensional turbulence in a stratified fluid within rectangular containers by means of laboratory experiments and numerical simulations. Their results were focused on the final states of the flow as a function of the domain geometry, and found a clear difference with the prediction of quasi-stationary final states from statistical-mechanical theories. The authors found that the cell patterns are not merely determined by the shape of the container, but also depend significantly on the formation and detachment of viscous boundary layers. These studies showed the role of no-slip boundaries as sources of vorticity and net angular momentum in two-dimensional turbulence in bounded domains, and demonstrated that these effects play a crucial role in the establishment of these quasi-stationary final states of the flow (see also Clercx *et al.*, 1998; van Heijst *et al.*, 2006; Clercx and van Heijst, 2009).

In contrast with these works, the evolution of 2D turbulent flow over topography has been less studied, specially by means of laboratory experiments. The study of decaying turbulent flows with rotation and topography in terms of the formation of coherent vortices leads to remarkable results with great applications, since the configuration of such structures is an important factor responsible for the transport of physical, chemical and biological properties in the oceans and in the atmosphere. In one of the pioneering works using topography, Bretherton and Haidvogel (1976) describe numerically the inverse energy cascade of a quasi-geostrophic decaying turbulent flow over random topography. They found that the flow tends towards a stationary state aligned with the topography, with cyclonic (anticyclonic) circulation around a depression (bump) (see also Salmon *et al.*, 1976; Herring, 1977). This behavior has been widely studied for different types of flows (vortices, currents) over a number of different bottom to-

pographies (slopes, seamounts, ridges). For a recent review, see van Heijst and Clercx (2009).

A particular idealized topography is a step-like bottom, dividing the flow domain in a shallow and a deep region. The flow evolution is then strongly influenced by changes in height of fluid columns, as they move from one region to another. Studies on barotropic currents interacting with step topographies are reported by Spitz and Nof (1991) and Stern and Austin (1995). The reflection of cyclonic (anticyclonic) vortices from step-down (up) topographies is described in Zavala Sansón *et al.* (1999). For the same kind of topography, Zavala Sansón *et al.* (2005) found a flow along the topography that always keeps the shallow region on the right when a coastal current reaches a step-up or down. Tenreiro *et al.* (2006) investigated the interaction of dipolar structures with a step-like topography and found an equivalent result: a persistent flow along the topography with the shallow region on its right. van de Konijnenberg and van Heijst (1996) describes a spin-up problem using this same configuration and finds always a cyclone (anticyclone) in the deep (shallow) region.

The occurrence of some geophysical processes such as mesoscale currents and vortices is persistent in time and space due to different factors associated with bottom topography and basin geometry. A good example is the Gulf of California, which is an extraordinary natural laboratory where a seasonal circulation of mesoscale geostrophic eddies along the main axis are observed. Hydrographic historical data prove the existence of these eddies that can reach up to 1000 m depth, with horizontal dimensions (<200 km) comparable with that of the basins that characterize the topography of the region (Figuroa *et al.*, 2003). Another case is the sequence of altimetry data showing the presence of cyclonic and anticyclonic eddies inside and outside the Gulf of Aden, aligned along the main Gulf axis (Al Saafani *et al.*, 2007). The authors report that

the presence of cyclones and anticyclones in the vicinity of the Gulf of Aden are due to westward propagating Rossby waves generated in the interior of the Arabian Sea. These two examples show how the circulation pattern seems to depend on the topography and geometry of the basin. In the present work, where laboratory experiments and numerical simulations are done using idealised geometries and topographies, we seek to contribute for a better understanding on how these flow patterns are generated.

Another important effect in geophysical systems is the stratification, which inhibits vertical motions and therefore contributes to the quasi-2D motion of the fluid. Rotation, stratification and topography effects all play a fundamental role in the evolution of the turbulence and therefore in the study of geophysical flows. Numerous works have contributed for a better understanding of the physics involved in the interaction of homogeneous or stratified fluid structures with topography in a rotating system. In this sense, experimental fluid dynamics increasingly arises as one of the fundamental areas of physical oceanography. This thesis is focused on the direct application of fluid dynamics results oriented to study the mesoscale circulation of the Gulf of California, which is considered by many a great natural laboratory of oceanographic phenomena.

I.2 Gulf of California

The Gulf of California (GC) is an interior sea located between the Peninsula of Baja California and the Sonora and Sinaloa coasts, Mexico (Figure 1). Also known as Mar de Cortés, it is an elongated basin (~ 1200 km) that does not exceed 250 km width. Its wide gap to the southeast, which connects it with the Pacific Ocean (PO) (imaginary line between Cape San Lucas and Cape Corrientes), leads some to consider the Gulf as an extension of the Pacific Ocean rather than a semi-enclosed sea. Traditionally the GC



Figure 1. *SeaWiFS image of the Gulf of California from October 6, 2001 (SeaWiFS Project, NASA/Goddard Space Flight Center and ORBIMAGE).*

splits into two geographical regions, one to the south and the other to the north of the central islands. From this natural border there stands out, for their size, the Ángel de la Guardia and Tiburón islands. The north end of the Gulf is the most shallow region (~ 50 m depth) and it is delimited by the delta of the Colorado River. The topography in the GC can be described as a set of basins arranged along the main axis with depths greater than 3,000 m in the southern part.

The GC has been investigated extensively during the last two decades. Oceano-

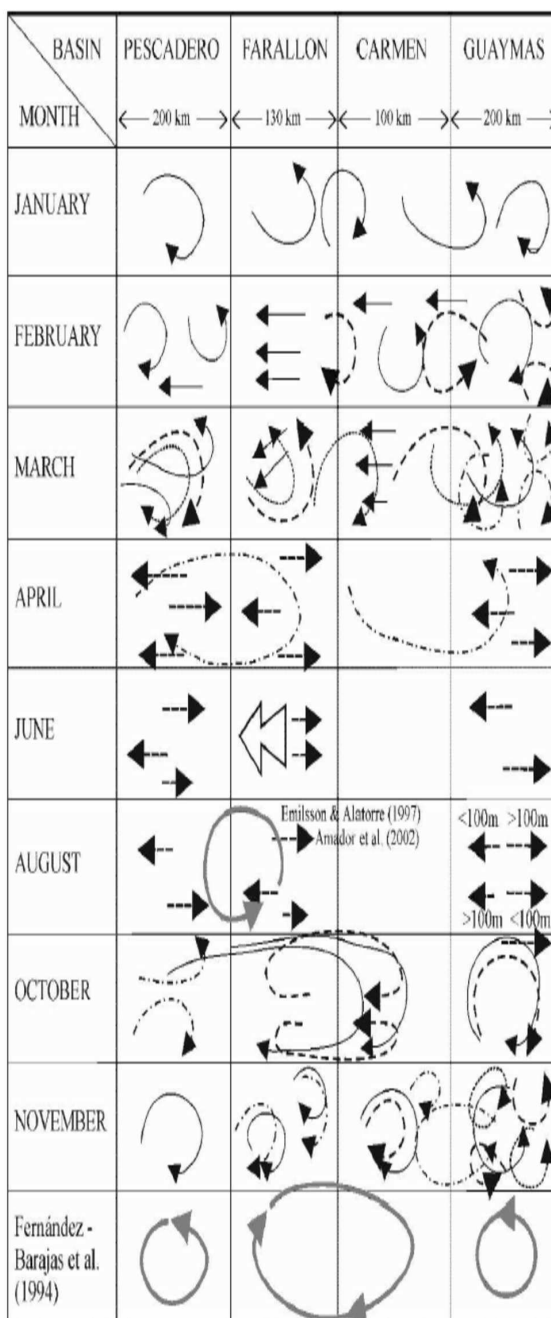


Figure 2. Schematic monthly mean circulation in the Southern part of the Gulf of California (SGC) from hydrographic historical data (taken from Figueroa et al., 2003).

graphic campaigns have been designed to study different scales phenomena, and have provided information for the validation of numerical models, which are often used as a fundamental tool in modern oceanography. In the same way, satellite images have im-

proved the way to identify and describe the structures that characterize the GC. Lavín and Marinone (2003) present a summary of the oceanographic knowledge of the GC. They conclude that the mesoscale circulation far from the coast consists of geostrophic eddies that can reach up to 1000 m depth with horizontal dimensions similar to the basins that characterize the topography of the GC. However, the effect of these structures on the average and seasonal circulation, as well as on the thermodynamics of the GC, is still unknown. The seasonal exchange between the GC and the Pacific Ocean is described by Castro *et al.* (2000), who used CTD data to conclude that the water exchange takes place in a cyclonic way: oceanic currents flow inwards the Gulf along the continental coast and run outwards of it along the peninsula. Figueroa *et al.* (2003) present a description of the circulation in the Southern part of the Gulf of California (SGC): they used hydrographic historical data and looked for evidence of the presence of eddies. These authors found a great variability, both in the horizontal and vertical directions, and in the sense of rotation and position of the eddies. From the data they found evidence of the existence of geostrophic eddies with horizontal scales similar to the Gulf width (~ 200 km), vertical scales that can vary from 500 m to 1000 m, variability in the relative position of the eddies with respect to the topography and seasonal variability in their circulation sign (see Fig. 2). In conclusion, the authors support the view that the presence of eddies is not associated with the topography, but they recommend the use of more information to be able to determine what controls the circulation in the region.

Lavín *et al.* (1997) studied the Northern Gulf of California (NGC) circulation using information from Lagrangian drifters and found a seasonal variability on the structures: the cyclonic summer gyre presents a baroclinic character, whereas the winter circulation results from a combination of baroclinic and barotropic motions. Three mechanisms

- tides, wind stress and forcing in the mouth by exchanges with the PO - could be responsible for the summer gyre, although their relative importance is still unknown. For the winter time, the forcing mechanism presented to explain the observed circulation is the wind, which tends to come from the northwest, and it is more intense than the one observed in the summer. In another study of the same region (NGC), Beier and Ripa (1999) explain the circulation by means of a two-layer model forced with the annual frequency of the PO, wind stress and heat flux across the surface. The model indicates that the seasonal variability on the NGC is more influenced by the PO, with the wind stress and the surface warming both being secondary forcing agents. In the September - October period, Beier and Ripa (1999) observed a cyclonic eddy that occupies the whole central and southern regions of the NGC, and for the February - April period, an anticyclone slightly displaced towards the northwest was found. Argote *et al.* (1998) used a non-linear, vertically integrated model to study the tidal currents forcing and wind stress effect on the barotropic average circulation of the GC and compare the results with current measurements. The authors conclude that in the northern part of the Gulf, during the winter period, the wind stress dominates and the circulation is mainly anticyclonic. In the southern part, a jet along the continental shelf with the same direction of the wind is observed. The differences found in the southern region between the model and the observations are attributed to the baroclinic character of the phenomena. Trying to describe the Lagrangian circulation on the GC using a three-dimensional model, Gutiérrez *et al.* (2004) found that during the cyclonic period a set of particles travels from the south and central regions towards the north, where they remain trapped. In contrast, during the anticyclonic period, these particles flow towards the south, where some of them leave the Gulf and some others remain inside of it, later returning to the NGC. In the central and southern regions, the authors found

some trapping areas at the peninsula side that reach up to 50 km radius and which can retain particles for more than 30 days, whereas on the continental side a fast transition region is described.

I.3 Motivation

As we can see, the mesoscale phenomena of the GC have motivated intensive investigations recently. The dynamics of this kind of structures, like eddies, gyres, fronts and currents, is of vital importance for the biological abundance in the region, for the transport of larvae and pollutants, as well as for the exchange of heat and momentum along the Gulf and with the atmosphere. However, the topographic effects on these structures is unknown. The objective of this thesis is to study these effects by simulating experimentally and numerically turbulent flows with topography in confined domains, including elongated regions resembling the geometrical characteristics of the GC. The aim is to contribute in this way to improve the knowledge of the physical oceanography of the GC.

I.4 Thesis outline

The goal of this thesis is to study the evolution of turbulent flows into well-organized patterns due to the geometry of the domain and the bottom topography. The main objective is to understand the formation, evolution and organization of turbulent flows in the oceans and interior seas when the bottom topography presents abrupt changes of depth. The existence of preferential flow states due to different geometrical and topographical configurations under decaying conditions will be widely discussed. For

this purpose, laboratory experiments and numerical simulations are carried out. A description of the laboratory experiments and the numerical models used to simulate the experimental results are given in chapter II. The equations of motion and the essential dynamical effects associated with bottom topography are also described in chapter II.

In chapters III and IV, a barotropic quasi-two-dimensional approximation is used to understand the physical mechanisms behind the organization of the flow due to the presence of a discontinuous topography (step-like). The results are oriented to understand the flow evolution in rectangular and square geometries, respectively. The barotropic approximation helps to isolate the influence of the domain geometry and the bottom topography in the flow organization. This is an appropriate approximation since, due to the rotation of the system, the flow is almost two-dimensional and characterized by the inverse energy cascade, or self-organization of the flow. This process is systematically observed in the laboratory experiments and well represented by the barotropic, shallow-water model. A step-like topography is used to divide the domain in a deep and a shallow region, both with the same horizontal dimensions. Different step heights are used in order to quantify the step-signal on the flow organization.

In chapter V, the same barotropic, shallow-water model is used on a rectangular domain with dimensions comparable with the southern part of the Gulf of California. Different bottom configurations are considered in order to represent some of the different topographic features of the Gulf. The aim is to compare the results with those obtained from a more realistic model: the Regional Ocean Modeling System (ROMS). The circulation of the Gulf of California is simulated by means of ROMS using different topographies and realistic conditions: wind forcing, stratification effects, solar radiation, etc. The goal is to identify some of the topographic effects responsible for the

generation and organization of the vortices that characterize the mesoscale circulation in the region during the summer period.

The main conclusions and final remarks of this thesis will be summarized in chapter VI.

Chapter II

Theory and methods

II.1 Equations of motion

The equations that govern the motion of fluids are derived from Newton's Second Law of Motion, $\mathbf{F} = \frac{d\mathbf{p}}{dt}$, which expresses that the net force (\mathbf{F}) on an element is equal to the time derivative of the momentum of the element, $\mathbf{p} = m\mathbf{v}$, where m is mass and \mathbf{v} is the velocity. If the mass is conserved, then $\mathbf{F} = m\frac{d\mathbf{v}}{dt} = m\mathbf{a}$, with \mathbf{a} the acceleration. From this simple equation, the so-called Navier-Stokes equations are deduced and used to describe most of fluid motions, including geophysical systems. In the present study, a homogeneous, incompressible fluid moving in a steadily rotating system is described by the spatial coordinates \mathbf{r} and the velocity field $\mathbf{u}(\mathbf{r}, t)$ satisfying the momentum balance equations

$$\frac{\partial \mathbf{u}}{\partial t} + (\mathbf{u} \cdot \nabla) \mathbf{u} + 2\boldsymbol{\Omega} \times \mathbf{u} = -\frac{1}{\rho} \nabla P + \mathbf{g} + \nu \nabla^2 \mathbf{u} - \boldsymbol{\Omega} \times (\boldsymbol{\Omega} \times \mathbf{r}), \quad (1)$$

where $\boldsymbol{\Omega}$ is the system's angular velocity, ρ is the fluid density which will be considered constant, and P is the pressure. Conservative forces (per unit mass) are given by the acceleration caused by gravity $\mathbf{g} = \nabla\phi$, with ϕ the gravitational potential, and non-conservative forces are associated with dissipative viscous effects given by $\nu \nabla^2 \mathbf{u}$, where ν is the kinematic viscosity, assumed constant. The rotation effects are represented by the Coriolis ($2\boldsymbol{\Omega} \times \mathbf{u}$) and the centrifugal [$-\boldsymbol{\Omega} \times (\boldsymbol{\Omega} \times \mathbf{r})$] accelerations. The Coriolis term, which describes an acceleration perpendicular to the velocity vector \mathbf{u} , has a significant role in the flow evolution, while centrifugal effects can be included as a conservative

effect $-\boldsymbol{\Omega} \times (\boldsymbol{\Omega} \times \mathbf{r}) = \frac{1}{2}\nabla(|\boldsymbol{\Omega} \times \mathbf{r}|^2)$ in an "effective" gravitational potential.

Since ρ is constant, the reduced pressure can be defined as

$$p = P - \rho\left(\phi + \frac{1}{2}|\boldsymbol{\Omega} \times \mathbf{r}|^2\right), \quad (2)$$

and the momentum equation becomes

$$\frac{\partial \mathbf{u}}{\partial t} + (\mathbf{u} \cdot \nabla)\mathbf{u} + 2\boldsymbol{\Omega} \times \mathbf{u} = -\frac{1}{\rho}\nabla p + \nu\nabla^2\mathbf{u}, \quad (3)$$

that together with the conservation of mass (continuity)

$$\nabla \cdot \mathbf{u} = 0, \quad (4)$$

describes the fluid motion.

Hereafter we shall consider a Cartesian coordinate system (x, y, z) in which the fluid velocity has components $\mathbf{u} = (u, v, w)$, the angular velocity is oriented along the z -direction, $\boldsymbol{\Omega} = (0, 0, \Omega)$, and gravity in the opposite direction, $\mathbf{g} = (0, 0, -g)$.

II.1.1 Two-dimensional motion

In a system dominated by rotation effects, the motion is almost completely restricted to the horizontal plane (x, y) perpendicular to the rotation axis z . Such a phenomenon is commonly observed in laboratory experiments, when rotating tanks are used to simulate the Earth's rotation. The two-dimensionality of the flow, which has been observed and used since the work of Taylor (1923), is a good approximation under experimental conditions.

In order to justify mathematically the two-dimensional (2D) behavior of the flow dominated by rotation effects, equation (3) can be nondimensionalized using a length scale L , a velocity scale V , and a time L/V ; considering pressure as $\Omega V L \rho$ the equation

for the flow field \mathbf{u} becomes

$$R_o \left(\frac{\partial \tilde{\mathbf{u}}}{\partial t} + (\tilde{\mathbf{u}} \cdot \tilde{\nabla}) \tilde{\mathbf{u}} \right) + 2\hat{k} \times \tilde{\mathbf{u}} = -\tilde{\nabla} \tilde{p} + E \tilde{\nabla}^2 \tilde{\mathbf{u}}, \quad (5)$$

where \hat{k} is the unit vector in the local z direction, $R_o = \frac{V}{\Omega L}$ is the Rossby number and $E = \frac{\nu}{\Omega L^2}$ is the Ekman number. (Tildes denoting nondimensional quantities and operators will be omitted from this point onwards for clarity). The Rossby number R_o is a typical measure of the rotation effects. If $R_o \ll 1$, the accelerations of the flow are much smaller than those associated with the rotation of the system, and therefore the rotation effects dominate the flow evolution. The Ekman number E is a measure of the viscous terms compared with rotation effects. If $E \ll 1$ then viscous effects are weak. When $R_o \ll 1$ and $E \ll 1$, equation (5) for a steady flow becomes

$$2\hat{k} \times \mathbf{u} = -\nabla p \quad (6)$$

which represents the geostrophic balance, *i.e.* the Coriolis and pressure-gradient forces are in balance. Taking the curl and using continuity yields

$$\frac{\partial \mathbf{u}}{\partial z} = 0, \quad (7)$$

which is the Taylor-Proudman theorem. It means that the flow is independent of the vertical coordinate z . This independence is clearly observed in the vertical structure of vortices in rotating homogeneous fluids, which are manifested as columns aligned with the rotation axis, known as Taylor columns.

In laboratory experiments using rotating tables this columnar behavior of the flow is commonly observed, even when $R_o = O(1)$. Therefore, it is often accepted to consider the flow as quasi-two-dimensional, in the sense that the vertical velocities are much smaller than the horizontal ones.

II.1.2 Shallow-water model

In order to include topographic effects, equations (3) and (4) can be written as

$$\frac{\partial u}{\partial t} + u \frac{\partial u}{\partial x} + v \frac{\partial u}{\partial y} - fv = -\frac{1}{\rho} \frac{\partial p}{\partial x} + \nu \nabla^2 u, \quad (8)$$

$$\frac{\partial v}{\partial t} + u \frac{\partial v}{\partial x} + v \frac{\partial v}{\partial y} + fu = -\frac{1}{\rho} \frac{\partial p}{\partial y} + \nu \nabla^2 v, \quad (9)$$

$$0 = -\frac{1}{\rho} \frac{\partial p}{\partial z} - g, \quad (10)$$

$$\frac{\partial u}{\partial x} + \frac{\partial v}{\partial y} + \frac{\partial w}{\partial z} = 0, \quad (11)$$

where (u, v) are the horizontal velocity components in (x, y) directions and which are considered independent of the z direction, w is the vertical velocity component, and f is the Coriolis parameter defined as $f = 2\Omega$. Under the shallow-water approximation, vertical accelerations are ignored and therefore the hydrostatic balance dominates in the vertical equation of motion (10).

Since u and v are z -independent, it is possible to integrate the continuity equation (11) between an arbitrary bottom topography, $h_B(x, y)$, and the free surface located at a height $H(x, y, t)$:

$$(\nabla \cdot \mathbf{u})(H - h_b) = \omega|_{z=h_b} - \omega|_{z=H}. \quad (12)$$

Note that $H(x, y, t) = H_0 + \eta(x, y, t)$ is the sum of a reference height H_0 and the free surface deformation $\eta(x, y, t)$. The fluid depth is given by $h(x, y, t) = H(x, y, t) - h_b(x, y)$.

For solid boundaries, the normal component of the mass flux must be zero, which implies for a variable bottom topography that

$$w|_{z=h_b} = u \frac{\partial h_b}{\partial x} + v \frac{\partial h_b}{\partial y}. \quad (13)$$

For the flat bottom case where h_b is constant, *i. e.* $\nabla h_b = 0$, the vertical velocity $w|_{z=h_b}$ is zero. The kinematic condition for the free-surface is

$$w|_{z=H} = \frac{DH}{Dt}, \quad (14)$$

where $\frac{D}{Dt} = \frac{\partial}{\partial t} + u\frac{\partial}{\partial x} + v\frac{\partial}{\partial y}$ is the material derivative. Substituting (13) and (14) in equation (12) gives

$$(\nabla \cdot \bar{u})(H - h_b) = -\frac{D}{Dt}(H - h_b). \quad (15)$$

On the other hand, vertical integration of equation (10) yields

$$p(x, y, z, t) = -\rho g z + c(x, y, t), \quad (16)$$

where c represents an integration function. Using the boundary condition at the free surface $p(x, y, H) = p_0$, where p_0 is constant, the equation above becomes

$$p(x, y, z, t) = -\rho g(H - z) + p_0. \quad (17)$$

Applying this result in the momentum equations, and rewriting the vertically integrated continuity equation (15), the original system can be reduced to three equations in terms of u, v, η (or h)

$$\frac{\partial u}{\partial t} + u\frac{\partial u}{\partial x} + v\frac{\partial u}{\partial y} - fv = -g\frac{\partial \eta}{\partial x} + \nu \nabla^2 u, \quad (18)$$

$$\frac{\partial v}{\partial t} + u\frac{\partial v}{\partial x} + v\frac{\partial v}{\partial y} + fu = -g\frac{\partial \eta}{\partial y} + \nu \nabla^2 v, \quad (19)$$

$$\frac{\partial h}{\partial t} + \frac{\partial(hu)}{\partial x} + \frac{\partial(hv)}{\partial y} = 0. \quad (20)$$

These are the shallow water equations for a homogeneous fluid layer over variable topography (see e.g. Pedlosky, 1987).

Since the flow is considered nearly two-dimensional, the only relevant vorticity component is the vertical component

$$\omega = \hat{k} \cdot \nabla \times \mathbf{u} = \frac{\partial v}{\partial x} - \frac{\partial u}{\partial y}. \quad (21)$$

The z -component of the relative vorticity equation is obtained by taking the y -derivative of (18) and subtracting it from the x -derivative of (19), which yields

$$\frac{D\omega}{Dt} + \left(\frac{\partial u}{\partial x} + \frac{\partial v}{\partial y} \right) (\omega + f) = \nu \nabla^2 \omega. \quad (22)$$

Equation (20) can be rewritten as

$$\frac{\partial u}{\partial x} + \frac{\partial v}{\partial y} = -\frac{1}{h} \frac{Dh}{Dt}, \quad (23)$$

which combined with (22) gives

$$\frac{Dq}{Dt} = \frac{\nu}{h} \nabla^2 \omega, \quad (24)$$

where the *potential vorticity* q is defined by

$$q = \frac{\omega + f}{h}. \quad (25)$$

II.1.3 Quasi-2D models

In order to derive a two-dimensional system, the rigid-lid approximation is considered: the changes in the fluid depth due to free-surface oscillations are assumed to be small compared with those caused by the topography. In this way $\frac{\partial h}{\partial t} \sim 0$. From this assumption, gravity waves at the surface are neglected in our problem. Thus, the continuity equation is reduced to

$$\frac{\partial(hu)}{\partial x} + \frac{\partial(hv)}{\partial y} = 0, \quad (26)$$

where now $h = h(x, y)$ is time independent. From this expression it is possible to define a stream function ψ as

$$u = \frac{1}{h} \frac{\partial \psi}{\partial y} \quad (27)$$

$$v = -\frac{1}{h} \frac{\partial \psi}{\partial x}. \quad (28)$$

Using these expressions, the evolution equation for the relative vorticity is

$$\frac{\partial \omega}{\partial t} + J(q, \psi) = \nu \nabla^2 \omega, \quad (29)$$

where $J(q, \psi) = \frac{\partial q}{\partial x} \frac{\partial \psi}{\partial y} - \frac{\partial q}{\partial y} \frac{\partial \psi}{\partial x}$ is the Jacobian operator. The relation between ψ and ω is given by

$$\omega = -\frac{1}{h} \nabla^2 \psi + \frac{1}{h^2} \nabla h \cdot \nabla \psi. \quad (30)$$

Equations (29) and (30) are sometimes referred to as the barotropic nondivergent model (Grimshaw *et al.*, 1994).

Considering a particular case where $h = H_0$ (flat bottom case), it can be observed from the continuity equation that the flow is non-divergent

$$\frac{\partial u}{\partial x} + \frac{\partial v}{\partial y} = 0, \quad (31)$$

which means that a stream function can be defined as

$$u = \frac{\partial \psi^*}{\partial y}, \quad (32)$$

$$v = -\frac{\partial \psi^*}{\partial x}. \quad (33)$$

In this case the relation between stream function ψ^* and relative vorticity ω is given by the well-known Poisson equation

$$\omega = -\nabla^2 \psi^*. \quad (34)$$

The vorticity equation is reduced to

$$\frac{\partial \omega}{\partial t} + J(\omega, \psi^*) = \nu \nabla^2 \omega. \quad (35)$$

This equation can be written as

$$\frac{D\omega}{Dt} = \nu \nabla^2 \omega, \quad (36)$$

being the relative vorticity evolution equation for a fluid over a flat bottom. Note that it has exactly the same form as for a purely 2D flow.

II.1.4 Ekman damping effects

An additional effect on a rotating fluid is the adjustment of the flow to the boundary conditions that occurs both in the top and bottom boundary layers, usually called Ekman layers. Damping effects driven by viscous boundary layers are determined by the Ekman number. In the upper boundary, a viscous Ekman layer can be generated for example by wind-stress effects, which will not be considered in this work. On the other hand, the bottom boundary layer is produced by the imposed no-slip boundary condition at the solid bottom, which provides the mechanism for bottom friction effects. The 2D flow motion is only slightly affected from bringing the velocity gradually to zero within this thin layer above the bottom, which allows its incorporation in a 2D physical model.

Writing the Ekman number as

$$E = \frac{2\nu}{fH^2} \quad (37)$$

where H is the vertical length scale, the Ekman layer thickness is defined as

$$\delta_E = \left(\frac{2\nu}{f} \right)^{1/2} \equiv E^{1/2} H \quad (38)$$

(inside Ekman layers the viscous term should balance the Coriolis term). Notice that the Ekman layer thickness δ_E becomes smaller when rotation increases.

The Ekman layer at the bottom generally induces a non-zero vertical velocity which is proportional to the relative vorticity of the flow outside the Ekman layer. This is known as the Ekman pumping condition:

$$w|_{z=0} = \frac{1}{2}\delta_E\omega. \quad (39)$$

Linear and nonlinear Ekman effects can be incorporated in a quasi-2D model with variable topography as described by Zavala Sansón and van Heijst (2002). For variable bottom topography the condition for the vertical velocity can be expressed as

$$w|_{z=h_b} = u\frac{\partial h_b}{\partial x} + v\frac{\partial h_b}{\partial y} + \frac{1}{2}\delta_E\omega. \quad (40)$$

By using this expression in the vertically integrated continuity equation yields

$$\frac{\partial u}{\partial x} + \frac{\partial v}{\partial y} = -\frac{1}{h}\frac{Dh}{Dt} + \frac{1}{2}\frac{\delta_E}{h}\omega, \quad (41)$$

which states that the horizontal divergence is given by fluid depth changes due to free-surface variations and topography and by the vertical velocity induced by the Ekman layer at the bottom. Applying the rigid-lid approximation, equation (41) becomes

$$\frac{\partial u}{\partial x} + \frac{\partial v}{\partial y} = -\frac{1}{h}\left(u\frac{\partial h}{\partial x} + v\frac{\partial h}{\partial y}\right) + \frac{\delta_E}{2h}\omega. \quad (42)$$

Substitution of the horizontal divergence in the vorticity equation (22) yields

$$\frac{\partial \omega}{\partial t} + hu\frac{\partial q}{\partial x} + hv\frac{\partial q}{\partial y} = \nu\nabla^2\omega - \frac{\delta_E}{2h}\omega(\omega + f), \quad (43)$$

where q is the potential vorticity defined above.

Expressions for u and v are obtained by rewriting equation (42) in terms of partial derivatives as

$$\frac{\partial}{\partial x}\left(hu - \frac{1}{2}\delta_E v\right) + \frac{\partial}{\partial y}\left(hv - \frac{1}{2}\delta_E u\right) = 0, \quad (44)$$

and by defining a stream function ψ such that

$$hu - \frac{1}{2}\delta_E v = \frac{\partial\psi}{\partial y}, \quad (45)$$

$$hv + \frac{1}{2}\delta_E u = -\frac{\partial\psi}{\partial x}. \quad (46)$$

Since that the Ekman layer thickness is always much smaller than the fluid depth, the horizontal velocities are approximated as

$$u = \frac{1}{h} \left(\frac{\partial\psi}{\partial y} - \frac{\delta_E}{2h} \frac{\partial\psi}{\partial x} \right) \quad (47)$$

$$v = \frac{1}{h} \left(\frac{\partial\psi}{\partial x} - \frac{\delta_E}{2h} \frac{\partial\psi}{\partial y} \right). \quad (48)$$

Using these results in equation (43), the evolution equation for the relative vorticity is now

$$\frac{\partial\omega}{\partial t} + J(q, \psi) - \frac{\delta_E}{2h} \nabla\psi \cdot \nabla q = \nu \nabla^2 \omega - \frac{\delta_E}{2h} \omega(\omega + f). \quad (49)$$

The relative vorticity obeys the relation

$$\omega = -\frac{1}{h} \nabla^2 \psi + \frac{1}{h^2} \nabla h \cdot \nabla \psi + \frac{\delta_E}{2h} \frac{2}{h^2} J(h, \psi). \quad (50)$$

The terms in (49) and (50) that involve the Ekman layer thickness are due to Ekman friction. The left-hand side in (49) represents a non-linear correction to the advection effects driven by the Ekman layer, and the one on the right-hand side represents stretching effects associated with the Ekman pumping.

II.2 Experimental methods

The laboratory experiments were performed in rectangular (chapter III) and square (chapter IV) rotating tanks with horizontal dimensions $150 \times 75 \text{ cm}^2$ and $100 \times 100 \text{ cm}^2$, respectively, both filled with fresh water. The horizontal aspect ratio of the tanks,

defined as the ratio between length and width, are $\delta = 2$ and $\delta = 1$, respectively. A step-like topography (discontinuity) was used to divide the horizontal area of the tanks in two regions with different depths, one deep and the other shallow. The rectangular container was divided in two square regions and the square container in two rectangular regions. Such a difference implies a very different organization of the flow after several rotation periods of the system. The height of the water column at the deepest part was fixed at $H_0 = 20$ cm. Two step heights were used for each tank ranging between 1 and 5 cm. For further details see chapters III and IV.

The rotation rate of the tank around the vertical axis was fixed at $\Omega = 0.5$ rad s⁻¹, which corresponds to a Coriolis parameter $f = 2\Omega = 1$ s⁻¹. The decay induced by bottom friction is associated with the Ekman period, $T_E = H_0/(\nu\Omega)^{1/2} \approx 280$ s, for $\nu = 0.01$ cm²s⁻¹ (kinematic viscosity of water at 20 °C), which is roughly the duration of a typical experiment. The time scale associated to the Ekman decay is much longer than the rotation period, $T = 2\pi/\Omega \approx 12$ s.

The experimental procedure consisted of setting the tank in rotation at a constant angular speed for about 30-45 min before starting an experiment, in order to ensure that the fluid has reached a state of solid body rotation. The parabolic free-surface (1 to 3 mm) effects are ignored, assuming that the change in depth due to the bottom step (1 – 5 cm) are more important.

A disordered small-scale initial flow field was generated by passing a grid of vertical bars through the fluid. The grid was moved with constant speed by an electric motor mounted on the table. Once the flow has been forced, the grid is removed by vertically lifting it out of the fluid. The flow field evolution was recorded with a co-rotating camera mounted at some distance above the tank. For qualitative experiments, the vortices are visualized by adding fluorescent dye to the fluid. Quantitative experiments

were performed using passive tracers floating on the surface. Particle image velocimetry (PIV) was used for measuring the velocity field in the quantitative experiments.

II.3 Numerical methods

Two numerical models were used. One of them is suitable to simulate the evolution of a homogeneous fluid in a closed domain with rotation and topography. It will be shown that the organization and decay of the turbulent flows observed in the experiments is reasonably captured by this quasi-two-dimensional approximation. In addition, a regional model was used to simulate the dynamics of the Gulf of California under realistic conditions. The objective in both cases was to show the organization of the flow due to bottom topography effects.

II.3.1 Shallow Water Evolution (SWEVOL)

Decaying quasi-2D turbulent flows with discontinuous topography were numerically simulated with a barotropic, rigid-lid, shallow water model (SWEVOL). The model solves the quasi-2D dynamics expressed in Equations (49) and (50). This finite-differences code has a wide range of initial vorticity distributions, variable topography and boundary conditions available. The code was originally developed by Verzicco and Orlandi (University of Rome) in the 90's for purely 2D flows. It was modified and extended by van Geffen (Eindhoven University of Technology). Afterwards, the model was adapted to include topography effects by Zavala Sansón (see Zavala Sansón and van Heijst, 2002). The numerical domains are analogous to the laboratory experiments, as well as the flow parameters. The aim of these numerical simulations was to reproduce the main physical mechanisms observed in the laboratory experiments.

II.3.2 Regional Ocean Modeling System (ROMS)

The Regional Ocean Modeling System (ROMS) was used to simulate the Gulf of California circulation. The ROMS is a free-surface, terrain-following, primitive equations ocean model that can be used for a diverse range of applications (see Haidvogel *et al.*, 2000). A generalized nonlinear, terrain-following (or sigma) coordinate, which can be configured to provide enhanced resolution at either the sea surface or sea floor, was used earlier in SCRUM model (S-Coordinate Rutgers University Model). ROMS is an expanded version of SCRUM (see Song and Haidvogel, 1994) with a variety of new features. In this subsection the equations solved in ROMS are presented. Additional information on forcings, numerical domains, bottom topographies and flow parameters will be given in chapter V, where the circulation of the GC is studied.

The momentum balance equations in the horizontal plane (x, y) are given by the primitive equations in Cartesian coordinates:

$$\frac{\partial u}{\partial t} + \mathbf{u} \cdot \nabla u - fv = -\frac{\partial \phi}{\partial x} - \frac{\partial}{\partial z} \left(\overline{u'w'} - \nu \frac{\partial u}{\partial z} \right) + \mathcal{F}_u + \mathcal{D}_u, \quad (51)$$

$$\frac{\partial v}{\partial t} + \mathbf{u} \cdot \nabla v + fu = -\frac{\partial \phi}{\partial y} - \frac{\partial}{\partial z} \left(\overline{v'w'} - \nu \frac{\partial v}{\partial z} \right) + \mathcal{F}_v + \mathcal{D}_v, \quad (52)$$

where, (u, v, w) are the (x, y, z) components of the velocity \mathbf{u} ; f is the Coriolis parameter; $\phi(x, y, z, t)$ is the dynamic pressure given by $\phi = (P/\rho_o)$ with ρ_o a reference density; the effects of forcing and horizontal dissipation are represented by the schematic terms \mathcal{F} and \mathcal{D} , respectively. These equations are closed by parameterizing the Reynolds stresses with the vertical shear of the horizontal flow: $\overline{u'w'} = -K_M \frac{\partial u}{\partial z}$ and $\overline{v'w'} = -K_M \frac{\partial v}{\partial z}$.

The advective-diffusive equation gives the time evolution of any scalar concentration $C(x, y, z, t)$

$$\frac{\partial C}{\partial t} + \mathbf{u} \cdot \nabla C = -\frac{\partial}{\partial z} \left(\overline{C'w'} - \nu_\theta \frac{\partial C}{\partial z} \right) + \mathcal{F}_C + \mathcal{D}_C, \quad (53)$$

with $\overline{C'w'} = -K_C \frac{\partial C}{\partial z}$ being the turbulent tracer flux representation.

The equation of state is given by

$$\rho = \rho(T, S, P) \quad (54)$$

with T the temperature and S the salinity, and the total "in situ" density given by

$$\rho = \rho_o + \rho(x, y, z, t).$$

The vertical pressure gradient is given by

$$\frac{\partial \phi}{\partial z} = -\frac{\rho g}{\rho_o} \quad (55)$$

where the Boussinesq approximation is used; g is the acceleration of gravity.

The continuity equation for an incompressible fluid is used:

$$\frac{\partial u}{\partial x} + \frac{\partial v}{\partial y} + \frac{\partial w}{\partial z} = 0. \quad (56)$$

Equations (51)-(56) are subjected to boundary conditions on the sea surface $z = \eta$, and at the sea bed $z = -h$. At the surface the conditions are

$$K_M \frac{\partial u}{\partial z} = \tau_s^x(x, y, t) \quad (57)$$

$$K_M \frac{\partial v}{\partial z} = \tau_s^y(x, y, t) \quad (58)$$

$$K_H \frac{\partial C}{\partial z} = 1/\rho_0 C^*, \quad (59)$$

where τ_s^x and τ_s^y are the components of wind stress acting on the free surface in the x and y directions, respectively; for temperature T , $C^* = Q_T/C_p$ where Q_T is the heat fluxes and C_p is the heat capacity of the sea water; for salinity S , $C^* = e - p$ where e and p are the evaporation and precipitation rates, respectively.

At the sea bed the conditions are

$$K_M \frac{\partial u}{\partial z} = \tau_b^x(x, y, t) \quad (60)$$

$$K_M \frac{\partial v}{\partial z} = \tau_b^y(x, y, t) \quad (61)$$

$$K_H \frac{\partial C}{\partial z} = 0, \quad (62)$$

where $\tau_b^x = (\gamma_1 + \gamma_2 \sqrt{u^2 + v^2})u$ and $\tau_b^y = (\gamma_1 + \gamma_2 \sqrt{u^2 + v^2})v$, and γ_1 and γ_2 are coefficients of linear and quadratic bottom friction, respectively.

Chapter III

Self-organization and decaying process in a rectangular domain with a step topography

*This chapter is an adapted version of an article published in *Physics Of Fluids**

(Tenreiro et al., 2010)

III.1 Introduction

This chapter addresses the organization of decaying quasi-2D turbulence in rectangular containers with discontinuous topography. The objective is to describe the process in this system and to determine the preferential final state of the flow field due to the presence of the step within a rectangular domain. The relevance and antecedents of this problem are thoroughly discussed in chapter I. The study is carried out by means of laboratory experiments in a rotating tank with aspect ratio $\delta = 2$ and by numerical simulations. In subsequent chapters we analyse different geometries. The laboratory experiments provide physical evidence of the main features expected on 2D decaying turbulence with topography. The numerical simulations, based on a barotropic quasi-two-dimensional model with topography, will help to gain a better understanding of the processes involved. Most of these are related with the dynamics of dipolar structures generated during the flow evolution. The numerical results show that the flow organization depends crucially on the step height. An important result is that a flow along the step forces the existence of a preferential solution for long times (several rotation periods).

The chapter is organized in four main sections. In section III.2 the experimental setup and two particular experiments are discussed in terms of self-organization and topography signal. Numerical simulations with a similar arrangement are presented in section III.3 where the main features on the flow organization are described. Section III.4 is reserved for the discussion of the results and to present the conclusions.

III.2 Laboratory experiments

III.2.1 Experimental set-up

The laboratory experiments were performed in a rectangular, rotating tank with horizontal dimensions $150 \times 75 \text{ cm}^2$ filled with fresh water. The aspect ratio of the tank is $\delta = 2$, defined as the ratio between length and width. The bottom of the container was divided in two square regions, deep and shallow, by means of a 3 cm step. The height of the water column at the deepest part was $H_0 = 20 \text{ cm}$ (Figure 3 shows a schematic picture of the experimental set-up).

The rotation rate of the tank around the vertical axis was fixed at $\Omega = 0.5 \text{ rad s}^{-1}$, which corresponds to a Coriolis parameter $f = 2\Omega = 1 \text{ s}^{-1}$. The decay induced by bottom friction is associated with the Ekman period, $T_E = H_0/(\nu\Omega)^{1/2} \approx 280 \text{ s}$, for $\nu = 0.01 \text{ cm}^2\text{s}^{-1}$ (kinematic viscosity of water at $20 \text{ }^\circ\text{C}$) which is roughly the duration of a typical experiment. The time scale associated to the Ekman decay is much longer than the rotation period, $T = 2\pi/\Omega \approx 12 \text{ s}$. The experimental procedure consisted of setting the tank in rotation at a constant angular speed for about 30 min before starting an experiment, in order to ensure that the fluid has reached a state of solid body rotation. The parabolic free-surface (1 to 3 mm) effects are ignored, assuming

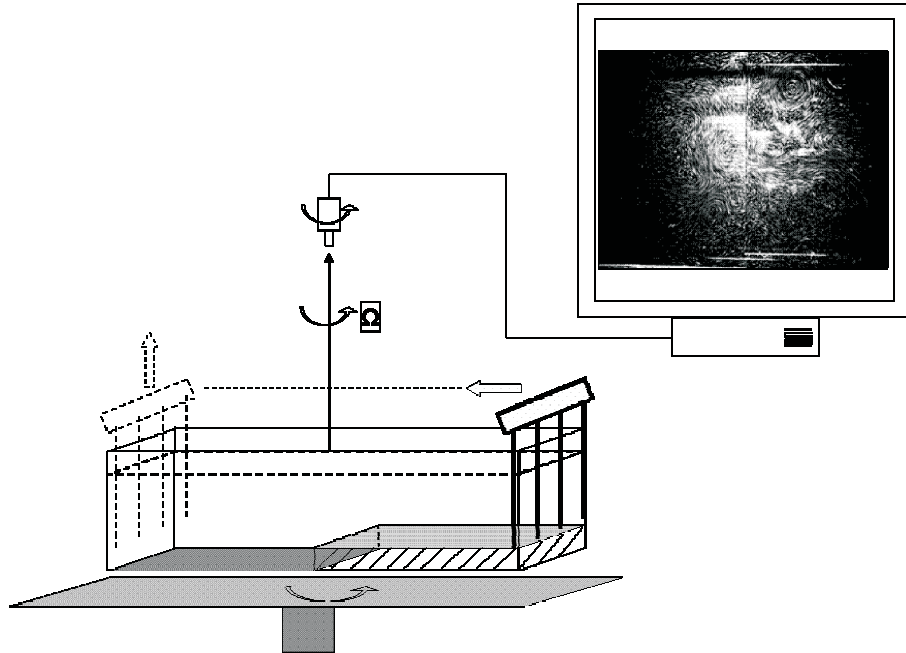


Figure 3. *Schematic picture of the experimental set-up. The initial flow is generated by moving the set of vertical bars from right to left.*

that the change in depth due to the step (3 cm) in the bottom topography is more important.

A disordered small-scale initial flow field is generated by passing a grid of vertical bars (15 bars with diameter $d = 6$ mm and 4 cm spacing between each one) through the fluid, parallel to the longer sides of the container. The grid is moved with constant speed by an electric motor mounted on the table (a similar configuration is used in Maassen *et al.*, 2003). When the bars arrive at the other side of the container, the grid is removed by vertically lifting it out of the fluid (Figure 3). The initial characteristic vorticity ω_0 is about 0.5 s^{-1} , which corresponds to a Rossby number $R_o = \omega_0/f$ always smaller than 1, ensuring the two-dimensionality of the flow.

In the presence of variable topography there are always three-dimensional effects. Nevertheless, for a rotating fluid system with small to moderate Rossby number and small Ekman number, the flow presents a strong columnar motion, which is modulated

by depth changes.

For qualitative experiments, the vortices are visualized by adding fluorescent dye to the fluid. Quantitative experiments are performed using passive tracers ($\sim 250\mu\text{m}$) floating on the surface. The flow field evolution was recorded with a co-rotating camera mounted at some distance above the tank. Particle image velocimetry (PIV) was used for quantitative experiments. The main results were clearly reproducible in all experiments.

III.2.2 Results

Several experiments were performed in order to observe the different processes involved in the self-organization of the flow field. Two typical experiments are discussed, one being qualitative and the other leading to quantitative information about the flow evolution.

Figure 4 shows a sequence of photographs from a typical qualitative experiment (a dye visualization of the flow is used). Hereafter, in all figures the lower (upper) side of the domain corresponds with the deep (shallow) region, the horizontal black line represents the step position and time is made dimensionless as $t = \frac{t^*}{T}$, where t^* is time and T the rotation period of the tank. Initially ($t = 3$), the small-scale motions, characteristic of the flow field originated by the passage of the rake through the fluid, are observed. At $t = 6$ it is already possible to identify small coherent structures like dipoles in both regions of the domain. For $t = 10$ new structures grow and the effect of the step results in a weak flow along the topography, which is sketched with an arrow. For longer times, the flow organizes into larger structures in both regions. Note, for instance, the large dipole at the shallow side ($t = 15 - 25$) and the smaller dipole near

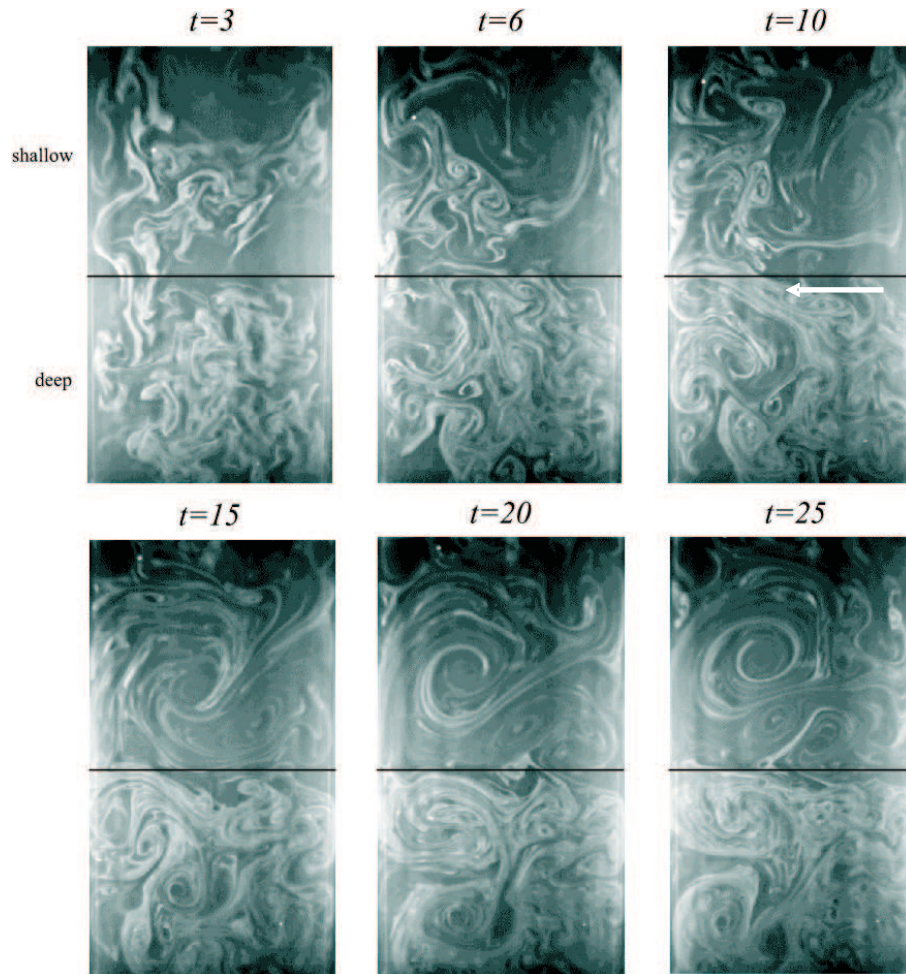


Figure 4. *Sequence of top view photographs showing the evolution of an experimental 2D decaying turbulent flow with rotation and discontinuous topography. The black line divides the domain into a deep (lower) and shallow (upper) regions. This experiment is visualized with dye distributed randomly inside the domain before passing the grid.*

the left wall at the deep region ($t = 15 - 20$). The important point to remark here is that the flow generated along the step effectively separates the shallow and deep regions as larger vortices are formed.

Figure 5 presents the velocity and vorticity fields from a quantitative experiment after several rotation periods. It shows the advection towards the left wall of a cyclonic (anticyclonic) structure at the deep (shallow) region, near the step. The presence of the step generates a flow towards the negative x -direction maintaining the shallow region

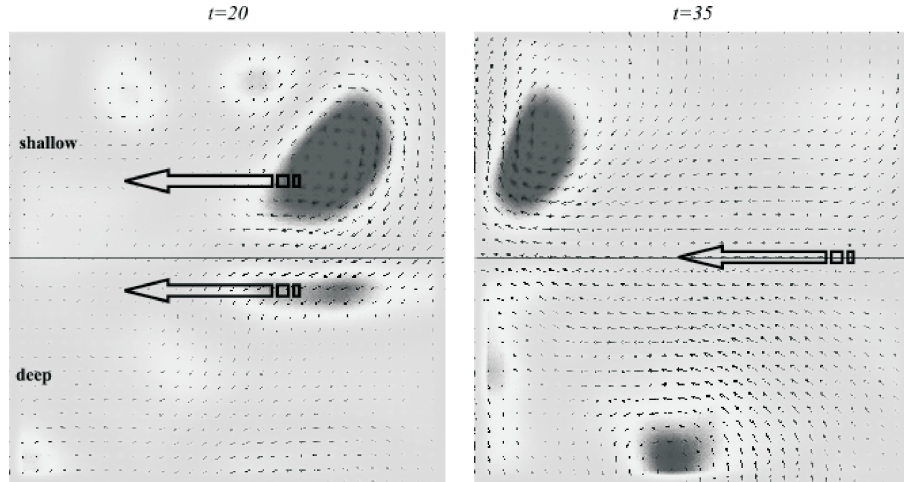


Figure 5. *Top view data from PIV showing the step region of an experimental flow field at two different times. The small arrows represent the velocity field $\mathbf{u} = (u, v)$. Dark regions represent strong positive (negative) vorticity center at the deep (shallow) side of the step. The black line indicates the position of the step. The big black arrows schematize the flow behavior. The area is a rectangle with dimensions $\sim [75 \text{ cm}, 80 \text{ cm}]$.*

on its right, which results in the absence of structures above the step. For these times ($t = 20 - 35$) the flow in both regions behaves almost independently. Note that the dipole moves along the step with each one of its parts at a different region: the cyclone (anticyclone) is always at the deep (shallow) part of the domain.

The two experiments shown above are representative of the observed interactions, among which the most remarkable are the flow along the step and the formation of fewer and larger vortices at both sides of the discontinuity. However, after repeating several experiments it was not possible to determine a clear trend towards a preferred configuration of the flow for long times. Thus, the final states were configured by one or two vortices at each side of the step, either cyclonic, anticyclonic or both. This is shown in Table I, which contains a list of the number of vortices, sign of vorticity and domain region where they were found for $t = 25$ in 10 experiments. The vortices are counted by identifying the strongest vortical structures for each experiment. The percentage of vortices in both regions indicates a slightly higher probability to find

cyclones (anticyclones) in the deep (shallow) part of the domain. This result, however, is not conclusive at all. One important factor in the experiments is the presence of Ekman friction. Indeed, bottom friction effects for long times strongly reduce the energy of the flow, halting the organization process, and therefore inhibiting the formation of even larger vortices (recall that $t = 25 \simeq 0.9T_E$). In order to avoid this problem, numerical simulations without Ekman effects are carried out. The results are shown in the following section.

Table I. *Summary of the laboratory results in terms of number, sign of vorticity and region of the vortices for $t = 25$. +D (+S) denotes cyclones in the deep (shallow) region, while D- (S-) indicates anticyclones in the deep (shallow) region.*

Exp.	+ D -	+ S -
1	1 - 1	1 - 1
2	1 - 0	1 - 1
3	1 - 2	2 - 1
4	0 - 1	0 - 1
5	1 - 1	1 - 1
6	1 - 0	1 - 1
7	1 - 0	0 - 1
8	1 - 0	2 - 2
9	0 - 1	1 - 1
10	1 - 1	0 - 1
# vortices	15	20
%	53 - 47	45 - 55

III.3 Numerical simulations

In this section, numerical simulations of decaying quasi-2D turbulence with discontinuous topography are presented. The flow is represented by means of a barotropic, shallow water model. The equations in the $\omega - \psi$ formulation solved with a finite differences

code (see e.g., Zavala Sansón and van Heijst, 2002) are:

$$\frac{\partial \omega}{\partial t} + J(q, \psi) = \nu \nabla^2 \omega, \quad (63)$$

$$\omega = -\frac{1}{h} \nabla^2 \psi + \frac{1}{h^2} \nabla h \cdot \nabla \psi, \quad (64)$$

where $\omega = \frac{\partial v}{\partial x} - \frac{\partial u}{\partial y}$ is the relative vorticity with (u, v) the horizontal, depth-independent velocity, $q = \frac{\omega+f}{h}$ the potential vorticity, $h(x, y)$ is the fluid depth, ψ is a transport function and J the Jacobian operator. Note that the local depth h is time independent, according with the rigid lid approximation, and therefore only depends on the local depth of the fluid. This formulation can be reduced to the quasi-geostrophic approximation when the step height h_B is much smaller than the maximum fluid depth, $\frac{h_b}{H} \ll 1$. The shallow-water model is adopted here, however, since it is a more appropriate approximation for high steps. A comparison of the two models in the presence of abrupt topography is reported in Zavala Sansón *et al.* (2010).

The simulations represent a rectangular domain with horizontal dimensions $L \times \delta L$ with $L = 0.5$, and $\delta = 2$ being the aspect ratio of the tank. A step-like topography divides the flow domain in two geometric squares with aspect ratio 1. In all simulations the height of the water column in the deep region is $H_0 = 0.2$. The rotation rate around the vertical axis is fixed at $\Omega = 0.5$, corresponding to a Coriolis parameter $f = 2\Omega = 1$. The rotation period is $T = 4\pi/f$. The flow decay is induced by lateral friction effects where viscosity is $\nu = 10^{-6}$. No-slip conditions are imposed at the side walls. Ekman friction effects are not considered. The discretization consists of 257×257 gridpoints and the dimensionless time step is always $\Delta t = 10^{-3}$ for all simulations. Due to the discretization, the step-like topography in the numerical simulations is actually a very narrow slope, whose width is much smaller than the size of the vortices.

The initial condition (IC) used in all simulations is an 8×16 array of cyclonic and

anticyclonic Gaussian vortices with maximum vorticity $|\omega| = 1$ and diameter $a = 0.05$. Similar initial distributions are used in several laboratory experiments where vortices are forced electromagnetically (Tabeling *et al.*, 1991; Hansen *et al.*, 1998) or by dragging a rake of vertical bars through the surface (as in this study; Maassen *et al.*, 2003). Twelve different initial conditions are used, with the relative positions between adjacent vortices slightly and randomly changed. The random perturbations of the positions are about 15% of the vortex diameter. The Reynolds number $Re = 2500$ is defined as $Re = LU_{rms}/\nu$, with $U_{rms} = 0.005$ being the characteristic velocity of the initial flow field.

Two step heights are used, $\Delta h = \frac{1}{20}H_0$ and $\Delta h = \frac{1}{4}H_0$. Since these values determine substantial differences in the flow evolution, they will be referred to as *low* and *high step*, respectively. Table II shows a summary of the numerical parameters used for the simulations.

Table II. *Characteristic parameters of the numerical simulations.*

Domain	$L \times \delta L$	0.5×1
Maximum depth	H_0	0.2
Kinematic viscosity	ν	10^{-6}
Rotation period	$T = 2\pi/\Omega$	12.5
Vortex diameter	a	0.05
Initial rms velocity	U_{rms}	0.005
Step height	Δh	low (high) 0.01 (0.05)

III.3.1 General features

Figure 6 shows the evolution of the relative vorticity field for a low step using lateral no-slip boundary conditions in a particular simulation. The black line at $y = 0.5$

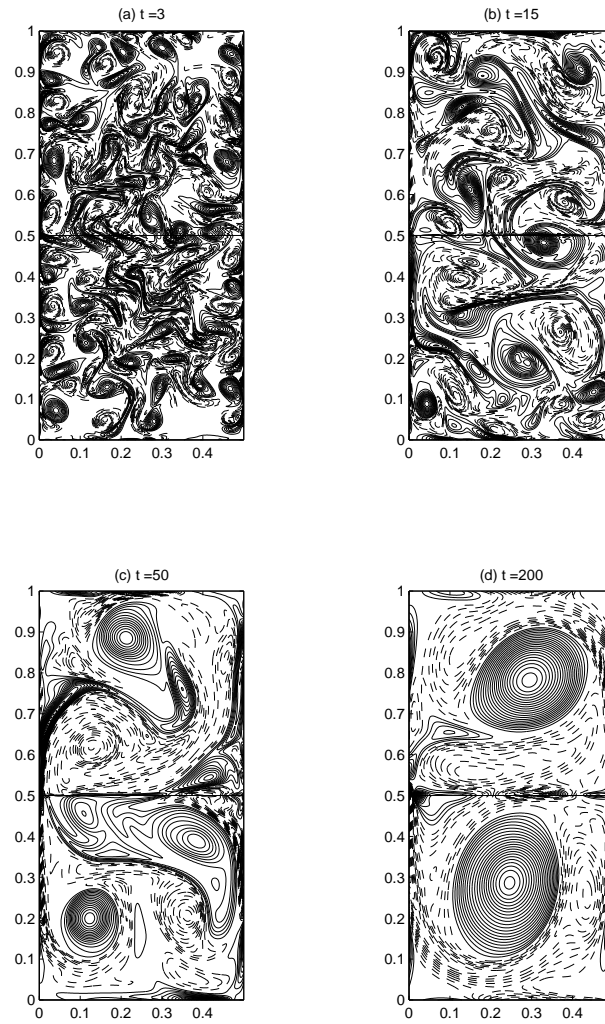


Figure 6. *Vorticity contours from a simulation with a low step and no-slip boundary conditions. Dashed contours represent negative values of vorticity, and solid contours represent positive values. The contour level increment is: (a)-(b) 0.02, (c) 0.01 and (d) 0.002.*

represents the position of the step that divides the domain in deep and shallow regions. Three main processes can be observed: 1) fast flow auto-organization (panels a and b); 2) strong interaction of the vortices with the lateral boundaries and the topography, with the formation of coherent structures with sizes comparable with the square regions (panel c); and 3) final configuration of two coherent structures more or less placed at the geometrical centre of the square deep and shallow regions (panel d).

When the simulation starts, vortices with the same sign of vorticity merge and gene-

rate larger vortices. Vortices with different sign form self-propagating dipolar structures, which in turn will interact with other vortices. Initially, the flow is dominated by these dipolar structures. When reaching the step topography, some of them are able to cross it, while others are reflected, depending on the step height and the strength and size of the structures (Tenreiro *et al.*, 2006). The effect of the boundaries when a vortex approaches a wall is the generation of thin filaments with opposite sign vorticity. These intense filaments are injected into the flow interior, sometimes forming new dipolar structures (Clercx *et al.*, 1998). At the step region, a flow along the topography is generated. This flow, which maintains the shallow region at the right, forces the formation of two structures, a cyclone at the deep and an anticyclone at the shallow part of the domain (panel c). Due to the interaction with the left wall the anticyclone generates at the shallow region a cyclonic structure which eventually prevails in this area. The flow field reaches a final pattern consisting of two large positive structures surrounded by negative relative vorticity.

In order to see the effect of the step height on the flow evolution, a numerical run with the same initial condition but now using a high step topography is performed (see Figure 7). Initially, the flow behavior is very similar to the low step case (compare panel a in Figures 6 and 7). However, after 15 rotation periods it can be noticed that there are no structures above the step (panel b), which indicates a clear separation between both regions. The flow along the step is generated and intense interactions with the left wall are observed (panel c). In this case, the final pattern consists of two large scale structures: an anticyclone at the deep and a cyclone at the shallow region (panel d). It is important to remark that the main effect of the high step is the earlier separation of the shallow and deep regions. A more precise time scale of this process in terms of the step height is given in next section. Note also that the final distribution has a very

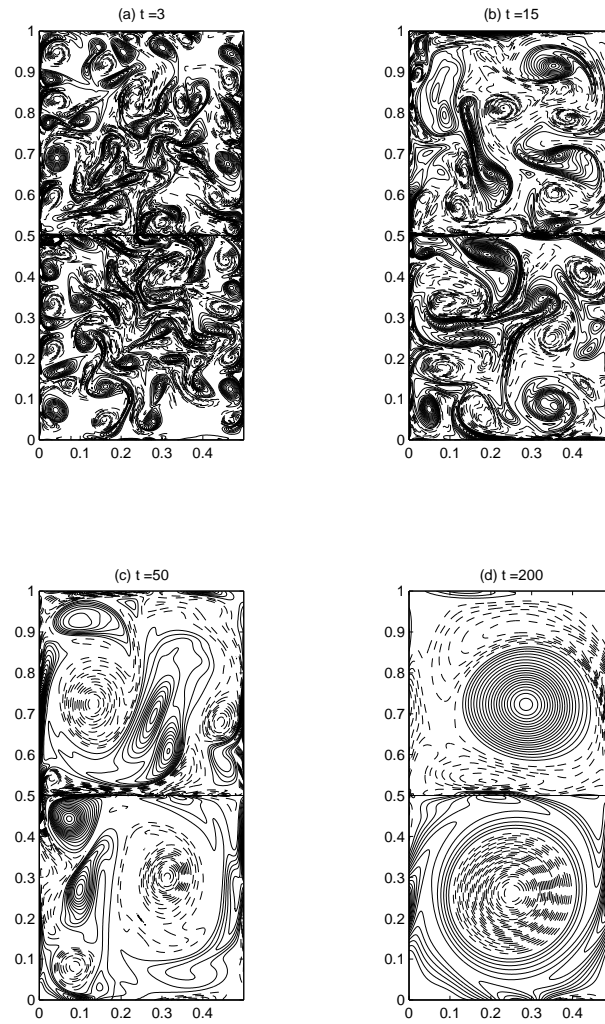


Figure 7. As Figure 6, but now for a high step.

different pattern compared with the low step simulation.

III.3.2 Flow at the step region

In order to get more information about the step influence on the flow evolution and organization, the velocity field along six parallel and consecutive grid lines adjacent to the step in the deep region is analysed. In Figure 8 the u and v components are examined independently for the same simulations shown in Figures 6 and 7. The plots present these components (horizontal axis) along the step during the whole simulation

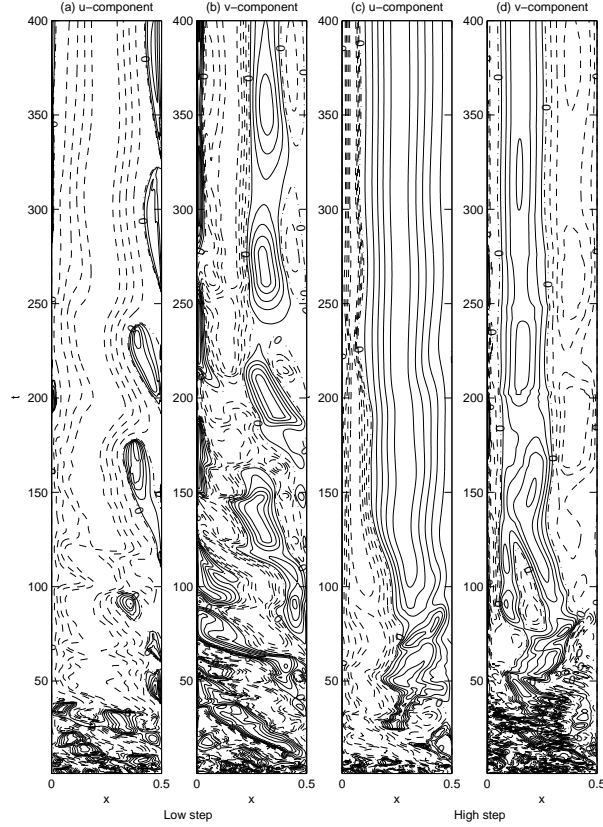


Figure 8. *Normalized mean velocity components along six grid-lines adjacent and parallel to the step in the deep region for the simulations shown in Figures 6 and 7. The velocity is normalized with the maximum value for each transect. The time step is $\Delta t = 1$. Dashed contours represent negative values and solid contours represent positive values. Dashed-point contours represents the zero. The contour level interval is 0.2.*

(vertical axis). The flow along the low step is clearly shown by the negative values of the u -component from $t \sim 40$ (panel a). Before $t \sim 40$, the existence of small scale structures associated with the vortices crossing above the step is observed. Note also that near the right wall there are some periodic inversions of the u -component, which are also correlated with the v -component. This behaviour is associated with the existence of topographic waves along the step. Panel (c) shows the u -component of the velocity field, in this case along a high step. It can be seen that negatives values of this component appear from $t \sim 5$ due to the step influence. Before $t \sim 5$, the existence of

small structures is related with the initial condition. For $t \sim 25$ a positive flow near the central point of the step is formed and grows in time. This positive flow at the step is directly associated with the presence of an anticyclone at the deep region (see Figure 7).

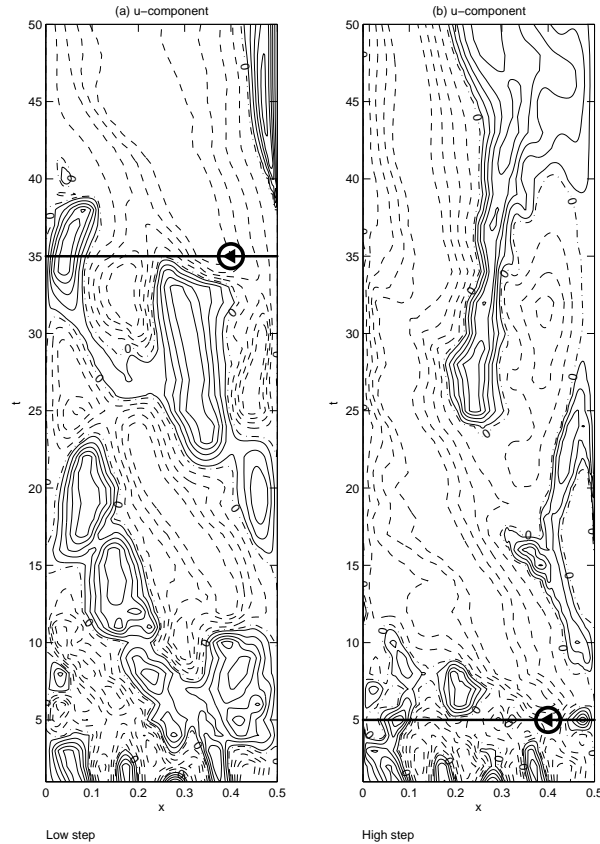


Figure 9. Zoom of Figure 8 panels (a) and (c). The line indicates the separation time between regions and the circle the initial position of the jet for a low (a) and high (b) steps.

The main point to emphasize here is the time at which the negative flow along the step is established: $t \sim 35$ for the low and $t \sim 5$ for the high step case (see Figure 9). This time is a good estimation of the moment at which the flows in the shallow and deep regions begin to evolve almost independently, which mainly depends on the step height.

III.3.3 Final configurations

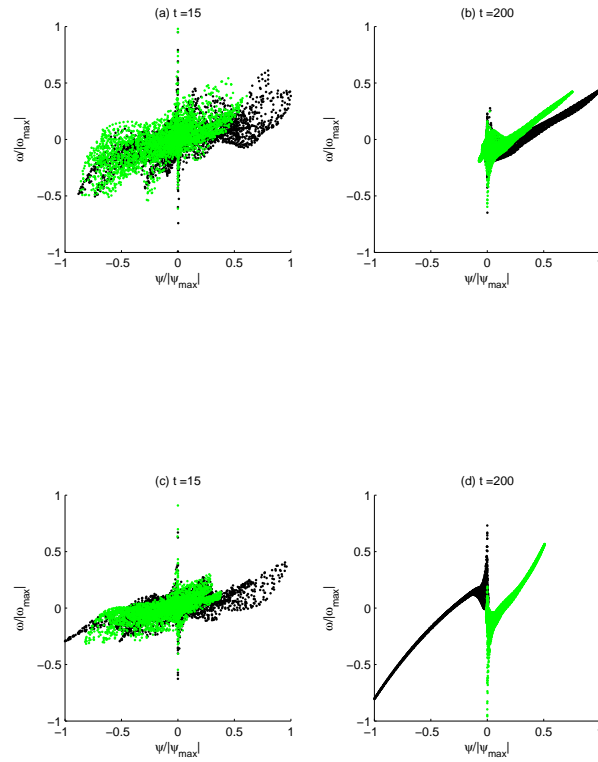


Figure 10. Scatter plots at two different times of simulations shown in Figures 6 and 7. Panels (a)-(b): low step; panels (c)-(d): high step. The values are normalized with maximum absolute values. Dark (grey) points are located in the deep (shallow) region.

The final flow configuration is well-represented by means of scatter plots. The relation between relative vorticity (ω) and transport function (ψ) is shown in Figure 10 for a low (panels a-b) and a high (panels c-d) step. Note that points in the deep and shallow regions are marked with different colours. For $t = 15$ the disordered character of the flow field can be noticed by the absence of a clear relationship between both quantities. However, this dispersion is smaller for the high step case, which indicates a faster organization of the flow field. For later times, $t = 200$, a nearly linear relationship is found separately for the two resulting coherent structures. The important point to remark is the different distribution of large vortices at the end of the simulation: two cyclones for the low step, and for the high step one cyclone in the deep region and an

anticyclone in the shallow region.

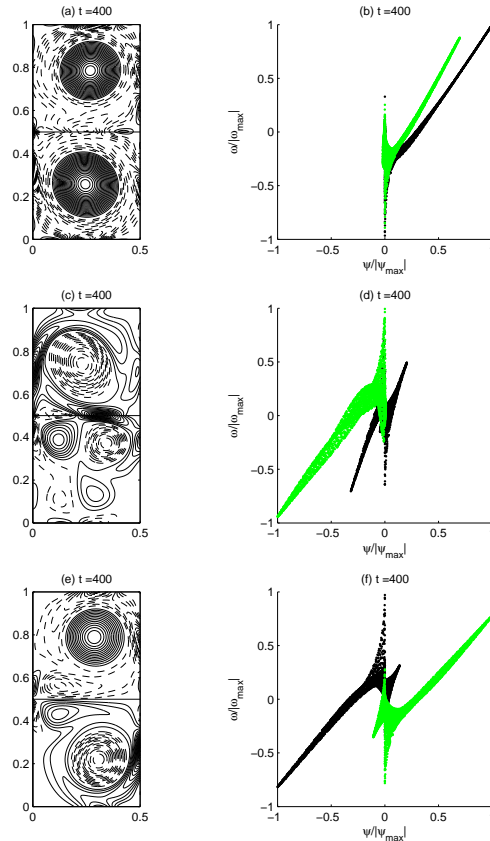


Figure 11. *Vorticity contours and scatter plots of three different simulations with a low step-like topography. Dashed contours represent negative values of vorticity, and solid contours represent positive values. The contour level increment is 0.001. Black (grey) dots in scatter plots are located in the deep (shallow) region.*

However, the final configurations shown above are not always obtained when slightly varying the initial conditions. To illustrate this assertion, figure 11 shows the relative vorticity contour lines and the corresponding scatter plots for three different numerical simulations at very long times using a low step. Recall that the simulations differ in the position of the vortices of the initial condition, which are weakly and randomly perturbed. It can be seen that all the simulations present a different final cell pattern distribution. Panel (a) shows the formation of cyclonic vortices at each side of the

step. For panels (b) and (c), intermediate configurations of different structures are found. The dominant vortices are easily identified with the corresponding scatter plots. Similar results for different numerical simulations using a high step were obtained: simulations with small variations in the initial conditions also presented different final cell pattern distributions.

Given the sensitivity of the final flow pattern for slightly different initial conditions, an ensemble of 12 simulations was carried out for each topography. In Table III a summary of the numerical results in terms of the final cell pattern distribution is presented. This table shows that the flow evolves towards a preferential final distribution of vorticity given by one coherent structure in each region; the correlation between the sign of these structures and the topography (deep vs. shallow) appears to be weak

Table III. *Summary of the numerical results for low and high steps in terms of number, sign of vorticity and region of the vortices at time $t = 400$. +D (+S) cyclone at the deep (shallow) region; D- (S-) anticyclone at the deep (shallow) region. The symbol 0 denotes cases in which no structures were found.*

IC	Low step		High step	
	+D-	+S-	+D-	+S-
1	1 - 0	0 - 1	1 - 1	0 - 1
2	1 - 0	2 - 2	0 - 1	0 - 1
3	1 - 1	0 - 1	0 - 1	0 - 1
4	1 - 0	1 - 0	0 - 1	1 - 0
5	0 - 1	1 - 1	1 - 0	1 - 0
6	1 - 0	0 - 1	0 - 1	0 - 1
7	1 - 0	1 - 0	0 - 1	1 - 0
8	0 - 1	1 - 0	0 - 1	0 - 1
9	1 - 0	0 - 1	0 - 1	0 - 0
10	1 - 1	1 - 0	1 - 0	1 - 0
11	0 - 1	1 - 0	1 - 0	1 - 0
12	1 - 0	1 - 0	0 - 1	1 - 0
# vortices	14	16	13	11
%	64 - 36	56 - 44	31 - 69	55 - 45

III.3.4 Generalization based on ensemble averages

In order to get more general information about the processes involved in the turbulent decay in the presence of a step, the time evolution of two global quantities, the kinetic energy (E) and the enstrophy (Z), is investigated. These functionals are defined as

$$E = \frac{1}{2} \int (u^2 + v^2) dx dy, \quad (65)$$

$$Z = \frac{1}{2} \int \omega^2 dx dy. \quad (66)$$

The ratio Z/E can be interpreted as $1/l^2$, where l is the mean scale of the structures of the turbulent flow field. The quantity l must grow in time due to the inverse energy cascade and it is indicative of the efficiency of the self-organization process.

The ensemble average is based on twelve runs using twelve slightly different initial conditions, as mentioned above. Figure 12 shows the decay of global quantities for a low and high step. In panel (a) the normalized kinetic energy and enstrophy decay is presented. As can be seen, the decays are very similar in both quantities. From the ratio $Z(t)/E(t)$ (panel b) different features can be noticed. The total algebraic decay rate of Z/E between $4 \leq t \leq 400$ for a low step is $\sim t^{-0.58}$, while for a high step is $\sim t^{-0.63}$. These values are quite similar. Nevertheless, they are somewhat larger than the one reported by Maassen (2000) for a rectangular container with the same aspect ratio ($\delta = 2$) but without topography ($t^{-0.48}$). In other words, the presence of the step increases the decay of this quantity or, equivalently, the efficiency of the organization of larger structures with respect to the strictly 2D case. Besides, the value measured by Clercx *et al.* (1999) for a square container ($\delta = 1$) without bottom topography is $t^{-0.63}$. Therefore, the exponents found here suggest that the flow in each region tends to behave independently, as in two separated square boxes. Panel (c) shows the mean scale of the structures. For $t > 40$ slightly larger structures are found for the high step

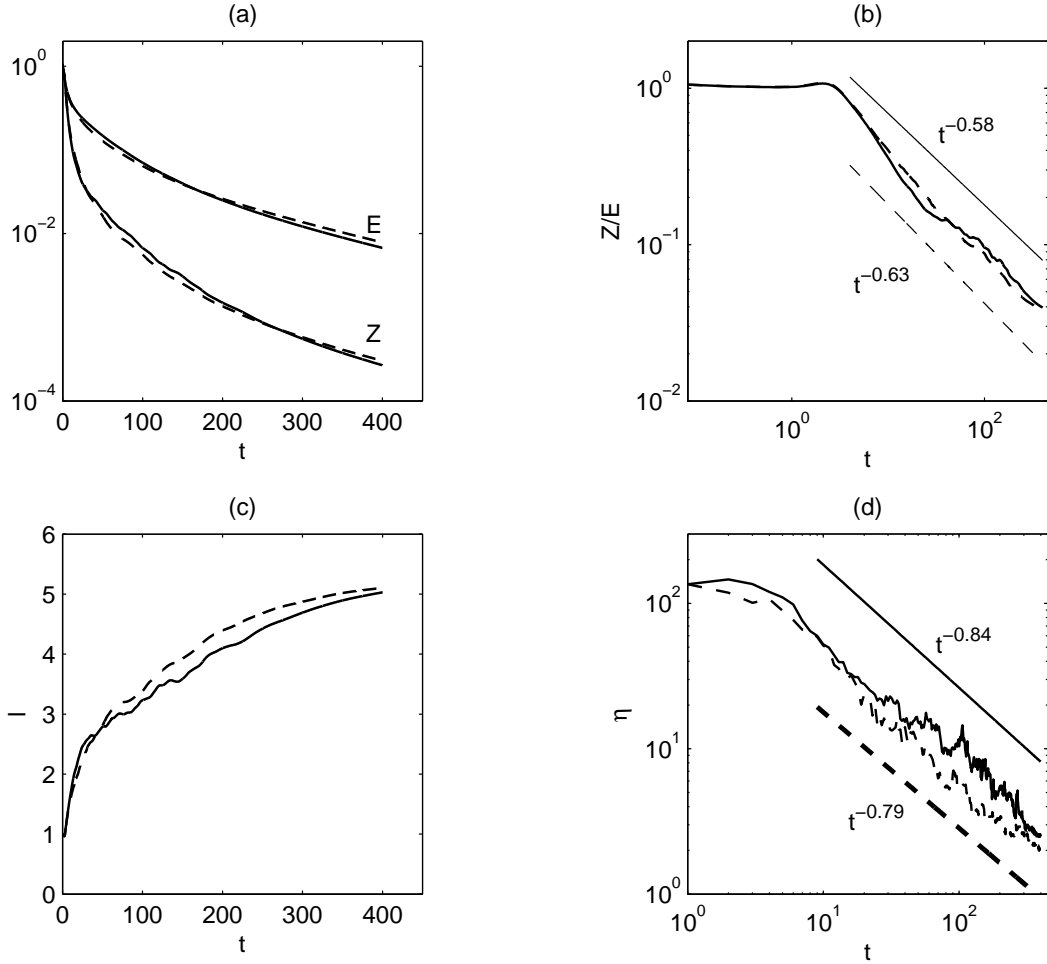


Figure 12. Time evolution of global quantities with low (solid) and high (dashed) steps: (a) Normalized kinetic energy ($E/E_{(t=0)}$) and normalized enstrophy ($Z/Z_{(t=0)}$); (b) Ratio of Z/E ; (c) Mean scale structures; (d) Number of vortices. The data are computed from ensemble averages of twelve runs with slightly different initial conditions.

case.

Another analysed quantity is the number of vortices as a function of time (panel d). The vortex count is done by making use of the Okubo-Weiss function, $Q = s_1^2 + s_2^2 - \omega^2$, where the strain components are defined as $s_1 = u_x - v_y$ and $s_2 = u_y + v_x$. $Q(x, y, t)$ allows to distinguish between rotation ($Q < 0$) and strain ($Q > 0$) dominated regions (e.g., Zavala Sansón and Sheinbaum, 2008). A vortex is counted in closed regions where $Q_{min} \leq Q \leq Q_{min}/10$. As the flow organizes, it is expected that the number of vortices

decreases. It can be seen that the number of vortices in both regions is reduced at almost the same rate. Nevertheless, the high step case presents always fewer vortices indicating a more effective self-organization of the flow.

III.3.5 Step-limit and step-signal

The separation of the flow in two different regions due to the step presence was found to occur at $t \sim 5$ ($t \sim 35$) for a high (low) step. The physical mechanism associated with this behavior consists of the cease of vorticity exchanges between regions as flow structures are less able to cross the step from one side to the other. This process depends on the flow properties such as circulation and vorticity and on the step height. In order to relate the separation time T^* , the step height Δh and the characteristic strength of the flow ω^* at this time, we define the latter as the integrated relative vorticity in the deep region:

$$\omega^* = \omega_{deep} = \int_0^{0.5} \int_0^{0.5} \omega dx dy. \quad (67)$$

For this analysis we could also use $\omega_{shallow}$, which is equal to $-\omega_{deep}$ because the total circulation is zero $\int_0^{0.5} \int_0^{1.0} \omega dx dy = 0$. Note that $\omega^*(0) \sim 0$ due to the initial conditions. For latter times we expect an increase of ω^* as fluid columns crossing towards the deep region are stretched, gaining positive relative vorticity.

Figure 13 shows the ensemble average of ω^* from twelve runs for each step height. An additional set of simulations with a very low step ($\Delta h = 0.005$) is also included. The time evolution of ω^* for the different steps is shown in panel (b). It can be noticed that, as expected, ω^* increases in time and reaches a maximum. Afterwards it decays without strong oscillations for each step height. The existence of this maximum suggests the time after which there are no more structures crossing the step. Indeed, this time is

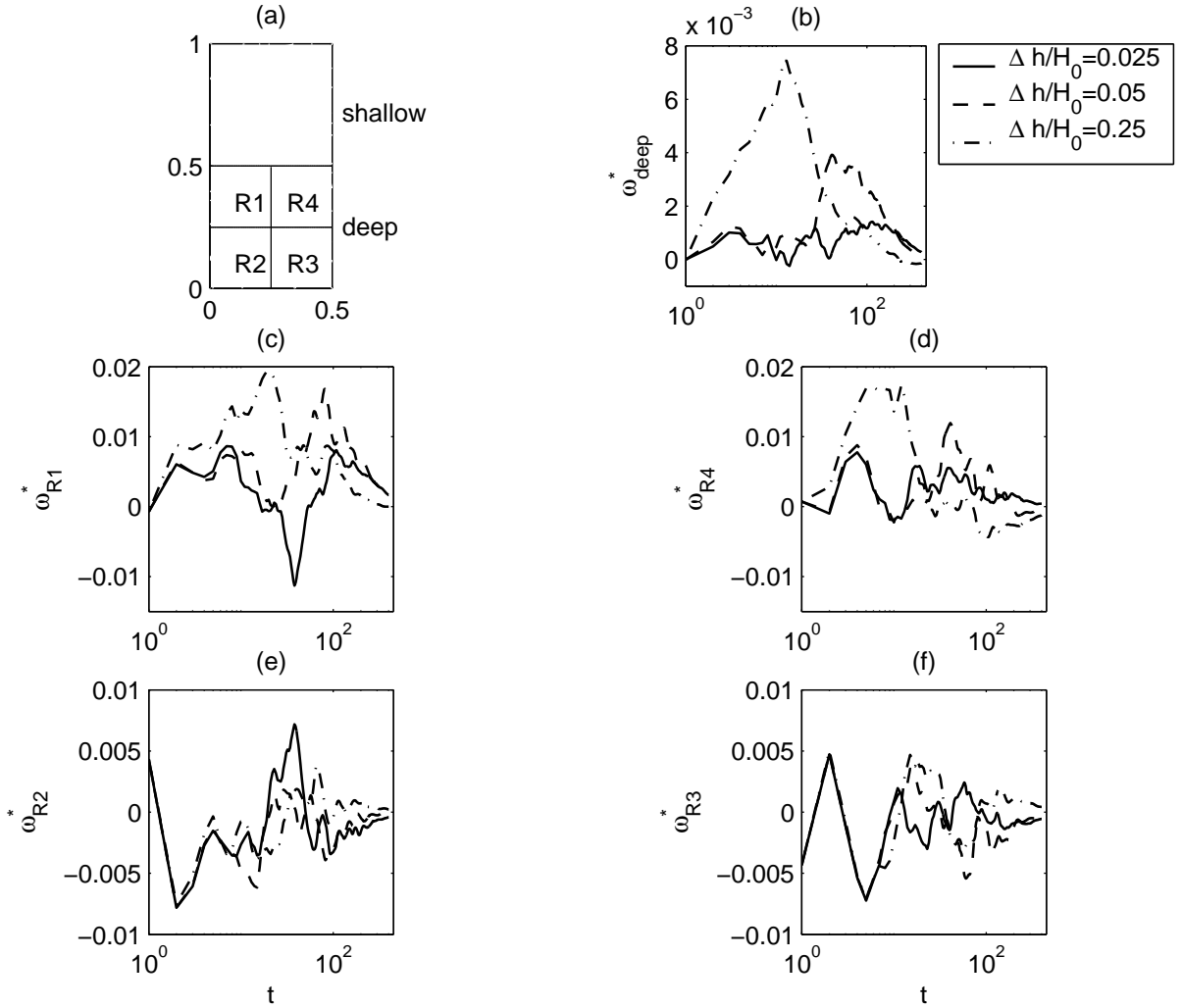


Figure 13. *Time evolution of integrated relative vorticity in different regions due to different step heights. (a) Schematic representation of the integration regions. Vorticity adjustment in (b) deep, (c) R1, (d) R4, (e) R2 and (f) R3 regions.*

$t \sim 10$ for the high step and $t \sim 40$ for the low step; these values correspond well with those previously found with independent measures. The magnitude of the maximum ω^* depends on the size of the step: larger steps induce stronger exchanges of vorticity across the topography. Panels (c)-(f) show the integrated vorticity on four sub-regions (see panel (a) for a schematic representation of the different integration areas). It is clear that the increment of ω^* is mainly associated with the R1 and R4 regions, where a stronger signal is measured compared with the other two placed away from the step.

Another interesting feature is that R2 and R3 regions present a strong correlation at early times. This means that the step signal takes several rotation periods to be noticed at the southern wall.

III.3.6 Statistical analysis of the final configuration

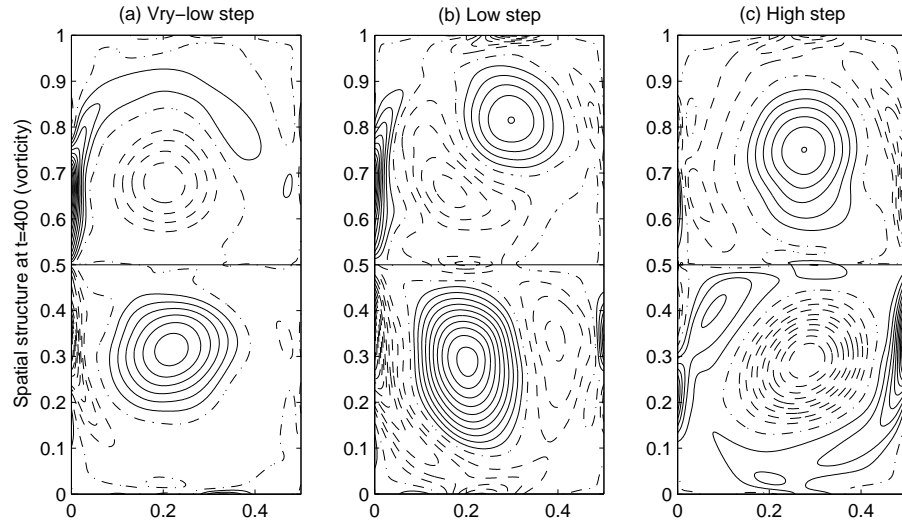


Figure 14. *Mean spatial vorticity distribution at $t=400$ for (a) very-low step, (b) low step and (c) high step. Dashed contours represent negative values of vorticity, dashed-dotted contours represent zero values, and solid contours represent positive values. The contour level increment is: (a) 0.001 and (b)-(c) 0.0008.*

In the preceding sections it was found that small differences in the initial conditions lead to significant differences in the final vorticity distribution. Figure 14 shows the final mean vorticity distribution ($t = 400$) calculated from ensembles of 12 simulations for the three steps discussed above. As expected, few large scale structures remain at each side of the topography. However, this average does not show the strong variability of the final configurations observed from individual simulations. In order to quantify these differences and to find spatial structures that explain them an Empirical Orthogonal Functions technique is used (Berkooz *et al.*, 1993; Emery and Thomson, 2001; Hartmann, 2008).

The EOF analysis seeks structures that explain the maximum amount of variance in a two-dimensional data matrix. A space-realization array at a single time ($t = 400$) is used where columns are the space vorticity vectors ($m = 1, 2, \dots, 257^2$) and rows the results of each initial condition used ($n = 1, 2, \dots, 12$):

$$\mathbf{X} = \begin{array}{c} \text{Realization} \rightarrow \\ \left[\begin{array}{cccc} \omega_{1,1} & \omega_{1,2} & \cdots & \omega_{1,N} \\ \omega_{2,1} & \omega_{2,2} & & \\ \vdots & & \ddots & \\ \omega_{M,1} & \cdots & & \omega_{M,N} \end{array} \right] \downarrow \text{Space} \end{array}$$

where $\omega_{m,n}$ is the vorticity at the grid position m for the simulation n . The M dimension represents the data structure and N the realization.

By using the Singular Value Decomposition for $M > N$, matrix \mathbf{X} can be written as

$$\mathbf{X} = \mathbf{U}\Sigma\mathbf{V}^T \quad (68)$$

where the columns of $\mathbf{U}_{(M \times M)}$ and $\mathbf{V}_{(N \times N)}$ are the eigenvectors (singular vectors) of the covariance matrices $\mathbf{X}\mathbf{X}^T$ and $\mathbf{X}^T\mathbf{X}$, respectively. The diagonal elements of $\Sigma_{(M \times N)}$ are the corresponding eigenvalues (singular values). \mathbf{U} and \mathbf{V} are orthogonal and Σ is diagonal. The singular values $\sigma_{m,m}$ contain the amplitude information of the data set in descending order of magnitude in the first N positions of the matrix.

Figure 15 shows the first three modes for the smaller step case. The first mode ($\mathbf{U}_{m,1}$ panel a) explains 60% of the variance to a preferential pattern ($\sigma_{1,1}^2 / \sum \sigma^2 \times 100$) and is spatially composed by two structures with the same sign covering the deep and shallow regions. In panel (b) the principal components times the single value of this mode ($\sigma_{1,1}\mathbf{V}_{n,1}^T$) shows that half of the simulations are composed by two cyclones and

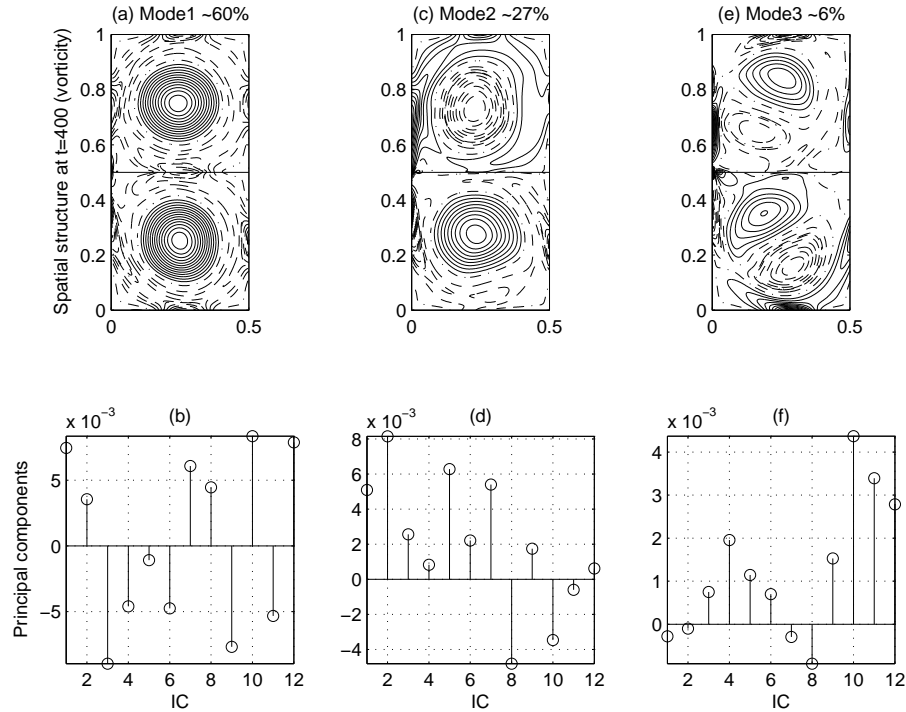


Figure 15. *Mean spatial vorticity distribution and respective principal components at $t=400$ for the very-low step EOF analysis: (a-b) first, (c-d) second and (e-f) third modes.*

the other half by two anticyclones (this product gives the sign and the amplitude of the spatial distribution). The second mode (panels c-d) explains 27% of the variance and represents a preferential distribution composed by a cyclone at the deep and an anticyclone at the shallow region. Only in three cases the inverse solution was found. The third mode (panels e-f) explains 6% of the variance and it is composed by two different signed structures at each region, with a cyclone and an anticyclone near the step at the deep and shallow regions, respectively.

Figure 16 shows the three modes of the intermediate step height case. The first mode (panels a-b) explains half of the variance (50%) and its spatial structure is composed by two different signed structures. The principal components show a cyclone (anticyclone)

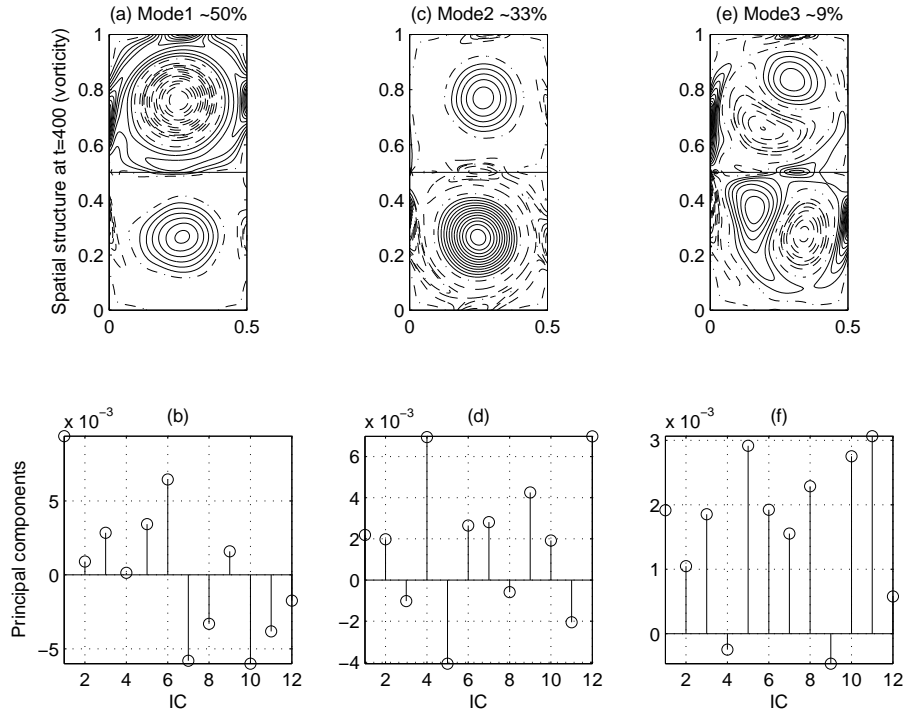


Figure 16. As Figure 15, but now for the low step case.

at the deep (shallow) region for seven simulations and the inverse distribution for the other five. The second mode (33%) shows a distribution where there is a tendency to have two positive structures at each region. The third mode, which explains 9% of the variance, shows a strong step signal with the structures slightly rotated when compared with the previous case.

For the higher step case, Figure 17 shows two structures for the first mode, with half of them being cyclones and the other half anticyclones (panels a-b). Nevertheless, a clear asymmetry between the structures is noticed. The second mode explains 38% of the variance and the solution is composed by an anticyclone at the deep region and a very weak distribution of positive vorticity at the shallow one. The third mode presents more structures near the step and only 5% of the variance is explained. In

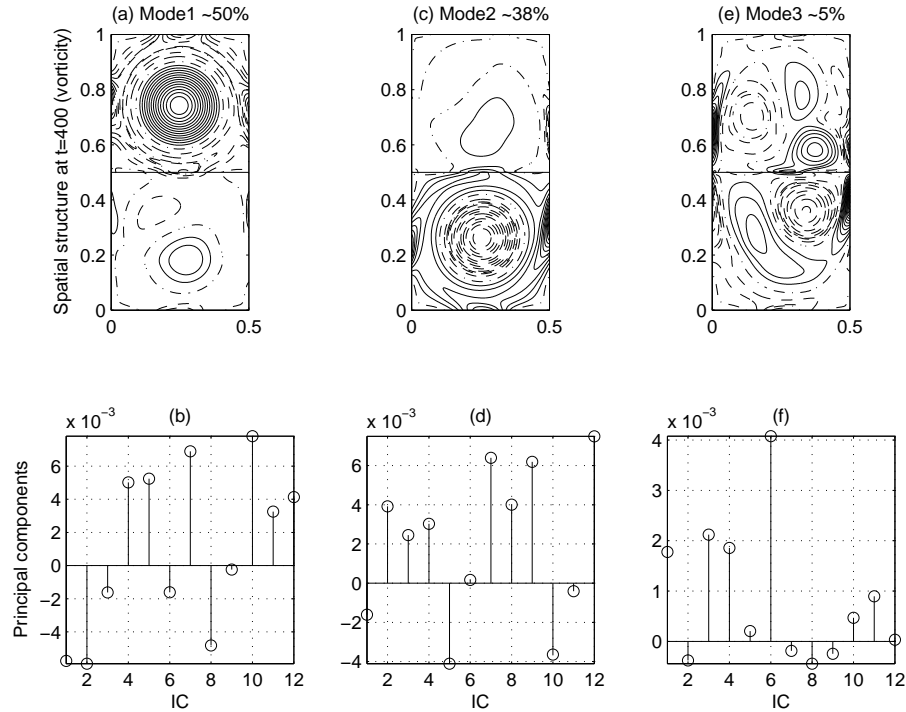


Figure 17. As Figure 15, but now for the high step case.

particular, the third mode distribution indicates a strong step signal on the separation of the domain in two independent regions.

From this analysis several features appear in order to quantify the step signal on the flow organization. The smaller step is the only case in which more than 50% of the variance (60%) is explained by the first mode, where a symmetric distribution of vorticity between regions is obtained. For the intermediate and high steps the variance explained by the first mode is 50% and the spatial structure in the shallow region is stronger and more coherent than the one in the deep side. For both intermediate and high steps, the spatial distribution of the second mode coincides with the statistical result shown in Table III. This means that this mode represents the vorticity distribution in terms of the number of vortices. Third modes explain less than 10% of the variance

in all cases but shows a possible mechanism for a step induced solution: In all cases a flow along the step with the shallow region on its right is maintained by the presence of structures near the step.

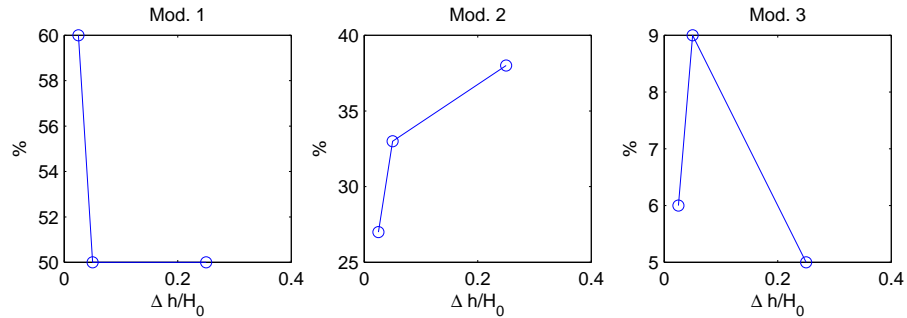


Figure 18. *Summary of the EOF analysis results for different step heights.*

Figure 18 summarizes the EOF analysis results in terms of percentage explained by each one of the first three modes and step height. It can be seen that the first two modes explain a high percentage of the variance (panels a and b). Nevertheless, the existence of a preferential solution in terms of the vorticity distribution due to step effects remains unknown. From the percentage of variance explained by the third modes, a weaker role on the existence of a preferential solution by the presence of a high step is shown (panel c). This supports the idea that there are critical, intermediate steps inducing stronger signals on the organization of the flow into a preferential solution.

III.4 Discussion and conclusions

The self-organization of confined 2D flows in rectangular containers with a step topography dividing the domain in two square regions with different depths, strongly depends on the height of the discontinuity. The conclusions are supported by laboratory exper-

periments and numerical simulations on decaying quasi-2D turbulence.

The laboratory experiments were performed in a rectangular container with aspect ratio $\delta = 2$ where a discontinuous topography divides the domain in deep and shallow regions, each with aspect ratio $\delta = 1$. The experiments showed the self-organization of an initial turbulent flow field into a well-organized flow pattern that almost fills up the entire domain. The final number of vortices tends to be $\eta = 2$, one in each region. The final distribution depends on the formation of one or two strong vortices that dominate the flow organization where the step-like topography plays a fundamental role. These strong structures are forced by the flow along the step that, when reaching the lateral boundary, interact continuously with it and injects vorticity into the flow interior. This intense step-wall-flow interaction seems to dominate the cell formation where a cyclone (anticyclone) is formed at the deep (shallow) region. Nevertheless, different distributions were also found.

Laboratory experiments are affected by the presence of Ekman damping, which eventually drains most of the energy of the system and halts the self-organization process. Thus, numerical simulations with no Ekman friction allow to study the flow behaviour for much longer times. Numerical simulations using no-slip boundary conditions show the same principal features observed in the laboratory experiments. The organization of the flow field into two structures placed near the geometrical center of each region, and a jet along the step which maintains always the shallow region on its right (for $f > 0$), are systematically obtained. The mass transfer from one side to the other across the step makes fluid columns to gain or lose relative vorticity due to potential vorticity

conservation: columns traveling from shallow to deep regions acquire positive vorticity, and traveling from deep to shallow get negative vorticity. This explains the positive (negative) vorticity patches along the deep (shallow) part for intermediate times (see panel (c) of Figure 6). As the flow decays, rotation effects and pressure gradients arising when the step is present are balanced and originate the flow along the step that always maintains the shallow region on the right. One remarkable feature of the presence of a discontinuous topography on a bounded domain is that, for intermediate times, there are always a cyclone and an anticyclone on the deep and shallow regions, respectively, near the left wall. This is due to the flow along the step

It was found that a higher step induces a faster flow organization. This is related with the existence of a critical time T^* determined by the strength of the flow and the step height, after which structures are not able to cross the topography. Afterwards, the flow evolves almost independently in each region. Such a time scale is longer for lower steps.

Nevertheless, this effect is not related with the existence of a preferential solution for long times. A slight tendency towards the existence of a preferential vorticity distribution due to the step was observed for lower steps with a cyclone (anticyclone) at the deep (shallow) region. From the EOF analysis, the existence of a preferential distribution of vorticity associated with the geometry induced by the discontinuity seems to depend on longer flow-step interactions. This supports the idea that such distribution are favored for intermediate steps, over which this interaction has a longer duration than over a high step.

Finally, it must be pointed out that despite the simplicity of the system, the difficulty to predict the long-term configuration of the flow is remarkable. Further research is in progress in order to analyze the relevance of different aspect ratios of the container, as well as different geometries.

Chapter IV

Self-organization and decaying process in a square domain with a step topography

This chapter is an early version of a manuscript to be submitted as an article to European Journal of Mechanics - B/Fluid (EJMB).

IV.1 Introduction

This chapter describes the decay process and organization of a quasi-2D turbulent flow in a square container with discontinuous topography in a rotating system. The main objective is to describe the existence of a preferential final state of the flow field in a square container due to the presence of a step-like topography. A similar study was conducted by Tenreiro *et al.* (2010) in a recent work using a step-like topography dividing a rectangular domain in two square regions (chapter III). The authors found that the presence of the step leads to a flow along the topography that always maintains the shallow region at its right for anticlockwise background rotation (see also Spitz and Nof, 1991; Stern and Austin, 1995; Zavala Sansón *et al.*, 2005; Tenreiro *et al.*, 2006). As a consequence, it was reported the existence of a critical value determined by the strength of the flow and the step height, after which both regions evolve almost independently. This separation strongly affects the flow organization. Nevertheless, it was found to be insufficient on the prediction of a long-term configuration of the flow. It was shown that the long-term evolution of the flow consisted of large-scale vortices occupying almost the entire shallow and deep regions. However, a particular

flow configuration was not found, since the sign and even the number of the vortices depend on the initial condition. In contrast, the square geometry used in this study implies the emergence of a well-defined arrangement of vortices after several rotation periods, even for very different initial conditions.

The results are obtained by means of experimental work and numerical simulations. The laboratory experiments, performed in a rotating tank, provide physical evidence of the decaying turbulence. However, the unavoidable presence of bottom friction somewhat hinders the long-term configuration of the flow, obscuring the unique arrangement of vortices at late times. By ignoring Ekman damping effects, the numerical simulations will help to gain a better understanding of the processes that lead to the existence of a final vorticity distribution induced by the step and the square geometry after long times (several rotation periods of the system).

The chapter is organized in four sections. In section II the experimental setup and results are discussed in terms of the decay process and the topographic effects on the flow organization. In section III, numerical simulations using a similar configuration are presented. The discussion of the results and conclusions appear in section IV.

IV.2 Laboratory experiments

IV.2.1 Experimental setup and procedures

The laboratory experiments were performed in an $L \times L$ square, rotating tank filled with fresh water. The horizontal aspect ratio of the tank is $\delta = 1$ with horizontal dimensions $L = 1$ m. A step-like topography was placed at the bottom of the tank dividing the domain in two rectangular regions with horizontal aspect ratio $\delta = 2$ and

horizontal dimensions $0.5 \times 1 \text{ m}^2$. The height of the water column at the deep part was $H_0 = 0.2 \text{ m}$ and two different step heights were used, $\Delta h/H_0 = 0.15$ and 0.25 (a schematic picture of the experimental setup is shown in Fig. 19). Hereafter the former will be referred to as low step, and the latter as high step.

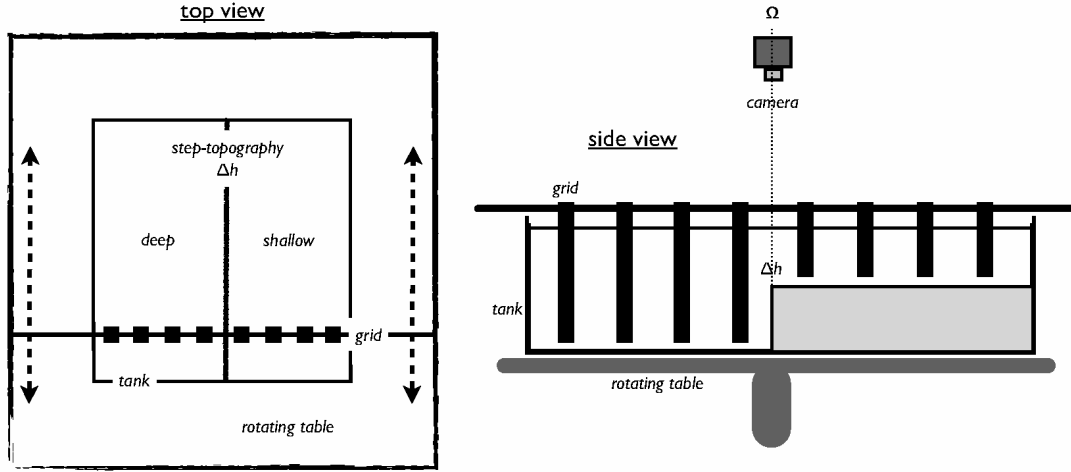


Figure 19. *Schematic top and side views of the experimental setup.*

The system rotates around the vertical axis in anticlockwise direction with a fixed rotation rate $\Omega = 0.5 \text{ rad s}^{-1}$. The flow decay is induced by both lateral and bottom friction effects, the latter implying an Ekman timescale $T_E = H_0/(\nu\Omega)^{1/2} \approx 280 \text{ s}$, for $\nu = 10^{-6} \text{ m}^2\text{s}^{-1}$ (kinematic viscosity of water at 20°C). The characteristic time scale associated with the Ekman decay is much longer than the rotation period, $T = 4\pi/f \approx 12 \text{ s}$, where $f = 2\Omega$ is the Coriolis parameter. In addition, the Ekman number $E = \frac{\nu}{fH_0^2}$ is much smaller than unity (about 2.5×10^{-5}).

Before starting an experiment, the tank is rotating at a constant angular speed for about 45 min in order to ensure a state of solid-body rotation of the fluid. Due to

this rotation, a parabolic shape of the free-surface is established (which produces a depth difference of about 0.3 cm between the center of the tank and the lateral walls). Nevertheless, the effects of the free-surface deformation on the flow evolution are ignored assuming that changes due to the step (3 and 5 cm) are more important.

An initial flow field is generated by passing a grid of vertical bars through the fluid. The grid consists of 8 PVC bars with a rectangular cross-section with a width of $b = 4$ cm and a thickness of 0.5 cm. The bars are equally distributed along a line perpendicular to the bottom topography. The separation between bars is 8 cm and all of them are adjusted to have a space of about 0.5 cm between the lowest end of the bars and the bottom of the tank. Turbulent flow is generated by moving the grid back and forth through the tank (it starts and finishes at the same position) with a constant speed $U_{grid} = 7.5$ cm/s. Once the flow has been forced, the grid is removed from the tank (a similar procedure is used in Maassen *et al.*, 2003). As a result, vortex structures with ~ 5 cm diameter are formed. The Reynolds number $Re = U_{grid}b/\nu$ based on the bar width b has a typical value $Re \approx 3000$. The initial characteristic vorticity ω_0 is around 2 s^{-1} , which corresponds to a Rossby number $Ro = \omega_0/f \sim 2$.

In laboratory experiments, 3D effects are always present due to the no-slip bottom topography. Nevertheless, a rotating system with moderate Rossby number and small Ekman number presents a strong columnar motion modulated by the depth field. This is easily verified in qualitative experiments where the vortices are visualized by adding fluorescent dye to the fluid. Quantitative experiments are performed using passive tracers ($\sim 250 \mu\text{m}$) floating on the surface. The flow field in both cases is recorded with a camera mounted at some distance above the tank co-rotating with the system. Particle image velocimetry (PIV) is used to retrieve the horizontal fields from the quantitative experiments. By repeating experiments it was found that the main results are clearly

reproducible.

IV.2.2 General features

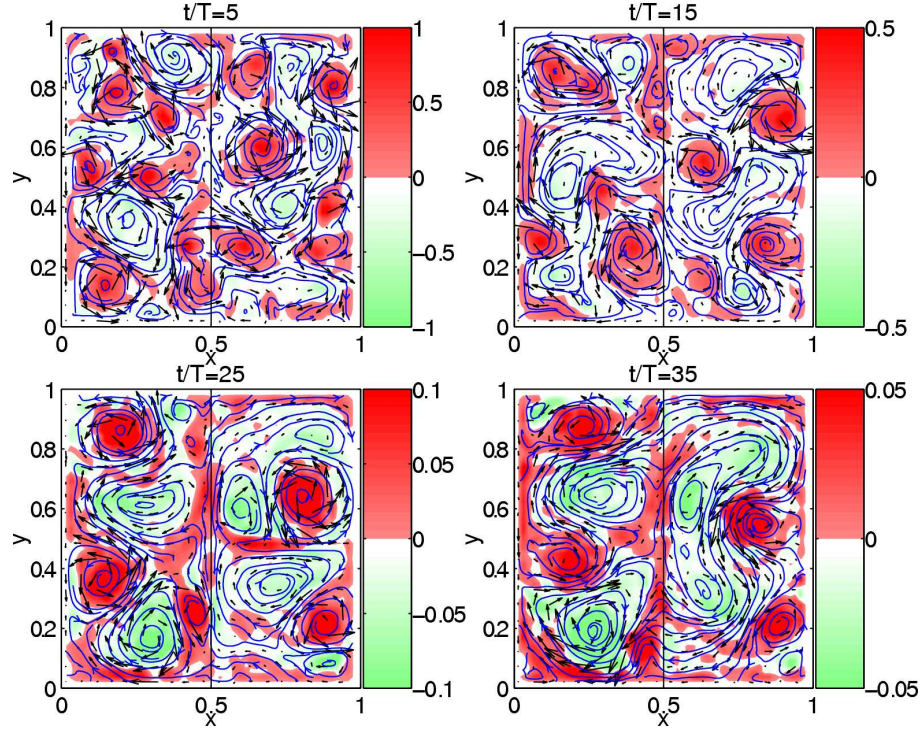


Figure 20. Vorticity surfaces, streamlines contours, and velocity arrows from an experiment with a low step ($\Delta h/H_0 = 0.15$). The black line at $x = 0.5$ indicates the step position which divides the domain in a deep (left) and a shallow (right) region. Grey surfaces represent negative values of vorticity, and dark surfaces represent positive values. The streamlines contour level increment is 0.1. The velocity arrows are scaled for a qualitative view.

Using cartesian coordinates (x, y) in the horizontal plane, the velocity components are defined as (u, v) and the vertical component of the relative vorticity is $\omega = \frac{\partial v}{\partial x} - \frac{\partial u}{\partial y}$. Figure 20 shows the evolution of the vorticity field, together with velocity arrows and streamlines for an experiment with a low step topography ($\Delta h/H_0 = 0.15$). The black line at $x = 0.5$ indicates the step position, which divides the domain in a deep (left) and shallow (right) region. In the first two panels ($t/T=5$ and 15, where T is the rotation period of the system) a very disorganized flow field can be observed. In this stage

the flow is dominated by vortex interactions, where vortices of equal sign merge and generate larger structures (inverse energy cascade), whilst different-sign vortices form self-propagating dipoles that interact with the topography and the lateral boundaries. Some of these dipolar structures are able to cross the topography from one side to the other, while others are reflected depending on their strength and size (Tenreiro *et al.*, 2006). For $t/T = 25$, a clear step signal can be identified as a flow along the topography with shallow water at its right, which is characterized by the patch of positive (negative) vorticity in the deep (shallow) region along the topography and by the orientation of the streamlines parallel to step. From this time on, the flow in the two regions evolves nearly independently: the transport across the step is reduced significantly. At $t/T = 35$ there is a distribution of four vortices with alternate signs disposed along the main axis in the deep part. In the shallow region, a strong anticyclonic circulation together with two smaller cyclones is found. This distribution is forced by the mean flow along the topography, which maintains always the shallow region at its right. When the flow approaches the vertical wall, a cyclone is formed in the deep region and an anticyclone at the shallow side. These two structures are always present in all laboratory experiments performed.

In Figure 21 a similar experiment is shown, but now for a high step topography ($\Delta h/H_0 = 0.25$). At early times ($t/T = 5$), the merging of equally-signed vortices and propagation of dipolar structures is similar to those observed in the low step experiment. Already at $t/T = 15$ a strong flow along the step is formed. This indicates an earlier separation between the deep and shallow regions with respect to the previous case. The presence of a strong flow along the topography forces the existence of two large vortices in the upper part of the domain, due to the interaction with the vertical wall. A cyclone (anticyclone) in the deep (shallow) upper region is clearly seen at $t/T = 25$. These two

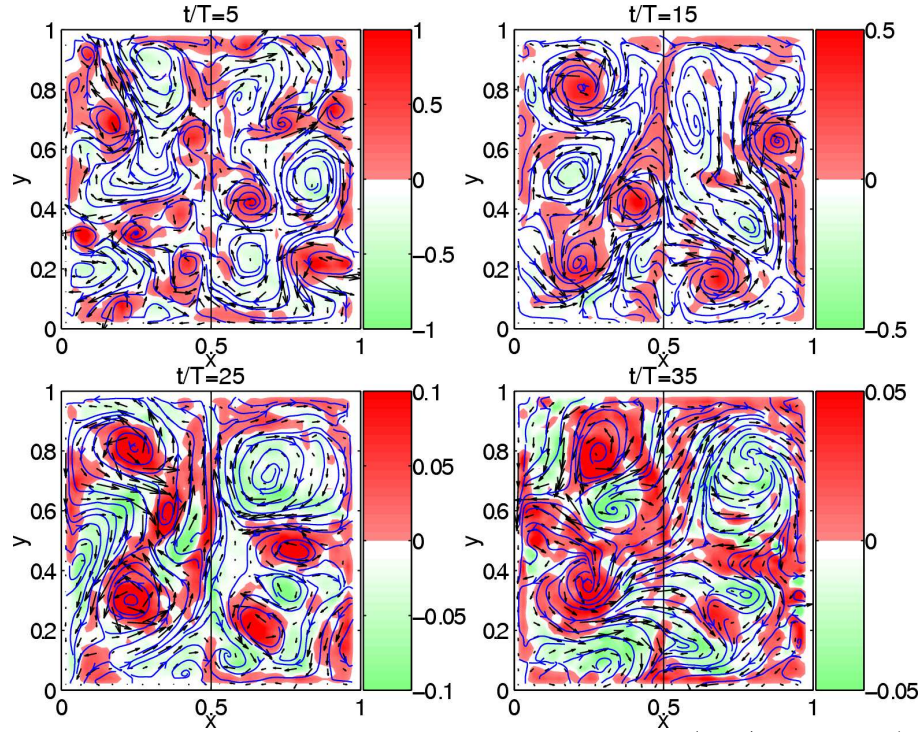


Figure 21. As Fig. 20, but now for a high step ($\Delta h/H_0 = 0.25$).

structures fill-up the entire subregion of the domain. For later times ($t/T = 35$), the high step case presents an alternated distribution of vortices at the deep region similar to the low step experiment. The shallow part is also dominated by the presence of anticyclonic motion, specially in the upper shallow region.

IV.2.3 Flow at the step

In this section the mean current along the topography is analyzed in order to quantify its influence on the flow organization due to the step presence. As stated above, after several rotation periods the step divides the domain in two nearly independent regions. The time separation strongly depends on the step height: the higher the step the faster the separation. Figure 22 shows the velocity component $v(x = 0.5)$ along the step as a function of time for the experiments shown in Figs. 20 and 21. The normalized

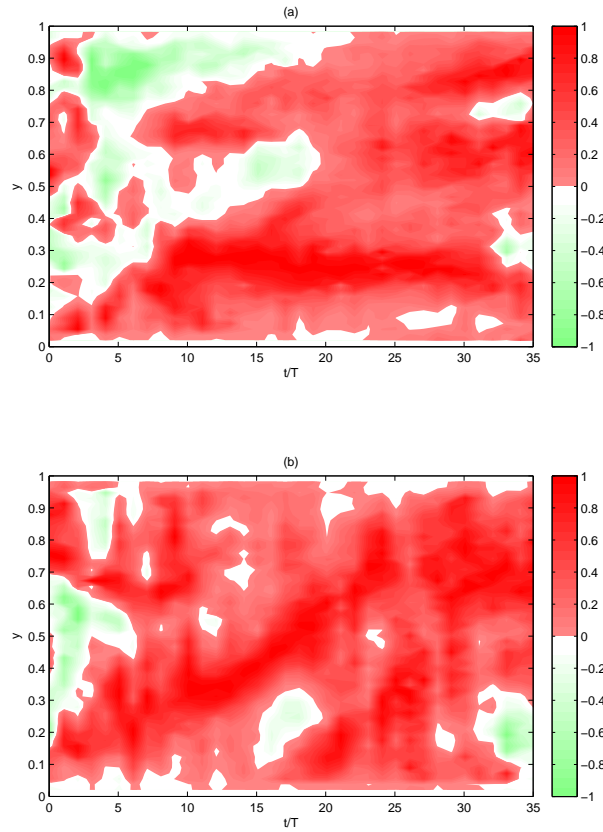


Figure 22. Normalized velocity component along the step for the experiments shown in Figs. 20 and 21. The velocity is normalized with the corresponding maximum value along the transect. The time step is $\Delta t = 1$. Grey (black) surfaces represent negative (positive) values.

velocity $\frac{v(t)}{v_{max}(t)}$ values along the step (vertical axis) are plotted for the full duration of the experiment (horizontal axis). The flow along the step is clearly shown in both panels by the measured positive values. Panel (a) shows the low step case. At early times there are regions with positive and negative values, which are associated with small scale structures crossing the topography from one side to the other. The formation of the flow along the step can be noticed at $t/T \sim 5$ by the upward slope of the positive surfaces. The flow along the low step is completely formed at $t/T \sim 20$. After this time all values are positive, indicating a flow along the step with the shallow region at its right. Panel (b) shows the high step case, where the flow along the step is

already present at $t/T \sim 5$. Negative values at the lower part of the step ($y \sim 0.2$) for longer times (for instance, at $t/T \sim 15$ or $t/T \sim 33$) are directly associated with an anticyclonic structure present at this particular region.

IV.2.4 Results based on ensemble averages

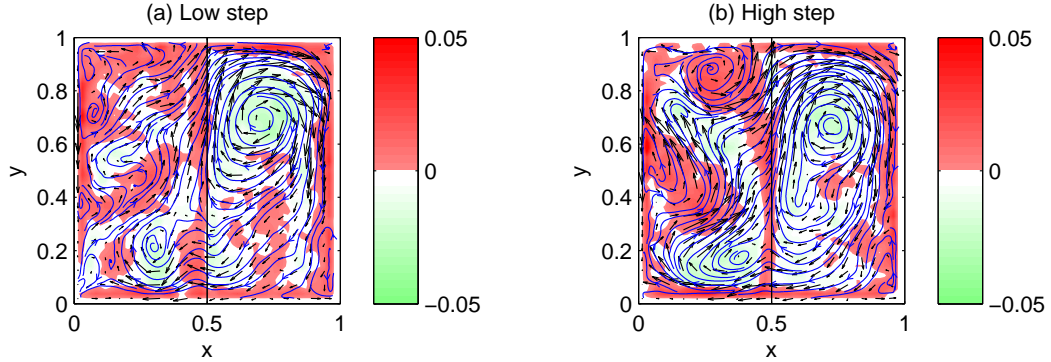


Figure 23. Mean spatial distribution of vorticity, streamlines contours, and velocity arrows at $t/T = 35$ from an ensemble of (a) 14 experiments for the low step and (b) 18 experiments for the high step. Grey (black) surfaces represent negative (positive) values of vorticity. The contour level increment for the streamlines is 0.1. The velocity arrows are scaled for a qualitative view.

In order to quantify the step-signal on the flow organization, an ensemble average based on 32 experiments is performed (14 for the low step and 18 for the high step case). The differences between experiments are associated with small perturbations on the initial conditions as the grid passes along the domain: even though the same grid is used, moving with the same velocity in all cases, there are always unavoidable differences between initial conditions. Although the detailed flow evolution differs between individual experiments, some robust features, such as the flow along the step, were observed in all cases.

In Figure 23 the mean spatial flow field is shown at $t/T = 35$ for the low (panel a) and high (panel b) step. The step signal is easily noticed by the positive (negative)

vorticity values aligned along the step in the deep (shallow) region. These are directly associated with the structure of the mean flow along the topography with shallow water at its right. When this flow interacts with the upper wall, it gives rise to a positive (negative) relative vorticity patch at the deep (shallow) region, as described for individual cases in Figs. 20 and 21. In general, the final configuration is an irregular pattern of four vortex-like structures in the deep region, alternately disposed, and a large patch of negative vorticity at the shallow side. In fact, the anticyclonic vortex formed next to the upper wall in the shallow part is a rather robust and persistent feature. The streamlines and velocity vectors are also shown, and corroborate these arrangements.

The distribution of four vortices in the deep region is geometrically associated with its rectangular area with aspect ratio $\delta = 2$. Indeed, it has been shown in previous studies (e.g. Maassen *et al.*, 2003) the formation of a certain number of vortices according with the aspect ratio of the domain. Since the regions tend to evolve almost independently after some time, it is expected to observe such a distribution. At these times, however, the flow has decayed due to Ekman damping effects, always present in laboratory experiments. This decay seems to prevent the formation of the same pattern at the shallow side, where bottom friction has a relatively large effect. A different final distribution of vortices induced by the step topography will be discussed later, in numerical simulations with the Ekman damping effects being set to zero.

In Figure 24 the time evolution of the mean normalized velocity component along the step, defined as

$$V_s = \frac{1}{v_{max}L} \int_0^L v dy, \quad (69)$$

is plotted for each experiment. For the low step case [panel (a)] strong variations of V_s values can be noticed for $t/T \sim 0 - 15$. After $t/T \sim 15$ all experiments reveal a

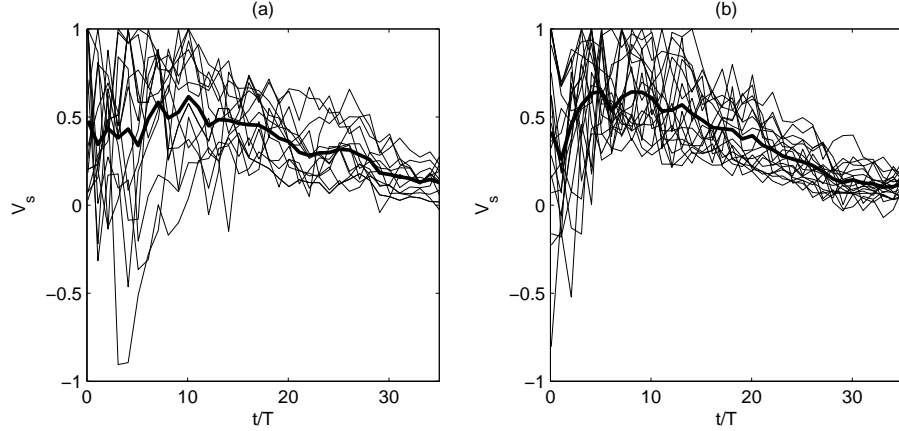


Figure 24. *Time evolution of the normalized velocity component along the step (V_s , equation 69) for (a) low and (b) high steps, calculated in 14 experiments for the low step and 18 experiments for the high step. The thick, black line indicates the ensemble average.*

positive value of V_s , and lower amplitudes of oscillation, which is directly associated with the flow along the step. In panel (b) for the high step, there is a strong tendency towards positive mean values of V_s just after $t/T \sim 5$. The high step forces an earlier separation of the domain in two subregions and the oscillation is smaller. Therefore, the mean flow along the step is clearly identified in the ensemble of experiments.

Taking advantage of the relatively large number of experiments, some global quantities of the ensemble are calculated, which are the total kinetic energy and the enstrophy:

$$E = \frac{1}{2} \int (u^2 + v^2) dx dy, \quad (70)$$

$$Z = \frac{1}{2} \int \omega^2 dx dy. \quad (71)$$

A third integral property is simply the ratio Z/E , which can be identified as a squared wavenumber or, equivalently, as the inverse of the squared characteristic length l of the flow:

$$\frac{1}{l^2} = \frac{Z}{E}. \quad (72)$$

In Figure 25, panel (a) shows the time evolution of the averaged kinetic energy

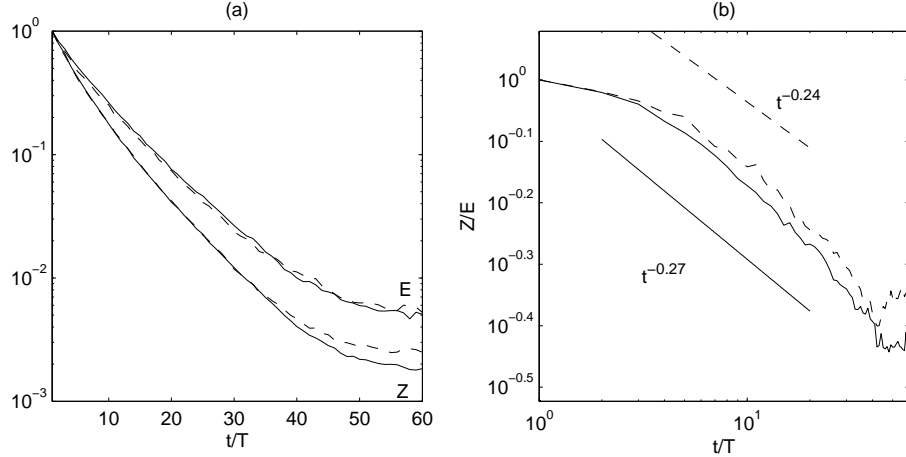


Figure 25. Time evolution of (a) normalized kinetic energy (E) and enstrophy (Z) and (b) ratio Z/E , from an ensemble of 14 experiments for the low step (solid lines) and 18 experiments for the high step (dashed lines).

and the averaged enstrophy for the two step heights. A very similar decay in both quantities is observed until $t/T \sim 35$. After this time the inverse energy cascade is halted by viscous effects that start to dominate the decay process. In addition, velocity measurements are less accurate for very low motions. As a result, the energy and enstrophy reach a stable value, perhaps also due to a weak influence of wind-induced motions at the free-surface, and to small errors of the experimental measurements. Thus, the experimental results are useful up to 35 to 40 rotation periods. Panel (b) shows Z/E in a log-log plot, where it is observed that both present a power-law decay. The exponent of $t^{-\alpha}$ indicates the efficiency of the inverse energy cascade, *i.e.* the efficiency of the organization of the flow in larger structures. A slightly larger value is found for the low step case with $\alpha = 0.27$, whilst for the high step $\alpha = 0.24$ for a decay period between $t/T = 2 - 20$ (the error associated with the exponent calculation is $\sim 10^{-2}$).

In order to quantify the efficiency of the flow organization in the shallow and deep parts and its relation with the step height, the ratios Z/E are plotted for each region

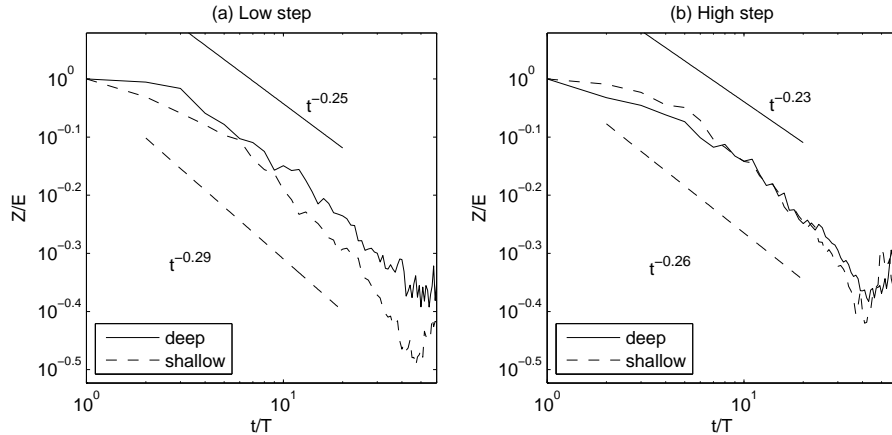


Figure 26. *Time evolution of the ratio Z/E in the shallow (dashed) and deep (solid) regions for the (a) low step and (b) high step. The ensemble is based on 14 experiments using the low step and on 18 experiments using the high step.*

separately in Figure 26. Panel (a) shows the ratios for a low step where a more effective organization is obtained for the shallow part, $\alpha = 0.29$, whilst for the deep part $\alpha = 0.25$. For the high step case [panel (b)] in the shallow part $\alpha = 0.26$ and in the deep $\alpha = 0.23$. Comparing both step cases and respective regions, it is found that globally the inverse energy cascade is slightly more effective when a low step is present due to a stronger organization in both regions. Recall that in both cases an anticyclonic circulation dominates over the shallow part of the domain, whilst more structures are observed in the deep region. When the step height increases, both regions tend to have the same exponents since the step acts like a wall, effectively dividing the flow domain into two separate regions.

IV.3 Numerical simulations

In this section, numerical simulations of decaying quasi-2D turbulence with discontinuous topography are presented. A barotropic, shallow-water model in the $\omega - \psi$ formulation with Ekman friction is solved with a finite differences scheme (see Zavala

Sansón and van Heijst, 2002). The equations for the relative vorticity ω are

$$\frac{\partial \omega}{\partial t} + J(q, \psi) - \frac{\delta_E}{2h} \nabla \psi \cdot \nabla q = \nu \nabla^2 \omega - \frac{\delta_E}{2h} \omega(\omega + f), \quad (73)$$

$$\omega = -\frac{1}{h} \nabla^2 \psi + \frac{1}{h^2} \nabla h \cdot \nabla \psi + \frac{\delta_E}{2h} \frac{2}{h^2} J(h, \psi). \quad (74)$$

where $q = (\omega + f)/h$ is the potential vorticity, with $h(x, y)$ the fluid depth (which is time independent, according with the rigid-lid approximation), ψ is a transport function, $\delta_E = (2\nu/f)^{1/2}$ is the thickness of the bottom Ekman layer and J the Jacobian operator. The model includes linear and nonlinear Ekman friction terms (proportional to δ_E), which provide a good representation of bottom friction effects (Zavala Sansón and van Heijst, 2002).

The numerical domain is analogous to the experimental tank, as well as the flow parameters. The domain represents an $L \times L$ square tank, with $L = 1$. The topography consists of a discontinuity (step-like topography) dividing the domain in two equal rectangular regions (the discontinuity is actually a very narrow, step slope due to the spatial discretization). Corresponding with the experiments, in all simulations the water column in the deep part of the domain is $H_0 = 0.2$. Two step heights are used, $\frac{\Delta h}{H_0} = 0.15$ (low step) and $\frac{\Delta h}{H_0} = 0.25$ (high step). The rotation period around the vertical axis is $T = 4\pi/f$, with $f = 1$ being the Coriolis parameter. The flow decay is induced by frictional effects, where the kinematic viscosity is $\nu = 10^{-6}$. No-slip boundary conditions are imposed at the boundaries in order to represent the lateral tank walls. The spatial discretization consists of 257×257 grid points and the time step used is fixed at $\Delta t = 10^{-3}$.

IV.3.1 Comparison with the laboratory experiments

In order to compare the quasi-2D simulations with the laboratory results, it is convenient to use the experimental flow fields as the initial conditions. Therefore, the vorticity field is taken from the first few seconds of some experiments $t/T = 1$, interpolated onto a 257×257 numerical grid, and considered as the initial vorticity distribution in the simulations.

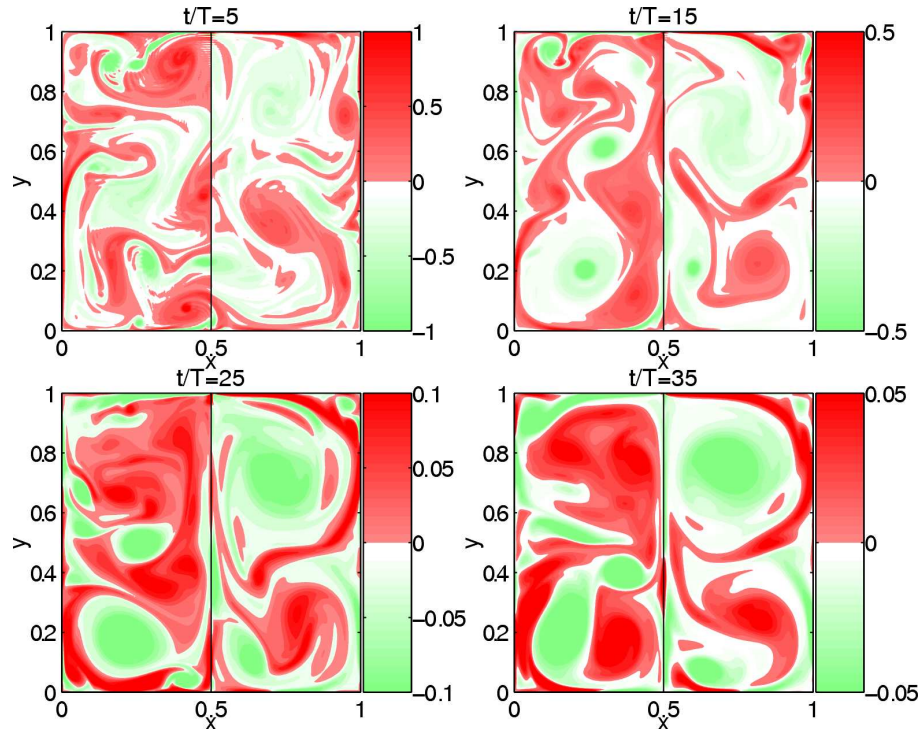


Figure 27. Vorticity surfaces from a simulation with a high step and no-slip boundary conditions. Grey (dark) surfaces represent negative (positive) values of vorticity. The black line at $x = 0.5$ indicates the step position which divides the domain in a deep (left) and a shallow (right) region.

Figure 27 shows the evolution of the relative vorticity surfaces for a high step in a typical simulation using lateral no-slip boundary conditions and bottom friction. The black line at $x = 0.5$ indicates the position of the step, which divides the domain in a deep (left) and a shallow (right) region (as in the laboratory experiments). In the first two panels ($t/T = 5 - 15$) several features can be noticed: strong vortex-

vortex interactions with like-sign vortices merging and forming larger structures, and opposite-sign vortices forming dipolar structures; vortex-lateral walls interactions that lead to the formation of thin filaments that are injected into the flow interior; and vortex-topography interactions. For $t/T = 5$ there are some structures above the step. However, for $t/T = 15$ there are only a few of them crossing the step from one side to the other. At this stage a step-signal is clearly seen by the aligned positive (negative) vorticity along the step at the deep (shallow) region. For $t/T = 25$ the existence of a cyclone (anticyclone) in the deep (shallow) upper region of the domain is observed. The flow along the step and its consequent interaction with the vertical wall force these distributions. In the lower part of the domain the process tends to be the inverse: an anticyclone (cyclone) is formed in the deep (shallow) region.

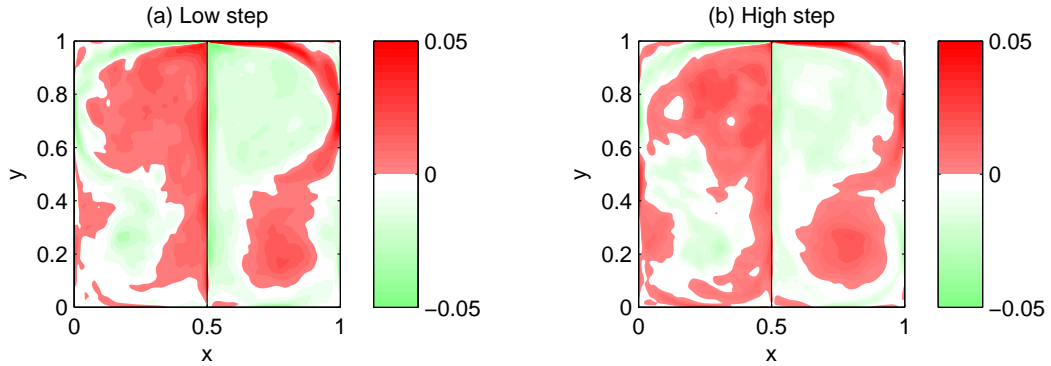


Figure 28. *Mean spatial vorticity distribution at $t/T = 20$ for (a) low step and (b) high step. Color surfaces as in Fig. 27. The ensemble is based on 27 simulations with slightly different initial conditions for each step height.*

The processes just described are qualitatively similar to those observed in the experiments. In particular, the mean flow along the step and the generation of counter-rotating vortices next to the upper wall are clearly reproduced. Moreover, the vorticity distributions for late times are also similar. In order to reinforce this notion, Figure 28 shows the mean spatial distribution of vorticity from an ensemble of 27 simulations with different initial conditions at $t/T = 35$. A qualitative agreement can be made

with Figure 23, in which the main features are present and the final distribution of the vortices is observed to be similar.

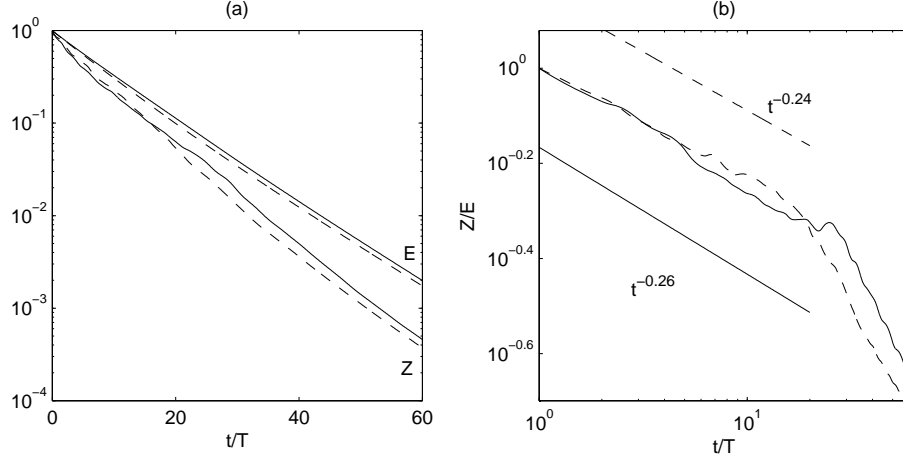


Figure 29. Time evolution of (a) normalized kinetic energy (E) and enstrophy (Z) and (b) ratio Z/E from an ensemble of 27 simulations for each step height.

In Figures 29 and 30, the decay of E , Z and the ratio Z/E are analyzed for these two ensembles of simulations where a quantitative comparison with Figures 25 and 26 can be made. The efficiency of the inverse energy cascade depends on the step height: a global decay with $\alpha = 0.26$ is obtained for the low step case, whilst $\alpha = 0.24$ for the high step between $t/T = 1 - 20$. When calculated in each region separately, for the low step case, $\alpha = 0.29$ in the shallow part and $\alpha = 0.23$ in the deep part. For the high step case $\alpha = 0.24$ in the deep and in the shallow region, revealing the effective separation of the flow in two almost independent regions.

IV.3.2 Results without bottom friction

In this section we examine the existence of a preferred distribution of vorticity induced by the step, *i.e.* a geometrical arrangement of the vortices at late times due to the step topography. Such a final configuration consists of four vortices covering the whole domain, two at each region: at the deep side a dipolar structure trying to climb the

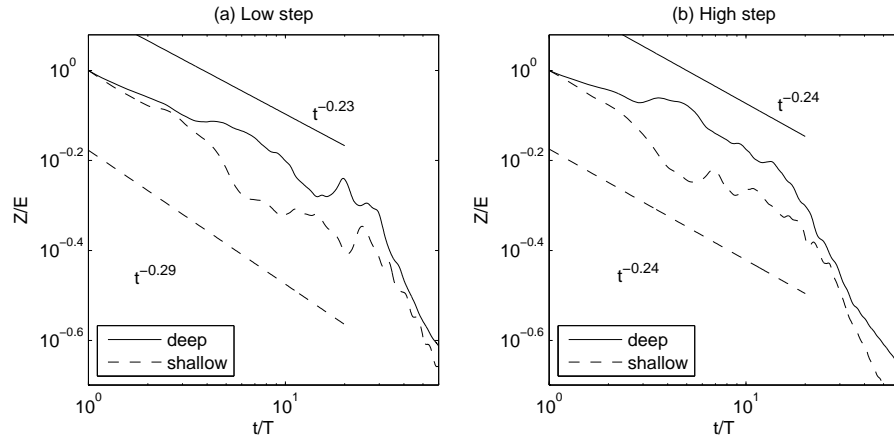


Figure 30. Time evolution of the normalized ratio (Z/E) for (a) low step and (b) high step from an ensemble of 27 simulations for each step height.

step and the inverse distribution at the shallow side of the step. This arrangement is suggested by the experimental and numerical results presented previously, specially regarding the cyclone-anticyclone pair next to the upper wall. However, bottom friction effects drain the kinetic energy of the flow before reaching this final state. As a consequence, the four-vortices final distribution is inhibited in the laboratory experiments. In order to avoid this, the Ekman terms in equations (73) and (74) are dropped and an ensemble of new simulations is carried out.

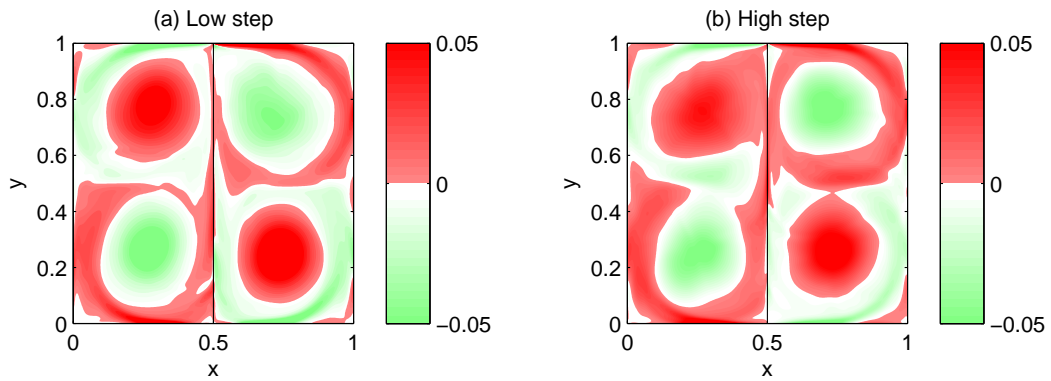


Figure 31. Mean spatial vorticity distribution at $t/T = 200$ for (a) low step and (b) high step simulations without bottom friction. Grey (dark) surfaces represent negative (positive) values of vorticity. The black line at $x = 0.5$ indicates the step position. The data are computed from an ensemble of 10 simulations for each step height.

A set of ten initial conditions similar to the ones used in section IV.3.1 were used for the two step height cases, now for the case of zero bottom friction. Now, the duration of the simulations can be longer due to the absence of Ekman damping. The mean spatial vorticity distribution of the ensemble at $t/T = 200$ is shown in Figure 31. Clearly, a well defined final distribution of four vortices is observed in both cases. This unique distribution of the vortices is forced by the interaction of the flow along the step with the upper wall, which results in a big dipolar structure at the upper side of the step. By geometry and due to the no-slip boundary conditions, this persistent dipolar structure forces the inverse distribution at the lower side of the step. The final distribution of the vortices are two large dipolar structures, one trying to climb the step and the other one trying to go down the step. All vortices are surrounded by a shield of opposite vorticity, indicating the boundary layer at the lateral walls of the flow domain.

In order to quantify the robustness of this step-induced vorticity distribution, a proper orthogonal decomposition (POD) technique is used (Berkooz *et al.*, 1993). The POD analysis searches for structures that explain the maximum amount of changes in a 2D matrix. First, a space-realization array at a single time ($t/T = 200$) is used and the analysis seeks the maximum amount of changes or variations relative to the mean spatial distribution of vorticity of the ensemble (see Tenreiro *et al.*, 2010). Second, the evolution in time of the amount of changes relative to the mean spatial distribution is investigated.

In Figure 32 the first three modes for the low step are shown for $t/T = 200$. Panel (a) presents the first mode, which explains 72% of the variations relative to the mean spatial distribution of vorticity. In panel (b), the principal components relative to this mode show that all simulations have the vortices at the same regions, since all principal components have the same sign. A simulation with a negative value would indicate a

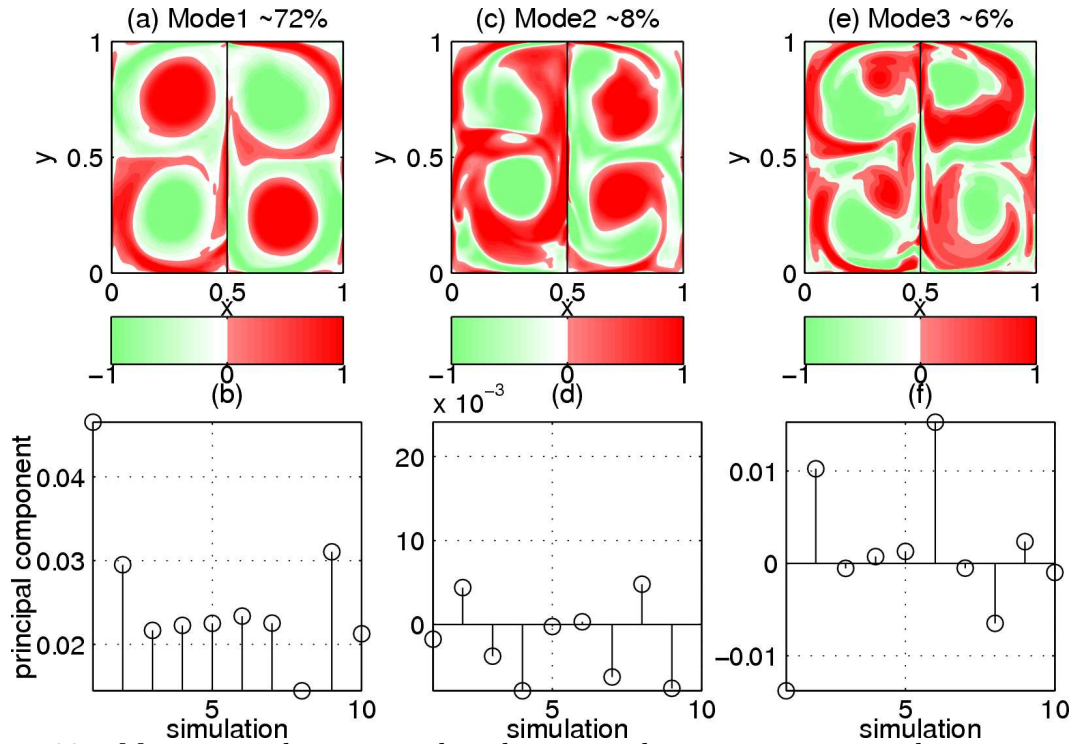


Figure 32. Mean spatial vorticity distribution and respective principal components at $t/T = 200$ for the low step case POD analysis: (a)-(b) first, (c)-(d) second, and (e)-(f) third modes.

similar vorticity distribution as the mean, but now with opposite sign. Mode two represents much less variations (8%), which are associated with small oscillations of the final structures. In the third mode [panels (e) and (f)], as expected, the explained variations are even lower (6%); nevertheless, the step signal is noticed by the spatial distribution of vorticity along the topography. For the high step case the spatial distribution for each mode are very similar (not shown here), however the variations explained for each mode are different: 61% by the first, 15% by the second and 7% by the third.

In order to investigate the evolution in time of the amount of explained variations, the first three modes are calculated for each complete rotation of the system. The results are shown together for the low and high steps in Figure 33. In panel (a) the amount of explained variations by the first mode is shown. For the interval $t/T = 0 - 40$ both step

heights present similar amount of explained changes. However, after this period the low step case presents always a larger percentage of explained changes relative to the high step. The amount of explained changes in the second and third modes decay as expected. These two modes represent small scale oscillations due to vortex interactions with the lateral boundaries and the topography.

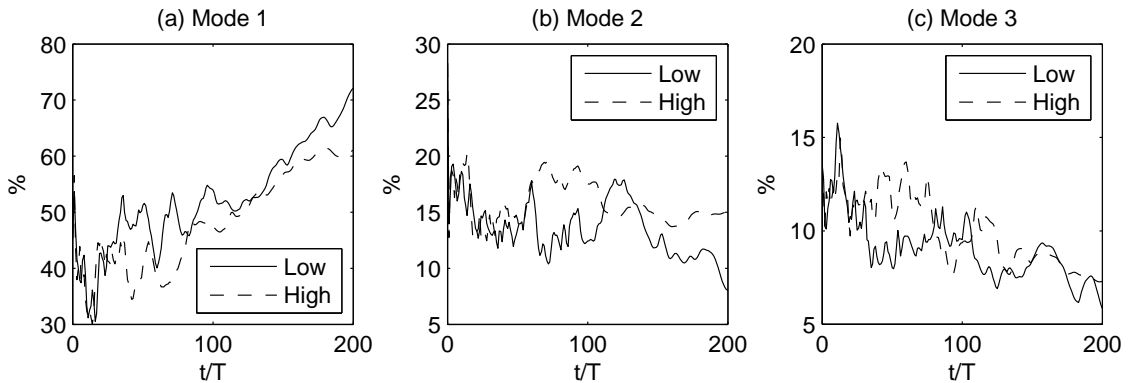


Figure 33. Time evolution of explained changes relative to the mean spatial distribution of vorticity by the (a) first, (b) second, and (c) third modes. Continuous line for the low step and dashed lines for the high step.

IV.3.3 Different initial conditions

In order to show that the step-induced final distribution of the vortices is independent of the initial flow, five simulations using different initial conditions (IC1 to IC5) for a high step ($\Delta H/H_0 = 0.25$) were performed. Again bottom friction is not considered. In Figure 34 the vorticity surfaces are plotted for $t/T = 0$ and $t/T = 200$ for each simulation. IC1 is a 16×16 array of cyclonic and anticyclonic Gaussian vortices with maximum vorticity $|\omega| = 1$ and diameter $a = 0.05$. This type of initial condition is similar to those obtained in laboratory experiments with electromagnetically forced vortices (see Tabeling *et al.*, 1991). The IC2 (IC3) represents a dipolar structure oriented towards the shallow (deep) side of the step topography. The diameter of the vortices is $a = 0.1$

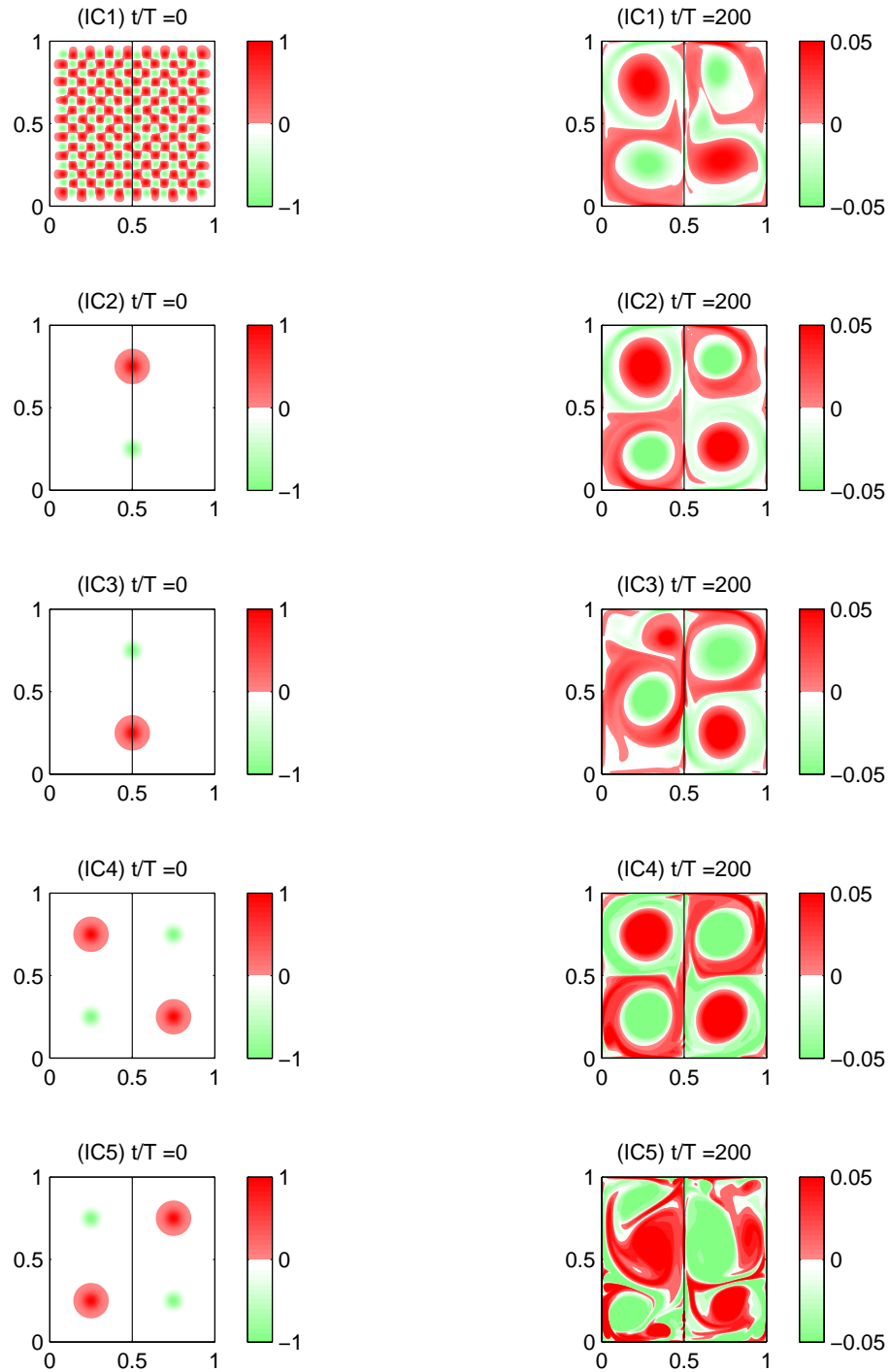


Figure 34. *Vorticity surfaces at $t/T = 0$ and $t/T = 200$ from five simulations without bottom friction using different initial conditions.*

and they are initially separated a distance $L/2$. Their peak vorticity is $|\omega| = 1$. IC4 consists of four vortices disposed as the expected final distribution described previously:

the vortices are located at $(x, y) = (0.25, 0.25), (0.25, 0.75), (0.75, 0.25),$ and $(0.75, 0.75)$. Their size and strength are the same as in IC2 and IC3. IC5 is the inverse distribution.

As can be seen from the right panels, all five different initial conditions result in a similar final distribution of vortices. There are some differences, specially when using IC5, but in general there is a clear trend towards the expected configuration. Several other initial conditions have been used (not shown), generally resulting in the same final four-vortex configuration.

IV.4 Discussion and conclusions

The self-organization of confined 2D turbulent flows in a square tank/geometry with a step-like topography in a rotating system has been investigated by means of laboratory experiments and numerical simulations. The goal was to describe the flow evolution in the shallow and deep regions and to discuss the existence of a preferential final state of the flow induced by the topography.

The laboratory experiments were performed in a rotating square tank with horizontal aspect ratio $\delta = 1$. A step topography was used to divide the domain in two rectangular regions with aspect ratio $\delta = 2$ and with different depths, one shallow and the other deep. In the laboratory experiments, the evolution from an initial turbulent flow field into a well-organized flow pattern was found. A persistent flow along the topography with the shallow region at its right is observed in all cases. This flow divides the domain in two independent regions. The time required for the separation to be effective strongly depends on the step height. The flow along the topography plays a fundamental role on the flow organization by its continuous interaction with the corresponding vertical wall perpendicular to the step. From this interaction two strong

structures at the end of the step are formed: cyclonic in the deep and anticyclonic in the shallow region. The presence of these two structures implies a continuous injection of vorticity into the flow interior. For longer times, the experimental ensemble shows four alternate-sign structures in the deep region, while the shallow part is dominated by an anticyclonic circulation.

Numerical simulations using no-slip boundary conditions show the same principal features observed in the laboratory experiments: a jet along the step with the shallow region at its right; different separation times due to different step heights; two persistent structures at the end of the step near the vertical wall continuously forcing the existence of a preferential distribution of the vortices; and a similar final distribution of the vortices for longer times.

Due to Ekman damping effects, the inverse energy cascade in the laboratory experiments and in the numerical simulations with bottom friction is halted at a finite time. As a result, some middle-size structures are still observed at long times, specially in the deep region. In order to study the full self-organization process, numerical simulations with zero Ekman friction were performed as well. For shorter times, the zero Ekman friction simulations show the same principal features as the ones with non-zero bottom friction. For longer times, in addition, it was possible to reach a complete self-organization of the flow and it was found to be a unique pattern. Such a configuration consists of a well-defined, long-term distribution of four vortices alternately disposed: in the deep part, a cyclone-anticyclone pair that fills-up the entire region, and the mirror structures at the shallow side (see Fig. 31). All four structures are surrounded by a ring of opposite-sign vorticity, indicating the presence of boundary layers along the lateral walls. Looking along the step, the cyclones are disposed at the up-left and down-right corners and the anticyclones at the opposite regions (up-right and down-left corners).

This vortex distribution was found to be unique and independent of the initial condition. This was shown by performing several simulations with different initial configurations and verifying that the four-vortex configuration was obtained at long-times.

It is important to remark that despite the apparent symmetry of this distribution, the cyclonic vortices cannot occupy the positions of the anticyclones. In other words, the mirror configuration with cyclones instead of anticyclones and vice versa, is not possible. The reason is that the step breaks such a symmetry and therefore it determines the position of the vortices. Indeed, where the flow along the step collides with the upper wall it induces the formation of a cyclone in the deep part and an anticyclone in the shallow region, as observed in the experiments. Since this interaction is continuously occurring, it forces the formation of the other structures and, eventually, of the four-vortex configuration. The POD analysis confirms the persistence of a preferential distribution of the vortices due to the geometry induced by the discontinuity.

The jet along the topography plays a fundamental role on the organization of the flow. Due to its continuous interaction with the vertical walls, the vorticity that is injected into the flow interior forces the existence of a preferential distribution of the vortices. This depends on the relation between the length of the discontinuity and the length of the lateral walls. A similar mechanism is found in the southern region of the Gulf of California. During the summer period, the surface circulation is characterized by an eddy-train of counter-rotating mesoscale eddies placed along the main axis of the Gulf (see Zamudio *et al.*, 2008). The organization and positioning of these structures are associated with the intense Pacific eastern boundary current, which interacts with the topographic features (bottom and coastal) forcing a unique distribution of the structures. This eastern boundary current could be numerically and experimentally simulated by the flow along a step-like topography.

For purely 2D flows in bounded domains, the evolution towards large structures filling the container is well-known, as shown for square and rectangular boundaries (Clerc *et al.*, 1999; Maassen *et al.*, 2003; van de Konijnenberg and van Heijst, 1996). The preferential vorticity distribution in a square container divided by a step topography, however, is a remarkable feature. Indeed, when the geometry of the container is different, a well-defined long-term configuration might not be obtained. That is the case of a rectangular domain with aspect ratio 2, as shown by Tenreiro *et al.* (2010). These results open new questions on the predictability of the flow evolution for different domain geometries with larger aspect ratios and step orientations. They seem to depend only on the length of the step when compared with the length of the walls. Further research is in progress in order to support this possible dependence.

On the other hand, the influence of the step height was considered. It was found that a higher step induces a faster flow organization at early times due to stronger topography effects. Nevertheless, smaller steps are more efficient due to longer interactions. The flow evolution in rectangular geometries favour the organization of counter-rotating vortices (eddy-train) that is found to be unique when a flow along the boundary is present.

Chapter V

The Gulf of California

V.1 Introduction

The surface circulation in the Gulf of California (GC) has been widely studied during the last decades. In the northern part, a seasonally-reversing gyre has been observed, cyclonic in summer and anticyclonic in winter (Lavín *et al.*, 1997). On the other hand, the southern part presents a more complicated circulation. A characteristic feature of the southern part of the Gulf of California is the formation of an eddy train along the main axis during the summer period. This has been observed in satellite images and corroborated by direct hydrographic observations (Castro *et al.*, 2007). Lavín *et al.* (2007) reported poleward surface currents flowing along the eastern coast during the early summer; when this coastal flow gets weaker the eddies become more evident and dominate the circulation in all the southern part. The eddies in this region are strongly barotropic, reaching up to 1000 m depth. Makarov and Jiménez-Illescas (2003) calculated barotropic currents for the southern part of the Gulf of California and their results suggest that large planetary and topographical effects support the main circulation in this region.

In this chapter, two numerical models were used to simulate the seasonal circulation of the Gulf of California, in particular the summer eddy train organization and its relation with topographic effects. The main goal was to understand the organization of the vortices along the main axis of the Gulf of California due to geometrical properties

given by different topographic features. First, the SWEVOL model used in previous chapters is adapted as a long rectangular box that resembles the Gulf of California (section V.2). Secondly, the regional model ROMS is used for simulating the entire Gulf under more realistic conditions (section V.3).

V.2 An idealized Gulf of California

It was seen in chapters III and IV that a step-like topography plays a fundamental role on the self-organization process of a turbulent flow inside rectangular and square domains. Both cases were numerically solved by using a finite differences code, which will be used here again. In this section, the numerical domain represents an $L_x \times L_y$ rectangular basin with dimensions comparable with the southern part of the Gulf of California ($200 \times 1000 \text{ km}^2$). The rotation period around the vertical axis is $T = 4\pi/f$, with $f = 10^{-4} \text{ s}^{-1}$ the Coriolis parameter. The flow decay is induced by frictional effects, where the turbulent eddy viscosity coefficient is $\nu = 10^2 \text{ m}^2/\text{s}$. No-slip boundary conditions are imposed in order to represent the lateral walls and bottom-friction is set to zero in order to observe the full organization process. The spatial discretization consists of 129×129 grid points and the time step used is fixed at $\Delta t = 720 \text{ s}$. The initial condition in all cases consists of a cyclonic circulation around the central point of the domain, with $\omega_{max} = f/4$. This initial state resembles the large-scale circulation set by the summer currents along the eastern coast of the Gulf of California. The simulations have a duration of 60 rotation periods, which is a timescale comparable to the period in which the train of mesoscale vortices is formed along the Gulf.

When studying the decaying process of quasi-2D turbulent flows in rectangular and square closed domains with a step-topography, a strong dependence was found between

the final configurations of the self-organization process and the aspect ratios (δ) of the domains. The self-organization process results in a well-defined final distribution of the vortices, modulated by the step topography in both cases. For $\delta = 1$ (square case) a unique final distribution of the vortices was found. Nevertheless, for $\delta = 2$ (rectangular case) a strong dependence on the initial condition was observed, which implies the existence of several different final distributions. These important results suggested a strong correlation between the aspect ratio of the domain and the existence of a preferential distribution of the vortices.

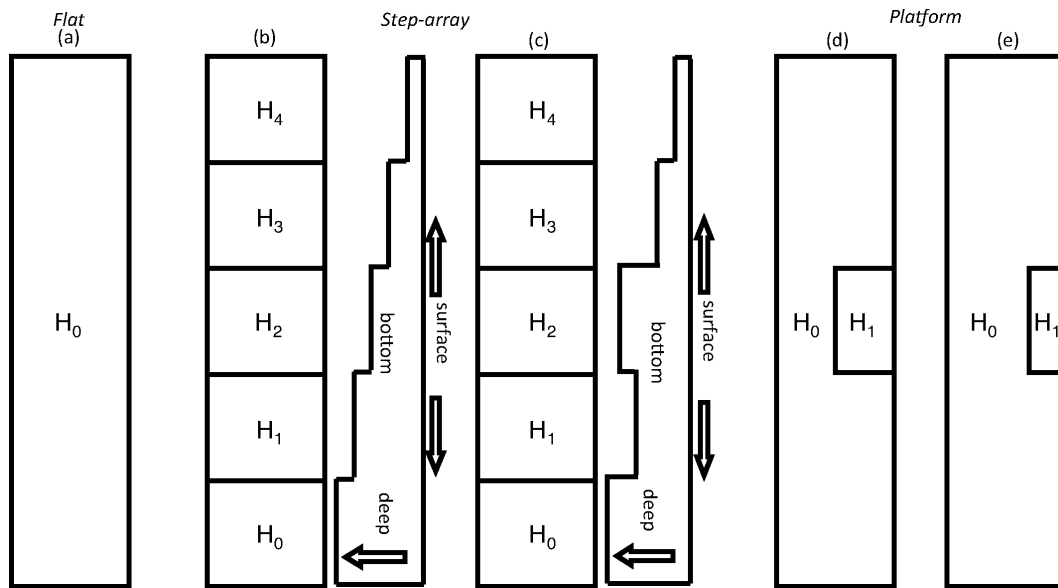


Figure 35. *Schematic representation of the five topographies used: (a) flat-bottom topography; (b) and (c) step-array topographies; (d) and (e) platform topographies. The depth values $H_{0,1,2,3,4}$ are summarized in table IV.*

Using a long rectangular box ($\delta = 5$), now the effects of five different topographies are analyzed. As a reference case, the flat bottom topography is first examined. The rest of the topographies consist of different arrangements of steps along the rectangular box. Analogously to the real bottom topography in the gulf, the depth of the steps increases along the long side of the rectangular domain. A detailed description of each case is schematically shown in Figure 35.

The numerical parameters and topographies used in the experiments of this section are summarized in table IV.

Table IV. *Characteristic parameters and topographies of the numerical simulations.*

Domain (aspect ratio) $L_x \times L_y$ (δ)		$200 \times 1000 \text{ km}^2$ (5)
Kinematic viscosity ν		$10^2 \text{ m}^2\text{s}^{-1}$
Coriolis parameter f		10^{-4} s^{-1}
Rotation period	$T = 4\pi/f$	
Initial peak vorticity ω_{max}		$f/4$
Time step Δt		720 s
Topographies	Regions	Depths (10^3 m)
(a) flat	H_0	1.0
(b) step-array	$H_0H_1H_2H_3H_4$	2.5 1.5 1.0 0.5 0.25
(c) step-array	$H_0H_1H_2H_3H_4$	2.5 1.5 2.0 1.0 0.5
(d) large-platform	H_0H_1	1.0 0.5
(e) short-platform	H_0H_1	1.0 0.5

V.2.1 Flat-bottom topography

In figure 36 the self-organization process is analyzed for topography (a), which has a uniform depth $H_0 = 1.0 \times 10^3 \text{ m}$ (in fact, the flow behavior is independent of this value; in other words, this case corresponds with the purely 2D dynamics). For $t = 0$ ($t = t^*/T$, where t^* is time and T is the rotation period) a flow with cyclonic vorticity covering the whole domain is prescribed. Between $t = 2 - 8$ the vorticity produced at the walls due to the no-slip boundary conditions grows and separates from the boundary, generating two vortices at the upper-right and lower-left corners. For later times ($t = 16 - 60$) the formation of a pattern with alternate circulation cells along the main axis of the domain can be discerned due to the self-organization property of two-dimensional flows. For the present aspect ratio, $\delta = 5$, the final distribution consists of five vortices. This

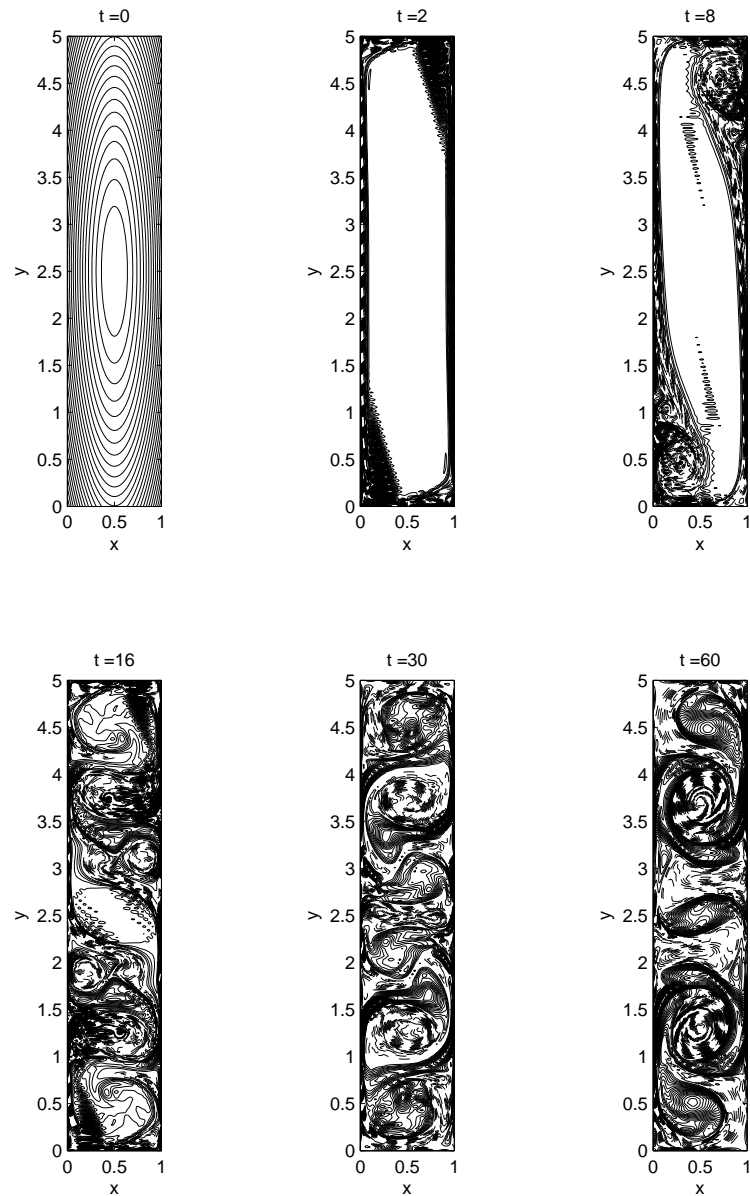


Figure 36. *Vorticity contours from a simulation with a flat-bottom topography (a) with $H_0 = 10^3$ m. Solid (dashed) contours represent positive (negative) values of vorticity. The contour level increment is 10^{-5} s^{-1} . The horizontal dimensions of the rectangular domain are nondimensionalized by using the width of the box $L_x = 200$ km.*

result is nearly independent of the initial condition, since the same result is obtained for different initial flows (not shown here).

The organization of a decaying flow in a set of vortices along a rectangular domain has been studied by several authors, mainly in the context of decaying 2D turbulence

(Maassen *et al.*, 2003) and also in terms of spin-up (or spin-down) processes (van Heijst *et al.*, 1990; van de Konijnenberg and van Heijst, 1996). The flow evolution presented in Figure 36 resembles the spin-up process where three main stages can be discerned: (1) initially, a flow with uniform vorticity is established; (2) afterwards, opposite-sign vorticity is produced at the lateral walls due to the no-slip boundary condition which grows and separates from the walls; and (3) a pattern of nearly circular vortices is formed along the main axis of the domain, with alternate circulations (cyclonic and anticyclonic). The number of cells depends on the aspect ratio δ of the domain. Due to viscosity, the vortices gradually decay until the fluid reaches again the state of solid-body rotation. An important point to remark is that the train of vortices is formed due to the geometry of the domain. In the following subsections we analyze the flow organization for non-flat bottoms.

V.2.2 Step-array topography

In figure 37 a simulation with a step-array topography (b) is presented, using the same initial condition as in the flat-bottom case. The topography consists of five regions with different depth, being $H_0 > H_1 > H_2 > H_3 > H_4$ (see Figure 35). As can be seen comparing with the previous case, the final distribution of the vortices changes dramatically due to the topographic steps. For $t = 2-8$ the effects of the topography are already visible: a flow along all the discontinuities with the shallow region on the right are noticed by the positive (negative) vorticity along the deep (shallow) side of each step. These flows parallel to the topography are expected to appear, since an equivalent result was found in the experiments and simulations presented in previous chapters. Due to the strong flow upward (downward) the steps along the right (left) walls (induced

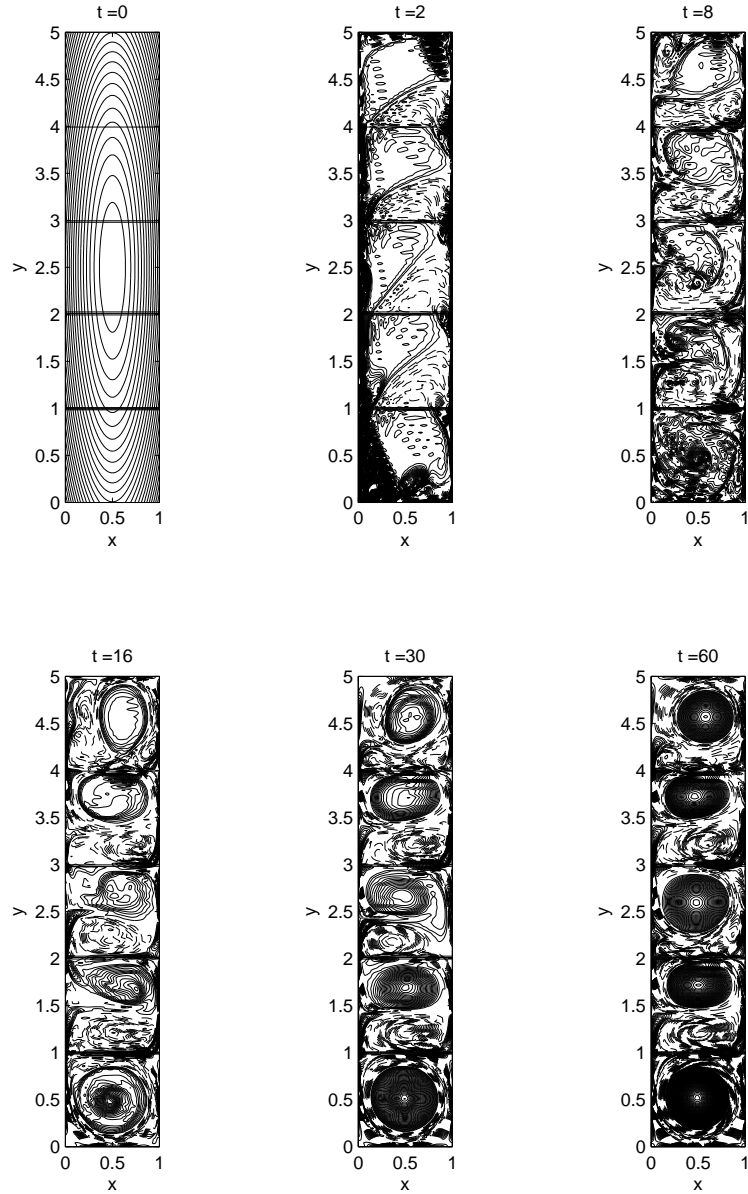


Figure 37. *Vorticity contours as in Fig. 36, but now using a step-array topography (b) consisting of five square regions with horizontal dimensions $200 \times 200 \text{ km}^2$ and depths $H_0 > H_1 > H_2 > H_3 > H_4$ (see Table IV). The step heights at $y = 1, 2, 3, 4$ are $1, 0.5, 0.5, 0.25 \times 10^3 \text{ m}$, respectively.*

by the cyclonic initial condition), potential vorticity conservation arguments can be used to explain the present configuration: a column of fluid going up (down) a step-topography gains negative (positive) relative vorticity. As a result, at $t = 30$ the central regions (with depths H_1, H_2 and H_3) show a cyclonic vortex at their northern parts

and an anticyclone at their southern sides. The deepest and the shallowest regions of the domain (with depths H_0 and H_4) present a cyclonic structure that fills up the entire region, surrounded by an annulus of negative vorticity. At later times ($t = 60$) the cyclonic structures dominate in all regions, although anticyclones in H_1 and H_3 still persist. As can be seen, the topography strongly modulates the self-organization process since the final configuration is dramatically changed compared with the flat-bottom case (Figure 36).

In Figure 38 a simulation with a different step-array topography [case (c)] is presented. The topography consists of five different depth regions with $H_0 > H_1 < H_2 > H_3 > H_4$. In this case, a shallow region (H_1) lies between two deeper regions (H_0 and H_2). As in the previous case, the effects of the topography are already visible for $t = 2 - 8$ and the flow along all discontinuities with the shallow region on the right are observed. One particular aspect of this simulation is that the step at $y = 2$ (between H_1 and H_2) implies that the flow is directed from left to right, in contrast with the flows along the other steps, which move from right to left. As a consequence, an anticyclonic circulation is induced inside the shallow region H_1 . For $t = 16$, it can be observed that this anticyclonic structure prevails over the cyclonic and grows in the central part of H_1 for later times.

V.2.3 Short-platform topography

In this case a platform-topography is used, consisting of a rectangular shallow region placed next to the right boundary at the central part of the domain. The objective now, is to show that a small topographic feature like this is sufficient to induce changes in the final distribution of the vortices (this kind of topography could represent a

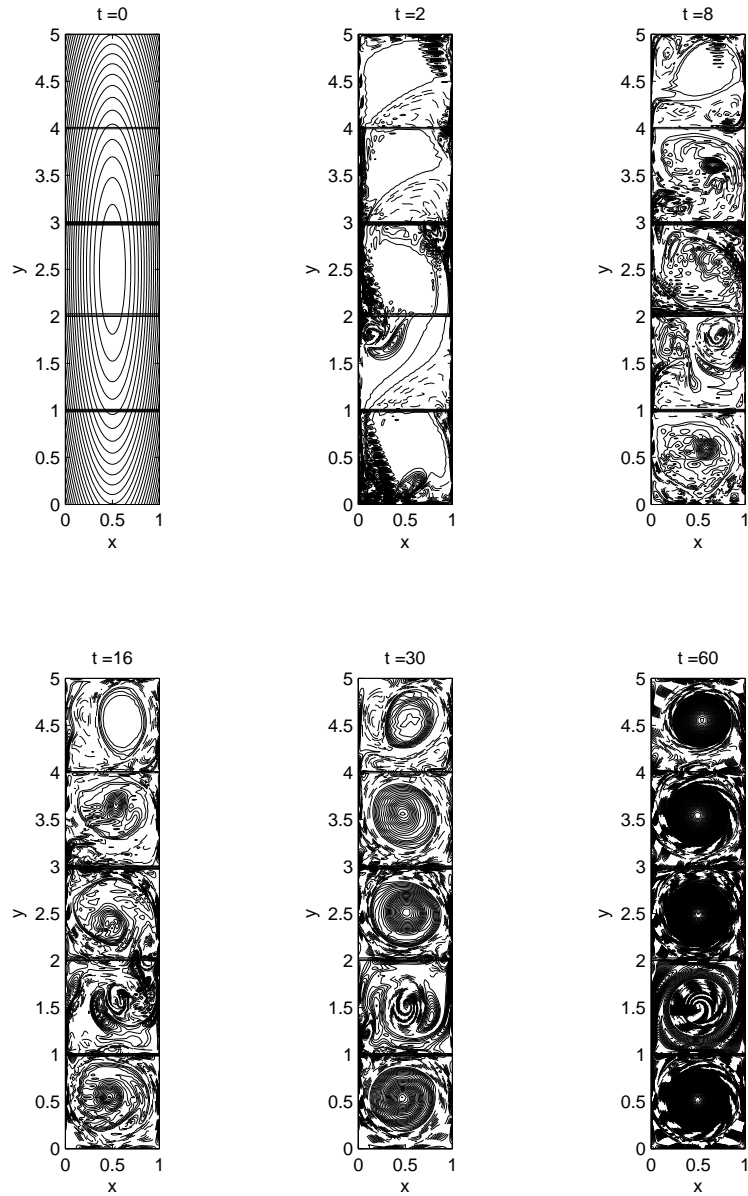


Figure 38. As in the Fig. 37 but now using topography (c) consisting of five square regions with depths $H_0 > H_1 < H_2 > H_3 > H_4$ (see Table IV). The step heights at $y = 1, 2, 3, 4$ are $1, -0.5, 1.0, 0.5 \times 10^3$ m, respectively.

submarine cape). Figure 39 shows the vorticity contours from a simulation using the rectangular platform-topography (d). The platform divides the central square region H_2 in two rectangular regions, one shallow and the other deep, both with dimensions $L_x/2 \times L_y/5$. The rest of the domain has a uniform depth H_0 . As can be observed, the

presence of the rectangular shallow region gives place to a different organization of the flow. The platform acts like an obstacle to the initial flow directed northwards at the eastern boundary, inducing a complicated pattern at the central part of the box. Note that there are three steps with different orientations. As can be seen at early times ($t = 2$) the flow is strong enough to bring water from the deep region to the shallow one, which explains the negative vorticity observed above the platform. Nevertheless, a flow around the platform is formed and detached near the corners. The long-term evolution of the flow is characterized by two anticyclonic vortices at the ends of the rectangular domain, followed by two cyclones and, at the central region, a set of smaller vortices over the platform. The presence of two cyclonic structures just next to the platform region and a four-vortex structure similar to the one discussed in chapter IV for the square domain, seems to be a special distribution for the present bottom geometry.

In Figure 40 the results for a shorter platform are presented. In this case it is clearly seen that the separation of cyclonic structures from the platform prevents the separation of the anticyclonic cells near the end of the domain. Due to this behavior, some anticyclonic vorticity is formed in front of the obstacle by boundary layer detachment. The presence of two cyclones just next to the platform region, force this structure to stay at the deep region in front of the platform ($y \sim 2.5$).

These examples demonstrate that the topography affects dramatically the self-organization process of quasi-2D flows. Figure 41 shows a schematic picture summarizing the results presented in this section.

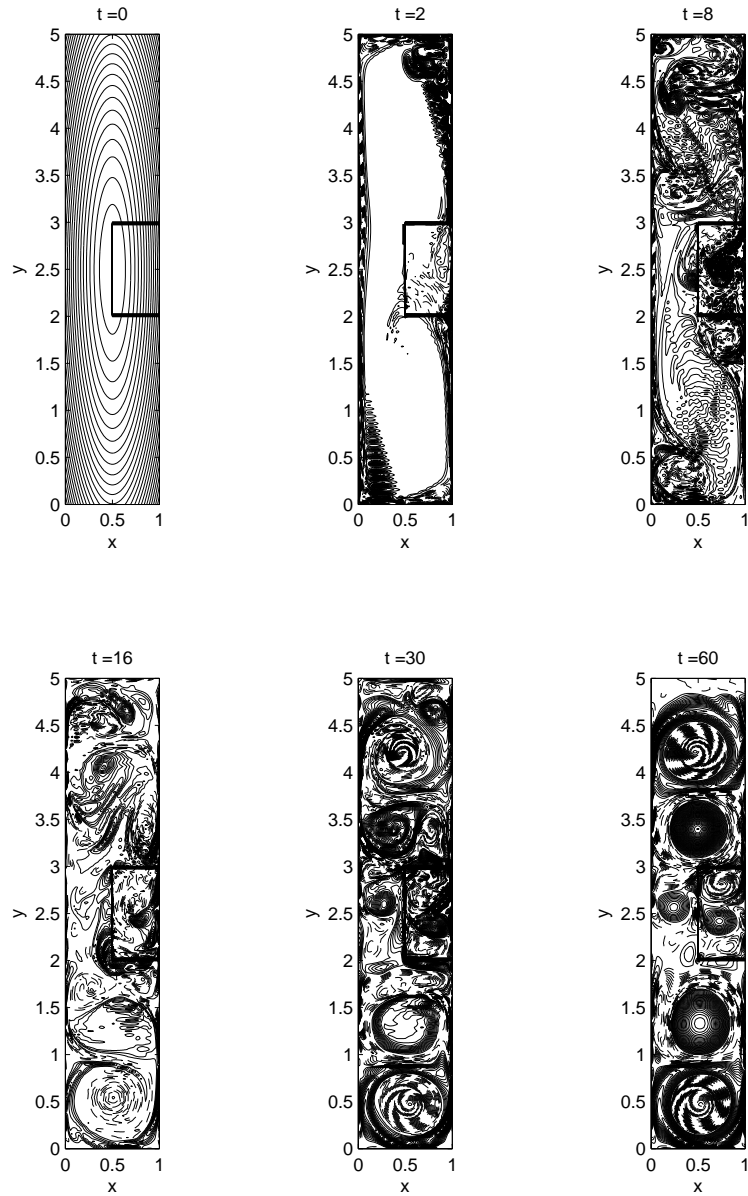
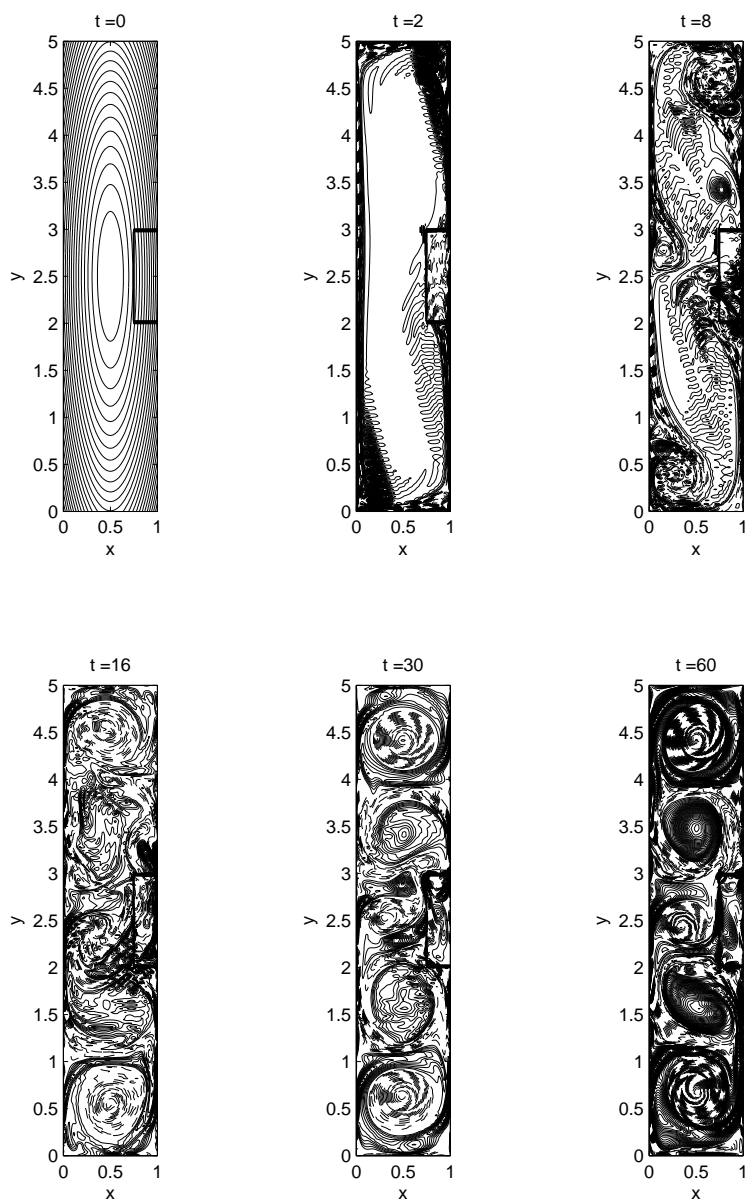


Figure 39. As Fig. 36, but now using the large-platform topography (d) consisting of a rectangular shallow region with horizontal dimensions $L_x/2 \times L_y/5$ and depth $H_1 = 0.5 \times 10^3$ m. The depth outside the platform is $H_0 = 10^3$ m (see Table IV).

V.3 Gulf of California: a regional approximation

It was shown in section V.2 that the presence of different topographic steps affects dramatically the final configuration of quasi-2D flows in a rectangular domain. The domain dimensions were chosen to be similar to the dimensions of the southern region



linespread1

Figure 40. As Fig. 39, but now using the short-platform topography (e).

of the Gulf of California (SGC). In this section, the Regional Ocean Modeling System (ROMS) described in chapter II is used to simulate the circulation in the entire Gulf of California (GC). Some of the simulations have been designed to analyze the formation of vortices at the central and southern regions.

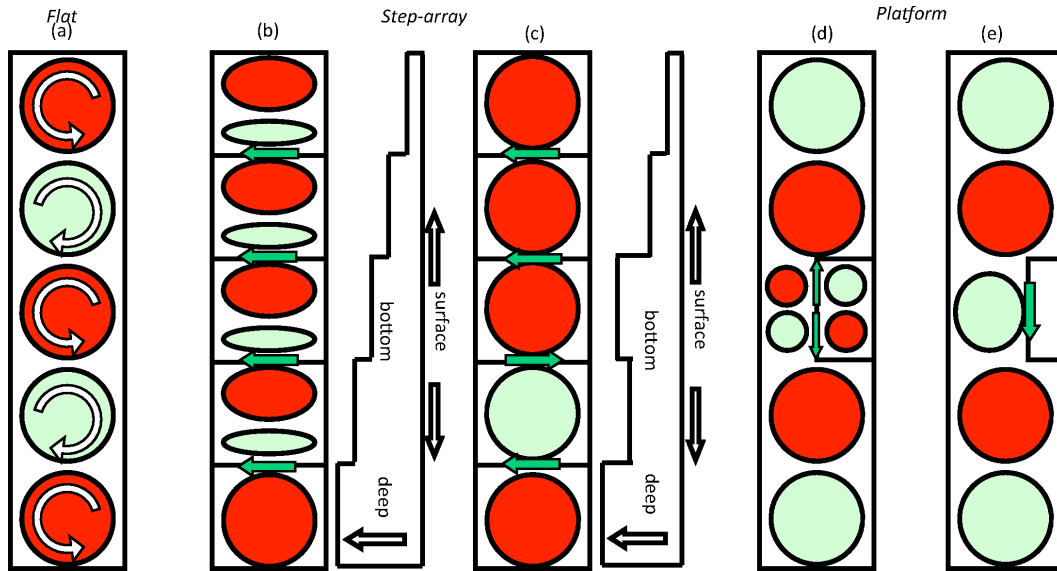


Figure 41. Schematic representation of the final distribution of the vortices found for the different topographies: (a) flat-bottom topography; (b) and (c) step-array topographies; (d) and (e) platform topographies. Dark and white surfaces represent cyclonic and anticyclonic structures, respectively [in panel (a) the sense of rotation of the structures is indicated by the white arrows]. Gray arrows represent the flow direction above the steps.

The aim of the simulations using the ROMS is to investigate the topographic effects on the generation and organization of the vortices in the SGC. The formation of mesoscale gyres and a possible geometrical signal on the flow organization will be also discussed. Several previous studies have described the existence of an eddy-train in the SGC region in the summer (e.g., Figueroa *et al.*, 2003). Nevertheless, the topography signal on this particular process is still unknown. Three simulations are analyzed using three different topographies, as will be described in the following subsections.

The geographical domain is 115° to 106° W and 23° to 32° N. The bathymetry data was obtained from ETOPO2, which is a 2 min gridded dataset (National Geophysical Data Center, 2006). The horizontal grid resolution of the model is $1/12^{\circ}$ and uses the 50 meter isobath as a land-sea boundary. In the vertical, 12 coordinate layers are used.

The model is forced with monthly averaged functions drawn from the COADS, a

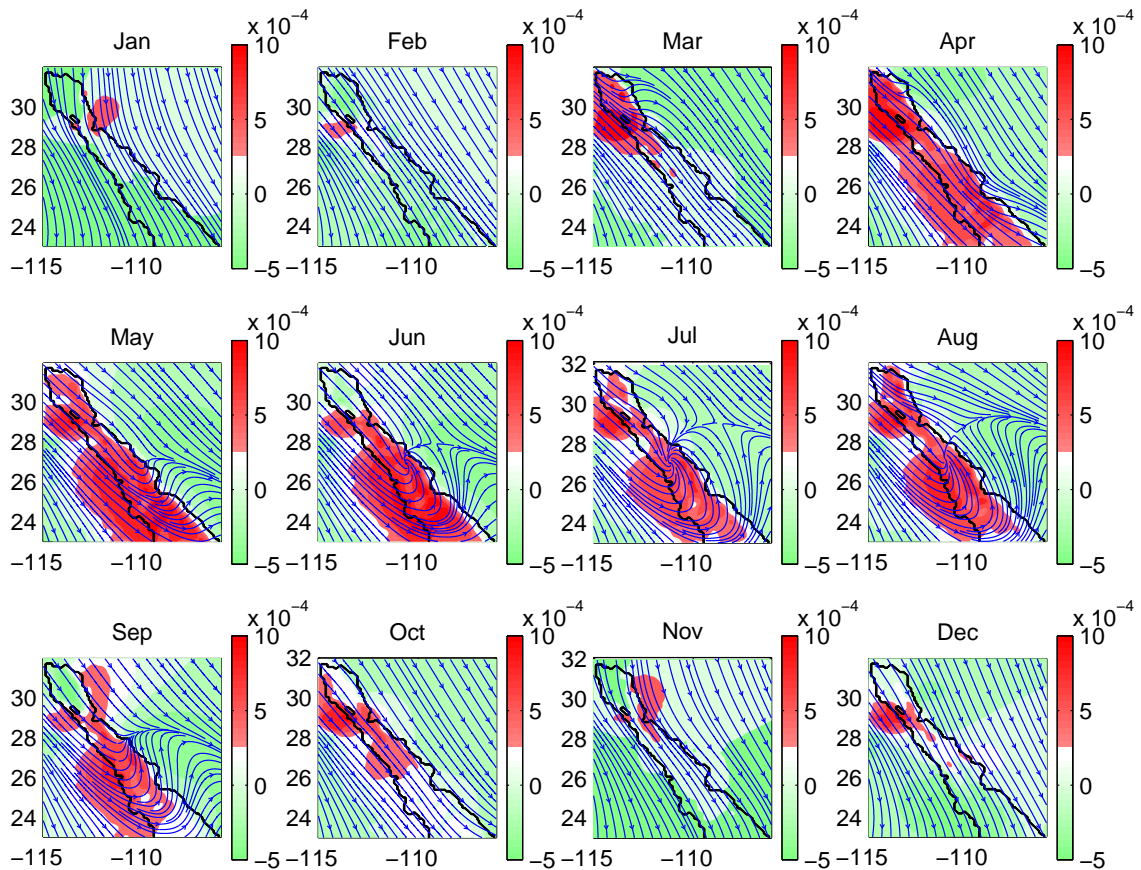


Figure 42. Monthly average of the horizontal wind field: streamline contours and vorticity surfaces.

global atlas of marine data at $1/2^\circ$ resolution (Da Silva *et al.*, 1994). The forcing fields included are the surface wind stress, sea surface salinity, surface net heat flux and heat flux sensitivity to sea surface temperature, surface freshwater flux (evaporation-precipitation) and sea surface temperature. The monthly climatology of the sea surface temperature was obtained from Pathfinder satellite observations (Casey and Cornillon, P., 1999). No-slip boundary conditions are imposed on the lateral boundaries and the open boundary at the entrance of the Gulf is initially forced with temperature, salinity and velocity data from the World Ocean Atlas 2001 climatology (Conkright *et al.*, 2001). Tides are not included.

One of the main forcing agents of the GC circulation is the wind. Figure 42 shows

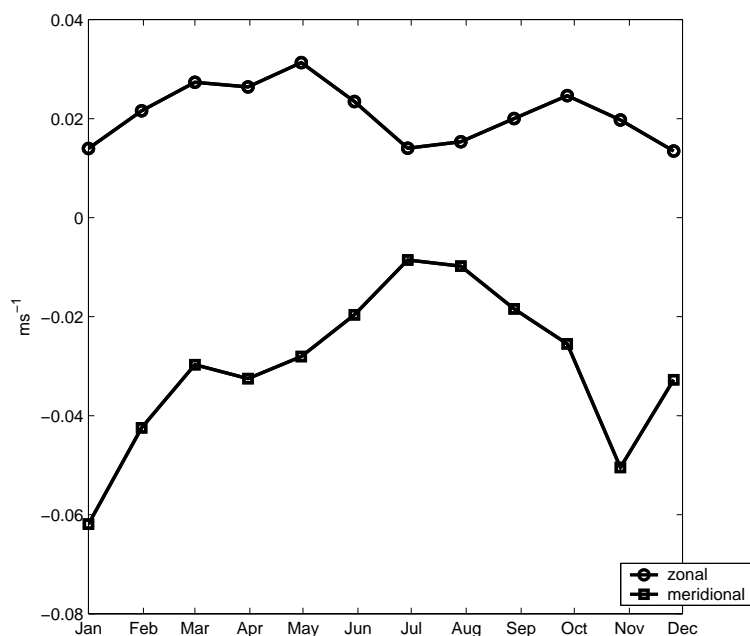


Figure 43. *Monthly average of the zonal and meridional components of the horizontal wind velocity.*

the monthly mean field of the wind used to force the model, as well as the curl, for the year 2005. Figure 43 shows the monthly mean amplitude of the zonal and meridional components of the wind for the same year. As can be seen, the wind is mainly south-eastward between October and April, with two maxima (in absolute value) in the mean meridional component during November and January. In the period between May and August the wind presents an opposite behaviour since in the southern part the monthly mean presents a northeastward direction. The average magnitude of the wind during this period is clearly smaller than the wind during winter and spring. Notice the strong decay of the mean averaged components of the wind during the period from May to July (Figure 43). This short period could represent a relaxation of the wind transfer of momentum to the ocean. Nevertheless, the spatial variability of the wind generates strong atmospheric vorticity which is transferred to the sea by turbulent momentum fluxes. This is clearly observed in the curl map where the maximum values are found

in this particular period.

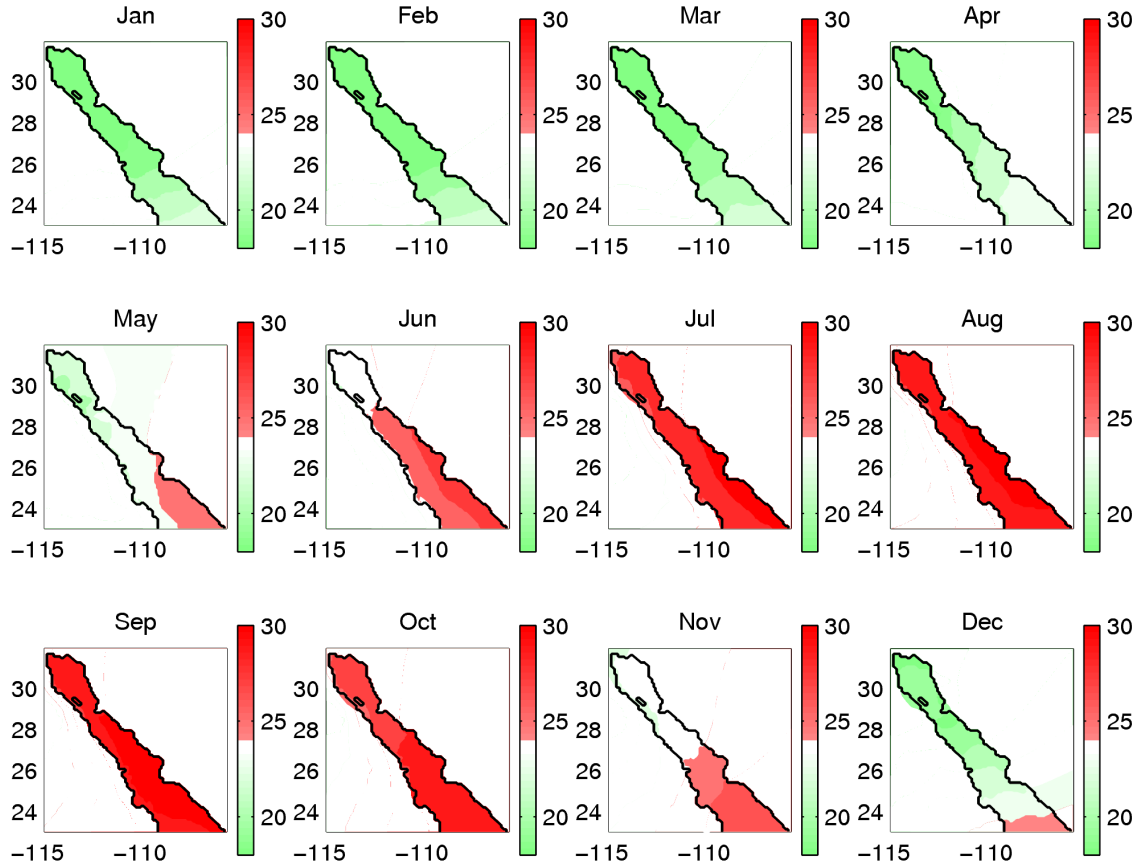


Figure 44. *Monthly sea surface temperature [C°].*

Other forcing agent used in the simulations is the sea surface temperature (SST) shown in Figure 44. It can be seen that the period from November to April presents the stronger gradient of temperature along the main axis of the Gulf, being colder in the north and warmer in the south. The period from July to October is characterized by a very uniform distribution of the sea surface temperature in the GC.

V.3.1 Real topography

Let us first analyze a numerical simulation with a realistic bathymetry. The GC topography was obtained by bi-linear interpolation of the ETOPO2 data. The depth of

the shallower region was fixed at 50 m. The resulting topography, referred to as "real", is shown in Figure 45. The GC can be divided into three zones. The entrance zone (EGC) that is in communication with the Pacific Ocean and is characterized by maximum depths of ~ 3000 m and a wider shelf-platform at the main-land side compared to the peninsula side. This wider shelf continues through the southern zone of the Gulf (SGC) characterized by a set of five basins arranged along the main axis ($\delta \sim 5$). The depths of the basins range from 2500 m to 250 m. Another important feature of this region is the irregular shape of the eastern coast-line where a cape in front of the Farallon basin can be discerned. The northern zone (NGC) is almost flat and very shallow.

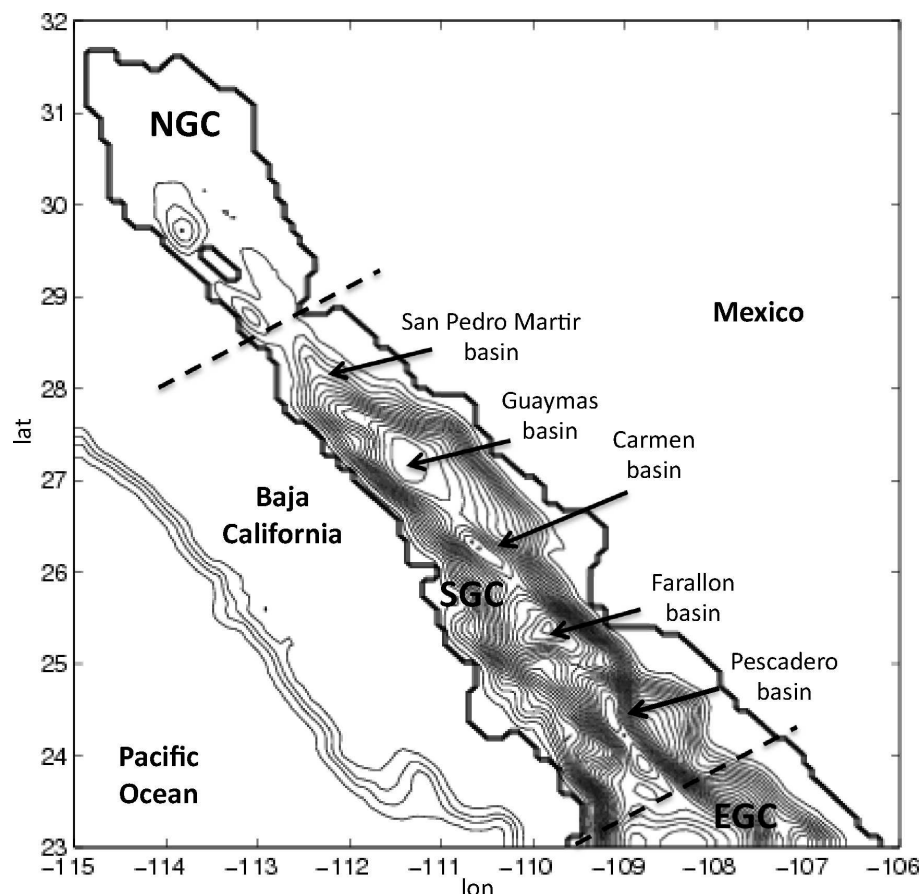


Figure 45. Plan view and topographic contours of the GC. The coast-line is defined by the 50 meter isobath. The contour interval is 100 m. The Gulf is divided in northern, central, southern and entrance regions and are referred to as NGC, SGC, and EGC, respectively. The principal basins in the SGC are also indicated.

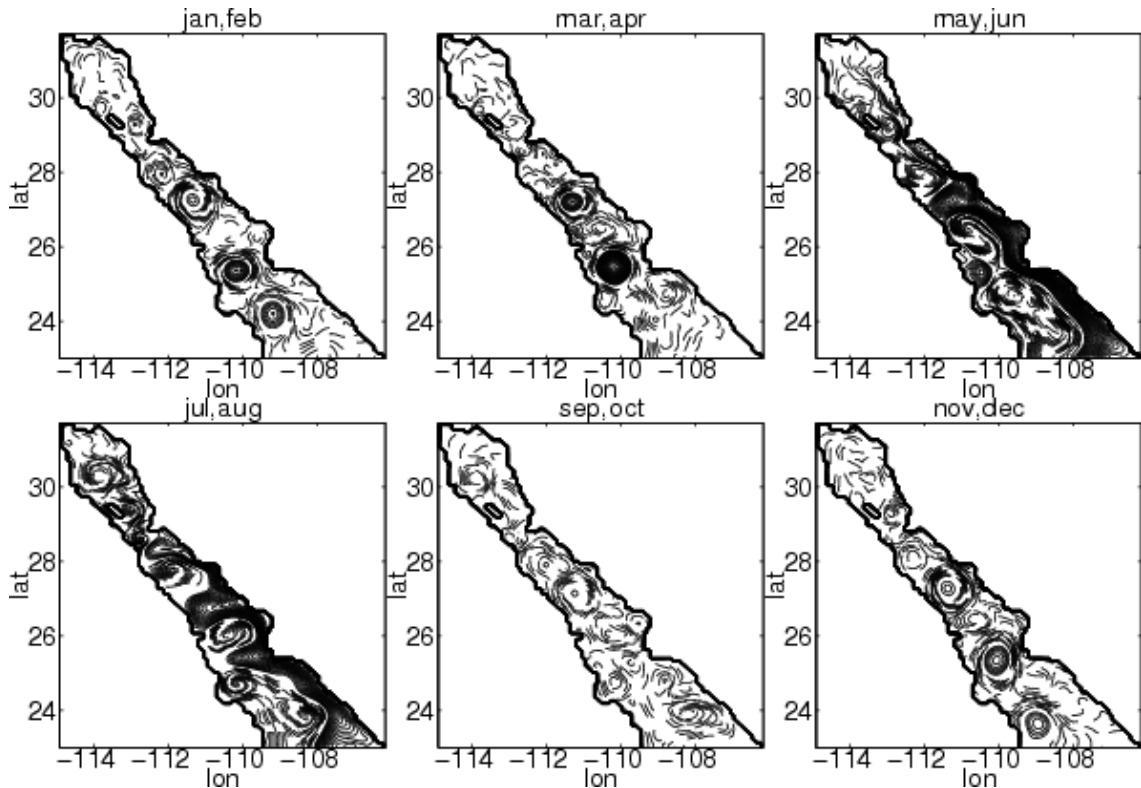


Figure 46. Two-month averaged sea surface height in a simulation using a real topography. The continuous (dashed) contours represent positive (negative) altimetry values. The contour level increment is 10^{-3} m.

In Figure 46 the two monthly averaged maps of the sea surface height (SSH) are shown for the entire GC. Several features can be observed, such as the constant presence of vortex structures in all regions during the entire period. Nevertheless, a completely different regime is clearly noticed during the summer period (May to June and July to August). At the beginning of the summer period, the flow is characterized by the entrance of an eastern boundary current. Later in the summer, this current gets weaker and a number of mesoscale eddies become more evident and dominate the circulation in the SGC region (the same phenomenon was described by Lavín *et al.* (1997)). In order to better understand this behaviour, Zamudio *et al.* (2008) studied the effects of the local wind and the effects of the oceanic remote forcing on the generation of the SGC eddies during the summers of 1999 and 2004. They found that the local wind is not

essential for the generation of these eddies, in contrast with the oceanic remote forcing from the Pacific. The authors concluded that the monthly variability of the currents and sea surface height in the SGC is mainly due to the poleward eastern boundary currents and that interactions with topographic irregularities (capes and ridges) generate the SGC eddies.

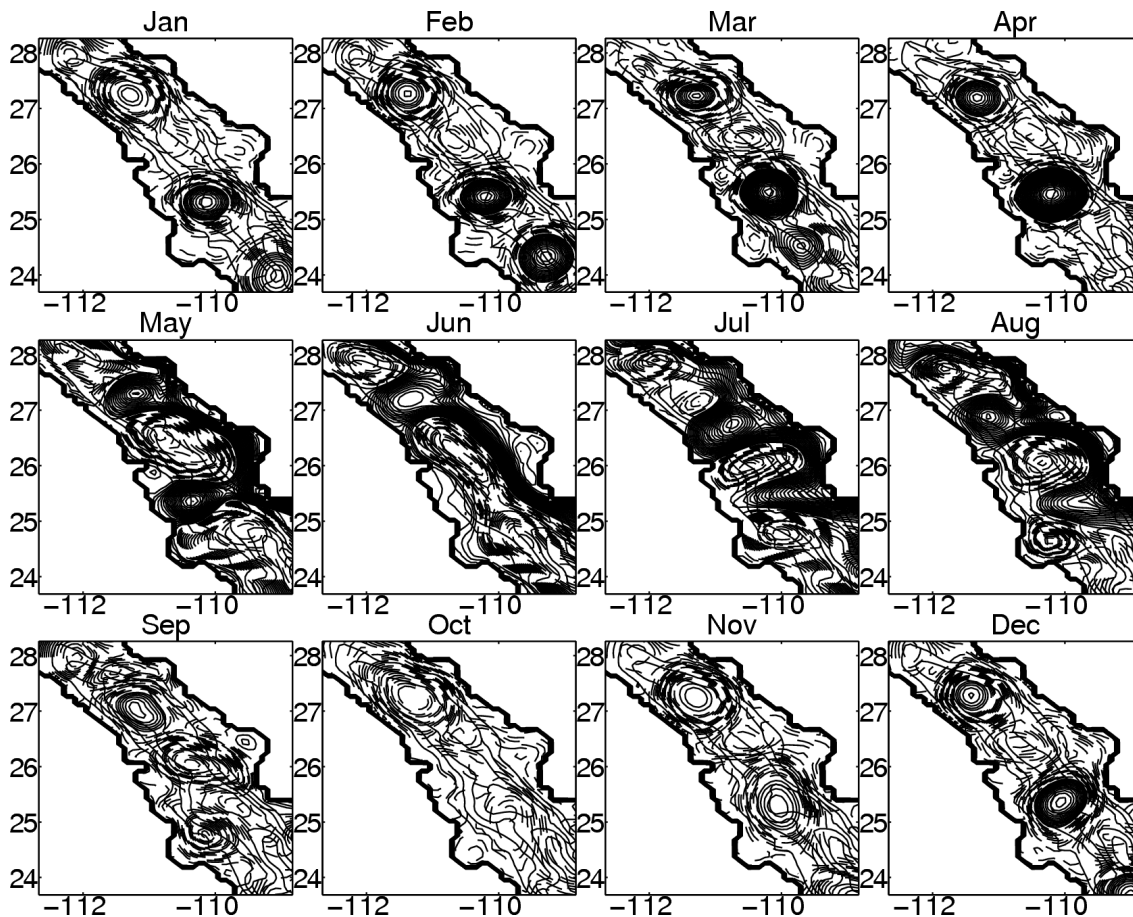


Figure 47. Monthly averaged sea surface height for 2005 using a real topography for the SGC region. The continuous contours represent positive altimetry values and dashed contours negative values. The contour levels as in Figure 46.

In Figure 47 the SSH monthly means are shown in the SGC region. For the period of January to March three anticyclonic structures are observed above the Pescadero, Farallon and Guaymas basins. In April, the anticyclonic structure above Pescadero basin travels north and merges with the one above Farallon basin. During May and

June the flow along the continental coast is established and a cyclonic circulation at the southern basis (Pescadero to Guaymas) is formed. During July and August there is an intensification of the eastern boundary current, which starts meandering and results in an alternate eddy distribution along the main axis of the Gulf with anticyclonic structures in the Farallon and Guaymas basins, and cyclonic structures in the Pescadero, Carmen and San Pedro Martir basins.

V.3.2 Flat-bottom topography

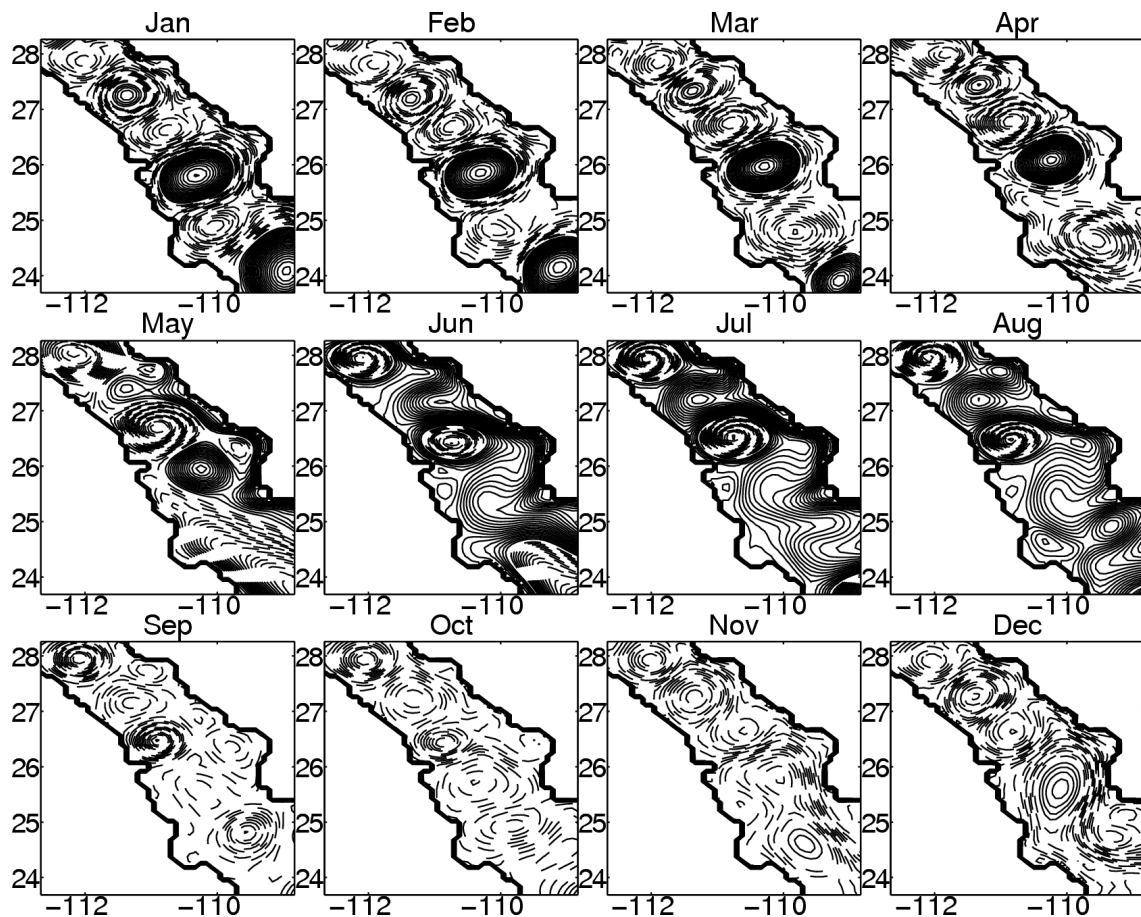


Figure 48. Monthly averaged sea surface height for 2005 using a flat-bottom topography for the SGC region. The continuous contours represent positive altimetry values and dashed contours negative values. The contour levels as in Figure 46.

In order to investigate the influence of the topography on the described eddy-train,

a simulation was carried out using the same forcing conditions, but now with a flat-bottom topography. The uniform depth is 500 m over the entire GC. In order to use the same initial conditions as the case before, the real topography is used at the open boundary. Figure 48 shows the SSH monthly means. As can be seen, from January to May the results are very similar to the previous case. For instance, a very persistent anticyclonic structure around 26° North is observed in both simulations (compare with figure 47). This suggests a weak effect of the topography on the circulation of the region during the first months of the year. However, there are several differences in terms of the dimensions and positions of the structures generated during the rest of the year. In the flat-bottom case, the eddy-train of alternating structures is more evident in the beginning of the summer period (June). The detachment of the eastern boundary current at $\sim 26^\circ$ N is stronger and reaches the western boundary. This result suggests that the eastern boundary current in previous simulations is confined to the coast by the real topography, and it crosses to the western boundary through the passages between the basins.

V.3.3 Step-like topography

In this section, a numerical simulation with an idealized step-topography is presented. Two discontinuities are prescribed dividing the GC in three different depth regions (see Figure 49). The southern discontinuity, with 250 m height is indicated by the black line orientated perpendicular to the lateral boundaries on the Farallon region. The step divides the domain in a southern deep part with 750 m depth and a northern, shallower region with 500 m depth. A second discontinuity with 250 m height, separates the SGC from the NGC region at 28° north.

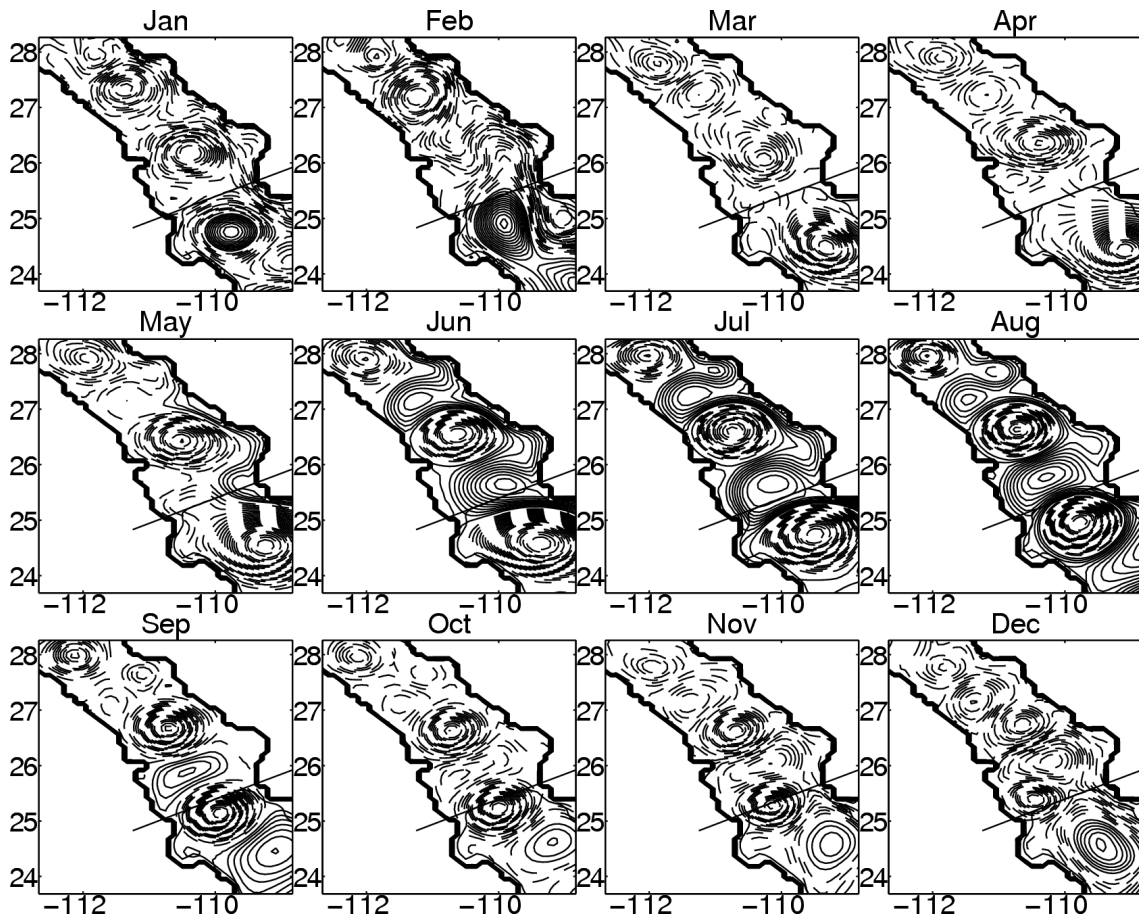


Figure 49. Monthly averaged sea surface height for 2005 using a step-like topography for the SGC region. The continuous contours represent positive altimetry values and dashed contours negative values. The contour levels as in Figure 46.

Figure 49 shows the SSH monthly means. Substantial differences can be found when comparing with the two cases described before (real and flat topographies). The eastern boundary current in June is forced to detach from the continental coast towards the peninsula along the southern discontinuity, while maintaining the shallow water on the right. This behaviour is similar to the results found in section V.2 and also to the experimental observations presented in chapters III and IV. This is clearly noticed during the rest of the summer period, where a persistent cyclonic structure remains at the deep side of the step and an anticyclone on the shallow side. Again, larger structures are formed, mainly anticyclonic.

V.3.4 Comparison between simulations

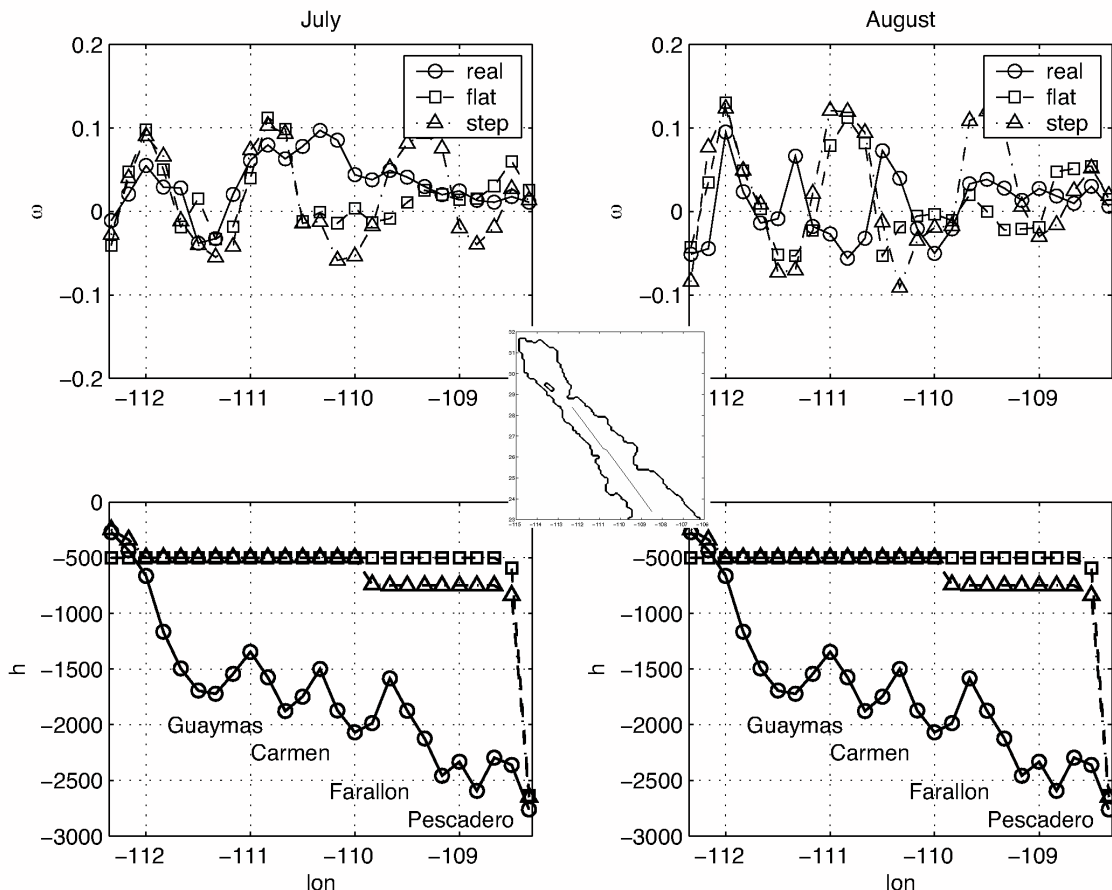


Figure 50. *Upper panels: mean relative vorticity along the main axis of the Gulf (shown at the central panel) during July and August in the three regional simulations. Lower panels: the three topographies used in the simulations. The transect is 800 km long and the space between data is 32 km.*

As shown in previous sections, the topography plays a role on the position of the structures in the SGC region as well as on the dimensions and intensity, particularly in the summer period. In order to compare these effects, Figure 50 shows the monthly mean surface vorticity for July and August along the main axis of the Gulf, where the main vortices are formed. During July all three cases are quite similar on the northern part of the SGC region between 112.5° and 110.5° W, with an anticyclonic structure between to cyclones. To the south, the simulations are very different. The real-topography

case presents a cyclonic circulation that extends from the Guaymas to the Pescadero basin. The flat-bottom gulf presents weaker cyclonic and anticyclonic structures up to the entrance zone. On the step-topography case, the eddy-train continues with a cyclonic structure between two anticyclones. This distribution is strongly influenced by the step-topography at 110° W where a cyclone (anticyclone) is formed at the deep (shallow) part next to the discontinuity. During August, the idealized simulations (flat and step topographies) maintain a similar distribution as in July along the whole SGC region. In contrast, the real-topography case is dramatically changed. As can be seen, the region between the Guaymas and the Farallon basins shows more eddies than in the previous month. However, their positions do not coincide with the vortices generated in the other simulations, except at the northern and southern ends of the transect. This result is a strong evidence on the topographic effects on the organization of the flow at the region.

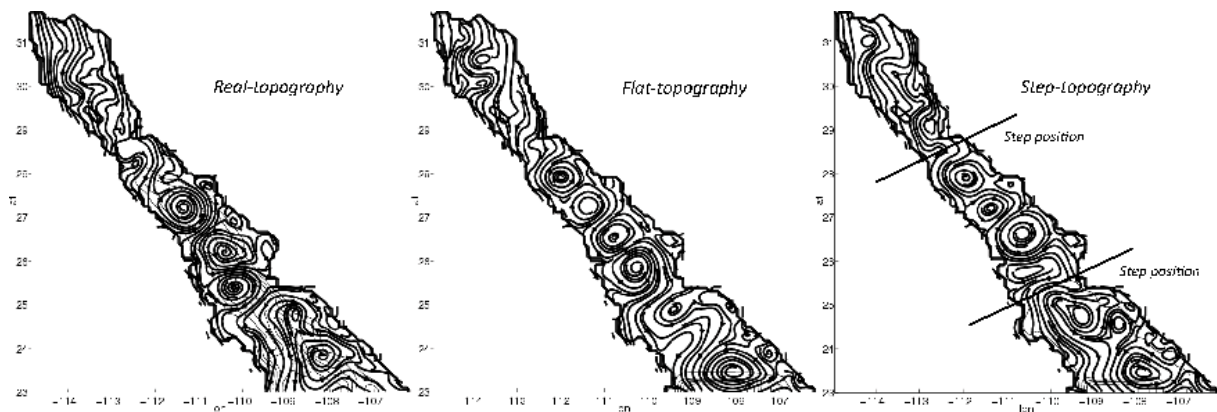


Figure 51. Streamline contours representing the annual mean surface circulation of the GC for the three topographies used in the numerical simulations. The arrows indicate the sense of motion. The contour interval is 5×10^{-3} .

In order to have a global idea of the bottom-topography effects on the circulation of the entire GC, in Figure 51 the annual mean surface circulation is shown for the three different experiments (real, flat and step topographies). As can be seen, the annual

averaged circulation presents well-organized, counter-rotating mesoscale eddies in all cases. The gyres are smaller and elongated along the Gulf for the simulation with the realistic topography.

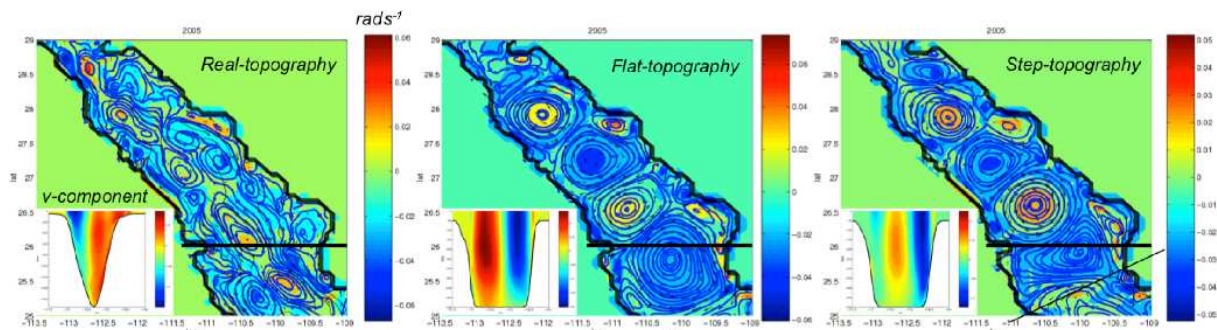


Figure 52. Annual mean bottom circulation in part of the SGC region. Relative vorticity distributions are represented by colors. The contours represent streamlines, with the sense of motion indicated by the arrows. The longitudinal black line represents the position of the vertical section shown in the insets.

Figure 52 shows the annual averaged bottom circulation for the SCG region. Relative vorticity and streamlines are presented. In addition, the meridional velocity component is shown for a longitudinal vertical section indicated by the black line. There are differences between the real-topography simulation and the idealized topographies. The simulation with flat and step topographies are characterized by a strong barotropic signal with the vortices almost filling the entire depth (see the vertical section). In both simulations the horizontal bottom circulation is characterized by a set of well-defined counter-rotating vortices. In contrast, in the real-topography case the circulation near the bottom is dominated by the shape of the ocean floor, which makes the vortex structure more elongated along the axis of the Gulf.

V.4 Discussion and conclusions

In this chapter, two numerical models have been used to investigate the organization of a train of counter-rotating mesoscale eddies that characterize the summer circulation in the Gulf of California. The SWEVOL simulations were designed to investigate the organization of quasi-2D flows in rectangular domains, and the ROMS to simulate the Gulf of California under more realistic conditions.

The rigid-lid, shallow water model (SWEVOL) was used to simulate the organization of quasi-2D flows in a rectangular domain with aspect ratio $\delta = 5$, similar to the dimensions of the southern part of the Gulf of California. Different idealized topographies were chosen to resemble some abrupt bathymetric features along the region of study (see Figure 35). The basins along the Gulf are represented by two step-topographies, consisting of five square regions with different depths, where the formation of stable vortices is persistently observed. Topographic irregularities, such as capes and ridges extending offshore, are idealized by a platform placed next to the eastern long wall, representing the continental side of the Gulf. A cyclonic circulation around the central point of the domain was used as initial condition, resembling the GC poleward eastern current observed in the beginning of the summer period. It was found that the organization strongly depends on the topographic configuration. A flat-bottom topography was also used in order to compare with a typical flow organization only due to the geometrical shape of the domain.

The flat-bottom simulation with the SWEVOL model was used as a reference case. The purely 2D flow in rectangular domains was studied in detail by van Heijst *et al.* (1990) and Maassen *et al.* (2003). For $\delta = 5$, the final distribution consists of five alternated vortices aligned along the main axis of the domain. When a step-array

topography is used, the final configuration is dramatically changed. For topography (b) in Figure 35, in which the regions have a decreasing depth, cyclonic structures dominate in all regions, all of them having a flow parallel to the discontinuity, towards the peninsula (left wall). When there is a shallow region between two deep regions, as in topography (c), a final configuration with a unique anticyclonic structure in the shallow region is obtained. These examples show that abrupt changes of depth have a tendency to promote the formation of mesoscale vortices over the regions isolated by the topographic steps. The simulations have shown that such a mechanism is very effective in the barotropic limit.

The effect of a platform topography at the eastern wall provided some evidence on the mechanism for the formation and positioning of vortices. It was found that a small topographic irregularity is sufficient to induce a change in the final distributions of the vortices. The irregularity acts like an obstacle inducing complicated patterns of the flow depending on the dimensions of the obstacle. If the platform is small, an anticyclonic structure is formed in front of it, but if it is larger, a more complicated pattern is formed. These results show that the geometry of the eastern boundary seems to be fundamental for the positioning of the eddies along the main axis. The formation of anticyclonic structures in front of the strong eastern boundary irregularity in front of the Farallon basin (*i.e.* the Topolobampo Cape) supports this idea. This result was suggested by Zamudio *et al.* (2008), who reported that SGC eddies are generated by the Pacific Equatorial boundary current interactions with topographic irregularities, such as capes and ridges extending offshore. This mechanism has also been discussed by A. Parés (personal communication).

The second model (ROMS) was used to simulate the Gulf of California. Three simulations using different topographies were carried out under the same forcing conditions.

It was found that the topography plays a role in the flow organization. However, the geometry of the Gulf seems to be fundamental for the summer organization of the flow into a well-defined set of counter-rotating mesoscale eddies. The train of mesoscale vortices is more evident during a possible relaxation period of the predominant wind in the late summer (Figure 43), when the formation and positioning of the structures are associated with the intense Pacific eastern boundary current and topographic effects (bottom and coastal). Indeed, this intense current separates from the continent and gives rise to the formation of the vortices. This notion is reinforced by the results of the simulation using a flat-bottom topography, in which this separation is stronger. Under the same forcing conditions and using an abrupt step-like topography, a strong anticyclonic structure is formed.

Summarizing, in both models similar results were obtained: an eddy-train configuration under decaying conditions influenced by topographic effects. It was shown that the relative simplicity of the 2D models can be used as a first approximation to explain realistic phenomena in the ocean. As a final remark, it is emphasized that oceanographic research can be supported by experimental results, where the idealization of the system leads to valuable information for interpreting observational data.

Chapter VI

Conclusions and final remarks

The self-organization of quasi-two-dimensional flows, confined within a closed domain and over different idealized step-like topographies in a rotating system, has been investigated. It was found that the organization process strongly depends on the presence of the topographic steps, which induce specific geometrical arrangements of the flow after several rotation periods. Besides the solid bottom, the lateral walls also play an important role. In a bounded domain, the no-slip walls act as a source of vorticity that is injected into the flow interior (van Heijst *et al.*, 2006). These vorticity filaments interact with vortices in the interior of the domain and form larger structures in a process strongly modulated by the topography. The result is a well-organized flow made by nearly circular coherent structures that fill the entire geometrical regions delimited by the lateral walls and the topography. This result is founded on laboratory experiments and numerical simulations in different geometries and bottom step topographies. The main results have been used to explain a topographical mechanism behind the organization of the eddy-train of counter-rotating structures that characterize the surface circulation in the southern region of the Gulf of California.

Laboratory experiments of decaying turbulent flows were carried out on rectangular (chapter III) and square (chapter IV) domains with aspect ratio $\delta = 2$ and $\delta = 1$, respectively. A discontinuous topography (step-like) was used to divide the domains in two regions, being one deep and the other shallow. In both cases, a flow along the topography that always maintains the shallow region to the right was found. Two

persistent structures at the end of the step due to the interaction of the flow with the vertical wall were systematically observed. The flow along the topography inhibits the exchange of fluid between the shallow and the deep regions. As a result, the flow inside the subdomains evolves almost independently. Due to Ekman effects, always present in laboratory experiments, the self-organization process is halted before reaching a complete organization of the flow.

Numerical simulations based on a shallow-water model of decaying quasi-two-dimensional turbulence were carried out under the same conditions used in the experiments with rectangular and square domains. A strong agreement between the simulations and the experiments was found. In order to study the full self-organization process, numerical simulations were performed without Ekman friction. The same principal features as in the experiments were observed, but now a complete organization of the flow was obtained. For the rectangular domain, the long-term configuration of the flow consisted of two coherent structures placed one at each region. In some cases, a cyclonic vortex occupied the shallow region while an anticyclone dominated the deep side, or vice versa. The sense of rotation of the final structures was found to be dependent on the initial condition: slightly different initial conditions in several numerical simulations lead to different arrangements, and therefore it was impossible to predict the long-term configuration of the flow. In the square container, in contrast, a final state of the flow composed by four vortices alternately disposed was found. In this case, the flow at the deep subregion is a cyclone-anticyclone pair trying to climb the step, and the mirror structures at the shallow side. An important difference with the rectangular domain is that this four-vortex flow organization is systematically observed, regardless of the initial condition.

The existence of a preferential distribution of the vortices due to a geometrical

signal induced by the discontinuity is a relevant result. In the present geometries and topographic configurations, the preferential distribution depends on the relation between the length of the discontinuity and the length of the lateral walls.

The results observed with simple step-topographies can be used to interpret the evolution of geophysical flows in an oceanographical context. With this purpose, a regional model (ROMS) was used to simulate the circulation in the Gulf of California in a realistic way. The objective was to study the topographic effects on the formation and organization of the counter-rotating mesoscale eddies that characterize the summer circulation in the southern region. An additional set of simulations performed with the shallow-water model was used to model the Gulf as a rectangular domain with aspect ratio $\delta = 5$. It is worth noting that the relatively simple 2D model provides useful information to understand better and improve the description of the more realistic ROMS simulation.

From the laboratory models to the Gulf of California simulations, the topographic effects were studied using idealized geometries and topographies. A general conclusion is that the combination of experiments and simulations proved to be a useful tool to gain a better understanding of some particular physical processes involved in the organization of turbulent oceanic flows. The use of two essentially different numerical models also led to relevant information on the formation and positioning of vortices along the domain. The simplicity of the shallow water model facilitates a physical interpretation of the results, while the regional model allows to establish a relation between the quasi-2D physical mechanism and the processes occurring under more realistic conditions.

It should be pointed out that additional work needs to be done concerning the eddy-train formation and organization in the Southern part of the Gulf of California. In particular, the possible baroclinic effects on the flow structures require further inves-

tigations. In the simulations with the ROMS model, a few number of layers of fluid were used (12). The main idea was to connect these results with the barotropic, shallow-water model used in the simulations with closed domains. This procedure was based on several studies that have revealed the strong barotropic character of the vortices that are formed in the region (e.g. Zamudio *et al.*, 2008); nevertheless, a possible baroclinic effect stays uncertain. Another interesting feature that needs more attention in future works is the characterization of the flow along the step-like topography. Such a step current has been described in a number of previous experimental studies (Spitz and Nof, 1991; Zavala Sansón *et al.*, 2005; Tenreiro *et al.*, 2006). This flow appears from the interaction of the vortices with the bottom topography and an oscillatory behavior is easily noticed in the vorticity field. Thus, there might be the presence of waves that seem to be trapped to the step topography.

Another important aspect is the dependence of the flow organization on the initial condition in both the experiments and the simulations. Indeed, a more universal validity of the long-term organization of vortices should be analysed in terms of the characteristics of the initial condition: the number and arrangement of initial structures, as well as their strength and size. Finally, there is a strong dependence between the length of the bottom discontinuity and the length of the lateral walls associated with the existence of a preferential distribution of the vortices in confined, decaying turbulent flows. In order to establish this relation, future work needs to be done for different aspect ratios δ and step orientations.

Bibliography

- Al Saafani, M. A., S. S. C. Shenoi, D. Shankar, M. Aparna, and J. Kurian (2007). Westward movement of eddies into the Gulf of Aden from Arabian Sea. *J. Geophys. Res.*, **112**(C11004).
- Argote, M. L., M. F. Lavín, and A. Amador (1998). Barotropic eulerian residual circulation in the Gulf of California due to M_2 tide and wind stress. *Atmósfera*, **11**: 173–197.
- Batchelor, G. K. (1967). An introduction to fluid dynamics. *Cambridge University Press*.
- Beier, E. and P. Ripa (1999). Seasonal gyres in the Northern Gulf of California. *J. Phys. Oceanogr.*, **29**: 305–311.
- Berkooz, G., P. Holmes, and J. L. Lumley (1993). The proper orthogonal decomposition in the analysis of turbulent flows. *Annu. Rev. Fluid Mech.*, **25**: 539–75.
- Bretherton, F. P. and Haidvogel, D. B. (1976). Two-dimensional turbulence above topography. *J. Fluid Mech.*, **78**: 129–154.
- Casey, K. S. and Cornillon, P. (1999). A comparison of satellite and in situ based sea surface temperature climatologies. *J. Climate*, **12**: 1848–1863.
- Castro, R., A. S. Mascarenhas, R. Durazo, and C. A. Collins (2000). Seasonal variation of the temperature and salinity at the entrance to the Gulf of California, Mexico. *Ciencias Marinas*, **26**(4): 561–583.
- Castro, R., M. F. Lavín, E. Beier, and A. Amador (2007). Structure of mesoscale eddies in the southern Gulf of California during cruise NAME-2 (August 2004). *Eos Trans. AGU*, **88**(23).
- Clercx, H. J. H. and van Heijst, G. J. F. (2009). Two-dimensional Navier-Stokes turbulence in bounded domains. *Appl. Mech. Rev.*, **62**: 020802–1/25.
- Clercx, H. J. H., S. R. Maassen, and G. J. F. van Heijst (1998). Spontaneous spin-up during the decay of 2d turbulence in a square container with rigid boundaries. *Phys. Rev. Lett.*, **80**(23): 5129–5132.
- Clercx, H. J. H., S. R. Maassen, and G. J. F. van Heijst (1999). Decaying two-dimensional turbulence in square containers with no-slip or stress-free boundaries. *Phys. Fluids*, **11**(3): 611–626.

- Conkright, M. E., Locarnini R. A., Garcia, H. E., O'Brien, T. D., Boyer, T. P., Stephens, C., and Antonov, J. I. (2001). World Ocean Atlas: Objective analyses, data statistics, and figures cd-rom documentation. *NOAA NODC WOA01*.
- Da Silva, A., Young, C.C., and Levitus, S (1994). Atlas of surface marine data 1994, vol. 1, algorithms and procedures. *NOAA Atlas NESDIS 6, U. S. Department of Commerce, NOAA, NESDIS, USA, 74 pp.*
- Emery, W. J. and Thomson, R. E. (2001). Data analysis methods in physical oceanography. *Elsevier Science Publishers*.
- Figueroa, J. M., S. G. Marinone, and M. F. Lavín (2003). A description of geostrophic gyres in the Southern Gulf of California. *O.U. Velasco Fuentes et al. (eds.), Nonlinear Processes in Fluid Dynamics, 237-255. ©2003 Kluwer Academic Publishers.*
- Grimshaw, R., D. Broutman, X. He, and P. Sun (1994). Analytical and numerical study of a barotropic eddy on a topographic slope. *J. Phys. Oceanogr.*, **24**: 1587–1607.
- Gutiérrez, O. Q., S. G. Marinone, and A. Parés-Sierra (2004). Lagrangian surface circulation in the Gulf of California from a 3D numerical model. *Deep-Sea Research II*, **51**: 659–672.
- Haidvogel, D. B., H. G. Arango, K. Hedstrom, A. Beckmann, P. Malanotte-Rizzoli, and A. F. Shchepetkin (2000). Model evaluation experiments in the North Atlantic Basin: simulations in nonlinear terrain-following coordinates. *Dyn. Atmos. Oceans*, **32**: 239–281.
- Hansen, A. E., D. Marteau, and P. Tabeling (1998). Two-dimensional turbulence and dispersion in a freely decaying system. *Phys. Rev. Lett.*, **58**(6): 7261–7271.
- Hartmann, D. L. (2008). ATM S 552 Notes: “Objective analysis”. *Department of Atmospheric Sciences, University of Washington*, (4): 51–86.
- Herring, J. R. (1977). On the statistical theory of two-dimensional topographic turbulence. *J. Atmos. Sci.*, **34**: 1731–1750.
- Kraichnan, R. H. (1967). Inertial ranges in two-dimensional turbulence. *Phys. Fluids*, **10**: 1417–1423.
- Lavín, M. F. and Marinone, S. G. (2003). An overview of the physical oceanography of the Gulf of California. *O.U. Velasco Fuentes et al. (eds.), Nonlinear Processes in Fluid Dynamics, 173-204. ©2003 Kluwer Academic Publishers.*
- Lavín, M. F., R. Durazo, E. Palacios, M. L. Argote, and L. Carrillo (1997). Lagrangian observations of the circulation in the Northern Gulf of California. *J. Phys. Oceanogr.*, **27**: 2298–2305.

- Lavín, M. F., P. P. Niiler, A. Amador, R. Castro, and E. Beier (2007). Surface velocity patterns in the Gulf of California from satellite-tracked drifters. *Eos Trans. AGU*, **88**(23).
- Maassen, S. R., H. J. H. Clercx, and G. J. F. van Heijst (2003). Self-organization of decaying quasi-two-dimensional turbulence in stratified fluid in rectangular containers. *J. Fluid Mech.*, **495**: 19–33.
- Maassen, S. R. H. (2000). PhD thesis: Self-organization of confined two-dimensional flows. *Eindhoven University of Technology*.
- Makarov, V. and Jiménez-Illescas, A. (2003). Barotropic background currents in the Gulf of California. *Ciencias Marinas*, **29**(2): 141–153.
- Pedlosky, J. (1987). Geophysical fluid dynamics. *Springer-Verlag*.
- Salmon, R., G. Holloway, and M. C. Hendershott (1976). The equilibrium statistical mechanics of simple quasi-geostrophic models. *J. Fluid Mech.*, **75**: 691–703.
- Song, Y. and D. Haidvogel (1994). A semi-implicit ocean circulation model using a generalized topography-following coordinate system. *J. Comput. Phys.*, **115**: 228–244.
- Spitz, Y. H. and Nof, D. (1991). Separation of boundary currents due to bottom topography. *Deep-Sea Res.*, **38**: 1–20.
- Stern, M. E. and Austin, J. (1995). Entrainment of shelf water by a bifurcating continental boundary current. *J. Phys. Oceanogr.*, **25**: 3118–3131.
- Tabeling, P., S. Burkhart, O. Cardoso, and H. Willaime (1991). Experimental study of freely decaying two-dimensional turbulence. *Phys. Rev. Lett.*, **67**, 3772–3775.
- Taylor, G. I. (1923). Experiments on the motion of solid bodies in rotating fluids. *Proc. Roy. Soc. A*, **104**: 213–218.
- Tenreiro, M., L. Zavala Sansón, and G. J. F. van Heijst (2006). Interaction of dipolar vortices with a step-like topography. *Phys. Fluids*, **18**: 056603–1–12.
- Tenreiro, M., L. Zavala Sansón, G. J. F. van Heijst, and R. R. Trieling (2010). Experiments and simulations on self-organization of confined quasi-two-dimensional turbulent flows with discontinuous topography. *Phys. Fluids*, **22**: 025101–1–14.
- van de Konijnenberg, J. A. and van Heijst, G. J. F. (1996). Spin-up in a rectangular tank with a discontinuous topography. *Phys. Fluids*, **8**(11).
- van Heijst, G. J. F. and Clercx, H. J. H. (2009). Laboratory modeling of geophysical flows. *Annu. Rev. Fluid Mech.*, **41**: 143–164.

- van Heijst, G. J. F., P. A. Davies, and R. G. Davis (1990). Spin-up in a rectangular container. *Phys. Fluids A*, **2**: 150–159.
- van Heijst, G. J. F., H. J. H. Clercx, and D. Molenaar (2006). The effects of solid boundaries on confined two-dimensional turbulence. *J. Fluid Mech.*, **554**: 411–431.
- Zamudio, L., P. Hogan, and E. J. Metzger (2008). Summer generation of the Southern Gulf of California eddy train. *J. Geophys. Res.*, **113**: C06020.
- Zavala Sansón, L. and Sheinbaum, J. (2008). Elementary properties of the enstrophy and strain fields in confined two-dimensional flows. *Eur. J. of Mech. B/Fluids*, **27**: 54–61.
- Zavala Sansón, L. and van Heijst, G. J. F. (2002). Ekman effects in rotating flow over bottom topography. *J. Fluid Mech.*, **471**: 239–255.
- Zavala Sansón, L., G. J. F. van Heijst, and Doorschot, J. J. J. (1999). Reflection of barotropic vortices from a step-like topography. *Nuovo Cimento Soc. Ital. Fis., C*, **22**: 909–929.
- Zavala Sansón, L., R. Serravall, G. F. Carnevale, and G. J. F. van Heijst (2005). Experiments and simulations on coastal flows in presence of a topographic slope. *J. Phys. Oceanogr.*, **35**: 2204–2218.
- Zavala Sansón, L., A. González-Villanueva, and L. M. Flores (2010). Evolution and decay of a rotating flow over random topography. *J. Fluid Mech.*, **642**(159).